

A real-time time-dependent density functional theory method for
calculating linear and nonlinear dynamic optical response

Yoshinari Takimoto

A dissertation submitted in partial fulfillment of
the requirements for the degree of

Doctor of Philosophy

University of Washington

2008

Program Authorized to Offer Degree: Physics

University of Washington
Graduate School

This is to certify that I have examined this copy of a doctoral dissertation by

Yoshinari Takimoto

and have found that it is complete and satisfactory in all respects,
and that any and all revisions required by the final
examining committee have been made.

Chair of the Supervisory Committee:

John J. Rehr

Reading Committee:

John J. Rehr

George F. Bertsch

Bruce H. Robinson

Date:

In presenting this dissertation in partial fulfillment of the requirements for the doctoral degree at the University of Washington, I agree that the Library shall make its copies freely available for inspection. I further agree that extensive copying of the dissertation is allowable only for scholarly purposes, consistent with "fair use" as prescribed in the U.S. Copyright Law. Requests for copying or reproduction of this dissertation may be referred to ProQuest Information and Learning, 300 North Zeeb Road, Ann Arbor, MI 48106-1346, 1-800-521-0600, to whom the author has granted "the right to reproduce and sell (a) copies of the manuscript in microform and/or (b) printed copies of the manuscript made from microform."

Signature_____

Date_____

University of Washington

Abstract

A real-time time-dependent density functional theory method for calculating linear and nonlinear dynamic optical response

Yoshinari Takimoto

Chair of the Supervisory Committee:
Professor John J. Rehr
Department of Physics

We present an approach for the calculation of the frequency-dependent response of nano-scale organic molecules for non-linear optical (NLO) devices. These calculations are performed using an efficient implementation of real-time, time-dependent density functional theory (RT-TDDFT)¹ and an adaptation of the SIESTA electronic structure code. This method yields frequency-dependent nonlinear optical properties of large organic molecules, which have been difficult to obtain with frequency domain calculations. Here we discuss the efficiency of the method and compare the results against frequency-domain TDDFT methods and to experiments. Solvent effects on the NLO properties of photonic molecules are also briefly discussed.

¹Y. Takimoto, F. D. Vila, and J. J. Rehr, J. Chem. Phys. **127**, 154114 (2007)

TABLE OF CONTENTS

	Page
List of Figures	iii
List of Tables	vii
Chapter 1: Introduction	1
1.1 Overview	1
1.2 Goals	3
1.3 A Brief History and Dissertation Plan	4
1.4 Density Functional Theory (DFT)	6
1.5 Implementation of Order-N method in SIESTA	12
1.6 Time-dependent Density Functional Theory (TDDFT)	14
Chapter 2: Nonlinear Response Function in The Time and Frequency Domain . .	17
2.1 Description of Optical Response	17
2.2 Time-domain Response Function	18
2.3 Frequency-domain Response Function	20
Chapter 3: Method of Calculation (RT-TDDFT)	23
3.1 Real-time Method in TDDFT	23
3.2 Numerical Time Evolution	23
3.3 The Time-dependent External Field	26
3.4 The Static Finite Field Perturbation Theory	27
3.5 The Time-dependent Finite Field Perturbation	29
3.6 Quasi-monochromatic Field Approximation	31
3.7 Efficiency of RT-TDDFT Method	34
Chapter 4: Illustration with Small Molecules	36
4.1 Details of Simulation Setup	36
4.2 CO molecule	38
4.3 H ₂ O molecule	47

4.4	Resonant Frequencies (H_2O)	51
4.5	CHCl_3 molecule and Basis Set Tests	57
4.6	<i>para</i> -Nitroaniline (pNA)	63
4.7	Time-evolution Time Step Dependence on a System.	69
Chapter 5:	Application for Large Photonic Molecules	71
5.1	YLD156 Chromophore Linear and Non-linear Polarizability	71
Chapter 6:	Study of “Local” Solvent Effects in Optical Linear and Nonlinear Re- sponse	79
Chapter 7:	Future Prospects and Conclusion	90
	Bibliography	93
Appendix A:	Where to Find The Code and System Requirement	100
A.1	Obtaining the Code	100
A.2	System Requirement	100
Appendix B:	Real-time TDDFT Program Manual	102
B.1	Quick Start Guide	102
B.2	Static Calculation	103
B.3	Linear Response Calculation	107
B.4	Nonlinear Response Calculation	111
B.5	How to Prepare Pseudopotentials and Basis Sets	115
B.6	User’s Guide for prepsiesta	120
B.7	List of Available TDDFT Options in SIESTA	123
B.8	Parallel Computing	126
B.9	Developer’s Note	126
B.10	Limitations of the Real-time TDDFT in SIESTA	129

LIST OF FIGURES

Figure Number		Page
3.1	Addition of more expansion terms in the Crank-Nicholson operator. The evolution of dipole moment H_2O in time described as in Fig. 3.2 is evaluated with Eq. (3.6) labeled by CN_1 , and CN_3 with additional cubic term of Eq. (3.7). We have concluded that the additional term does not necessary help stability and the difference is too small to appear in the final optical spectra.	25
3.2	Time evolution of the dipole moment $\mathbf{p}(t)$ along the z -axis for H_2O , with a static \mathbf{E} field applied in the z -direction for $t < 0$ and turned off at $t = 0$. The z -axis is defined by the direction of permanent dipole of H_2O	28
4.1	Quasi-monochromatic external field of the Gaussian enveloped sine wave $F_\delta(t) = \exp[-(t - t_c)^2 \delta^2 / 2] \sin(\omega_0 t)$ with $\omega_0 = 1.179$ eV, $\delta = 0.1$ eV, and t_c located at 40% of the total simulation time T	37
4.2	Average photoabsorption of the CO molecule calculated within the adiabatic GGA/PBE in real time, including broadening of $\delta = 0.3$ eV. The absolute total optical oscillator strength is normalized by the sum-rule (the valence electron count). TDDFT/ALDA OCTOPUS results from Ref. [1] (their data is available only up to 12 eV). The experimental results from Ref. [2].	40
4.3	Second harmonic generation (SHG) $\beta_{ }(-2\omega; \omega, \omega)$ of CO. TDDFT/ALDA OCTOPUS results from Ref. [1]. LDA, BLYP, B3LYP, HF, and CCSD results from Ref. [3]. The experimental results from Ref. [4]	43
4.4	Evolution of orbital coefficients $c(t)$ of the Carbon atom for HOMO state in the CO molecule with the DZDP basis set (two radial functions per angular momentum). The z -axis defined along the bond direction.	45
4.5	Evolution of orbital coefficients $c(t)$ of the Oxygen atom for HOMO state in CO molecule with the DZDP basis set (two radial functions per angular momentum). The z -axis defined along the bond direction.	45
4.6	Evolution of orbital coefficients $c(t)$ of the Carbon atom for HOMO state in CO molecule with the 5Z4P basis set (five radial functions for s -state, four radial functions for p -state and polarization d -state). The z -axis defined along the bond direction.	46

4.7	Evolution of orbital coefficients $c(t)$ of the Oxygen atom for HOMO state in CO molecule with the 5Z4P basis set (five radial functions for s -state, four radial functions for p -state and polarization d -state). The z -axis defined along the bond direction.	46
4.8	Second harmonic generation $\beta_{ }(-2\omega; \omega, \omega)$ of H ₂ O. TDDFT/ALDA OCTOPUS results from Ref. [1]. LDA, BLYP, B3LYP, HF, and CCSD results from Ref. [3]. The experimental results from Ref. [4].	48
4.9	The imaginary part of average linear polarizability α of H ₂ O. The spectra with quasi monochromatic wave is calculated at each fixed frequency point. The spectra with the step function includes all frequency components with single real-time simulation. Both spectra include the same broadening of $\delta \approx 0.1$ eV.	49
4.10	Second harmonic generation $\beta_{ }(-2\omega; \omega, \omega)$ of H ₂ O including optical resonant frequencies.	49
4.11	The imaginary part of the second harmonic generation coefficient $\beta_{ }(-2\omega; \omega, \omega)$ of H ₂ O including optical resonant frequencies.	50
4.12	Optical rectification $\beta_{ }(0; \omega, -\omega)$ of H ₂ O including optical resonant frequencies. TDDFT/ALDA OCTOPUS results from Ref. [1].	50
4.13	The imaginary part of diagonal parts of linear polarizability α of H ₂ O. . . .	51
4.14	Second harmonic generation vector components along the dipole axis of $\beta_{iiz}(-2\omega; \omega, \omega)$ of H ₂ O.	52
4.15	Dipole moment (a.u.) v.s. time (fs) with the external frequency $\omega = 3.0$ eV of H ₂ O.	53
4.16	Dipole moment (a.u.) v.s. time (fs) with the external frequency $\omega = 4.5$ eV of H ₂ O. Location of the first resonant peak of the SHG.	54
4.17	Dipole moment (a.u.) v.s. time (fs) with the external frequency $\omega = 8.6$ eV of H ₂ O. Resonant location for $\beta_{zzz}(\omega)$	54
4.18	Optical rectification $\beta_{ }(0; \omega, -\omega)$ of H ₂ O around the lowest resonant frequency of the second harmonic generation.	56
4.19	Dipole moment (a.u.) v.s. time (fs) with the external frequency $\omega = 6.5$ eV, 6.8 eV, and 7.2 eV of H ₂ O for (E_y, p_z) responses showing from the top. . . .	56
4.20	The molecular structure of p -Nitroaniline (pNA). The bond lengths are shown in Å.	63
4.21	The imaginary part of dynamical polarizability $\text{Im } \alpha(\omega)$ of pNA obtained from the response to the step function external field.	64
4.22	The real part of dynamical polarizability $\text{Re } \alpha(\omega)$ of pNA, obtained from the response to the step function external field.	64
4.23	f -sum rule for pNA (see text). The exact limit is $N_e = 52$	65

4.24	Frequency-dependent of the first hyperpolarizability $\beta_{ }(-2\omega; \omega, \omega)$ for pNA, using the B-convention. References are given in Table 4.9, except for OCTOPUS [1].	68
4.25	The first hyperpolarizability $\beta_{ }(-2\omega; \omega, \omega)$ of pNA including the lowest resonant frequency, and compared against results of Ref. [1], using the B-convention. The results of two different simulation times are shown (26 and 46 fs) near the resonant frequency.	68
4.26	The real-time simulation of the dipole moment p_z of CO with quasimonochromatic frequency of $\omega = 1.17$ eV in E_z direction. The top curve is obtained with $\Delta t = 0.1$ Har $^{-1}$ and the bottom curve is obtained with $\Delta t = 0.12$ Har $^{-1}$	70
5.1	The molecular structure of YLD156 nonlinear chromophore.	72
5.2	UV/Vis. photoabsorption spectrum for YLD156. Experiment is measured in chloroform solution.	73
5.3	The first hyperpolarizability spectrum of $\beta_{zzz}(-2\omega; \omega, \omega)$ for YLD156.	77
5.4	The first hyperpolarizability spectrum of $\beta_{HRS}(-2\omega; \omega, \omega)$ for YLD156.	77
5.5	The first hyperpolarizability spectrum of $\beta_{zzz}(0; -\omega, \omega)$ and $\beta_{HRS}(0; -\omega, \omega)$ for YLD156.	78
6.1	pNA+M(A), the molecular structure of pNA with CH ₃ OH. Interaction of methanol through the acceptor side of pNA.	81
6.2	pNA+M(D), the molecular structure of pNA with CH ₃ OH. Interaction of methanol through the donor side of pNA.	81
6.3	pNA+M(A,D), the molecular structure of pNA with CH ₃ OH. Interaction of methanol through the both acceptor and donor side of pNA.	81
6.4	pNA+C(A), the molecular structure of pNA with CHCl ₃ . Interaction of chloroform through the acceptor side of pNA.	82
6.5	pNA+C(D), the molecular structure of pNA with CHCl ₃ . Interaction of chloroform through the donor side of pNA.	82
6.6	pNA+C(P), the molecular structure of pNA with CHCl ₃ . Interaction of chloroform through the the phenyl group of pNA.	82
6.7	pNA plus local solvent - methanol - absorption spectra.	86
6.8	pNA plus local solvent - chloroform - absorption spectra.	86
B.1	Quasi-monochromatic external field with ExternalFrequency = 1.0 eV and EnergyResolution = 0.1 eV. The shape of Gaussian function is determined automatically as described in Eq. (B.9) and Eq. (B.11) where the central peak is located at $T/2$ of the total simulation time T	114

B.2	Quasi-monochromatic external field with <code>ExternalFrequency</code> = 1.0 eV, where the envelope sine has a frequency <code>ExternalFrequency2</code> = 0.1 eV, and the total simulation time determined from <code>EnergyResolution</code> = 0.1 eV, as described in Eq. (B.11)	115
B.3	Schematic of the Hamiltonian matrix block form of the 1D processor grid in SIESTA main routine and the 2D processor grid in the matrix inverses routine.	129

LIST OF TABLES

Table Number		Page
4.1	Comparison of static polarizabilities and hyperpolarizabilities of CO. The results are in the atomic unit (a.u.). Our results include two different basis sets, DZDP and 5Z4P.	39
4.2	Absolute total optical oscillator strength for the $A^1\Sigma^+ \rightarrow A^1\Pi$ transition of CO. The value is determined from the integration of the dipole strength function $S(\omega)$ up to $\omega = 9.5$ eV. It yields the partial number of valence electron count for the transition.	41
4.3	Frequency-dependent hyperpolarizabilities of CO. Note that our result of smaller DZDP basis set turns out in undesired results that the value of $\beta_{ }(0; -\omega, \omega)$ is higher than that of $\beta_{ }(-2\omega; \omega, \omega)$	42
4.4	Frequency-dependent (hyper)polarizabilities of H ₂ O.	47
4.5	CHCl ₃ permanent dipole moment, linear polarizabilities, and the first hyperpolarizabilities results with SIESTA. Study of dependence with splitnorm value. The splitnorm of 0.15 is the SIESTA default setting. The DZDP basis set is the double- ζ plus two polarization functions. The 5Z4P basis set includes five- ζ with splitnorm of 0.6, 0.15, 0.015, and 0.0015. The “splitnorm” is a parameter for constructing the second- ζ . The value defines the amount of norm that the second- ζ split-off from the first- ζ has to carry, and the corresponding split radius is defined accordingly. All are calculated with energy shift of 0.5×10^{-7} for the first- ζ	58
4.6	CHCl ₃ permanent dipole moment, linear polarizabilities, and the first hyperpolarizabilities results with SIESTA. Study of convergence by varying energy shift $\delta\epsilon$ value. The DZP basis set and energy shift of 0.01 Har are the SIESTA default settings. The 5Z4P basis set is the same basis as used in Table 4.5.	59
4.7	CHCl ₃ permanent dipole moment, linear polarizabilities, and the first hyperpolarizabilities results with SIESTA, and compares against various methods with GAUSSIAN 03.	61
4.8	Frequency-dependent hyperpolarizability averages $\beta_{ }$ and β_{HRS} for the CHCl ₃ molecule. The first hyperpolarizability in physical unit is given by β 1 a.u. = $3.20636 \times 10^{-53} \text{C}^3\text{m}^3\text{J}^{-2}$ = 8.6392×10^{-33} esu.	62
4.9	Frequency-dependent hyperpolarizability $\beta_{ }(-2\omega, \omega, \omega)$ of pNA in the atomic unit, using the B-convention.	67

4.10	The maximum time step (Har^{-1}) for nonlinear calculation running for the total simulation time $T = 860 \text{ Har}^{-1}$ or $T \sim 20 \text{ fs}$. The elapsed time is also shown in 10^3 sec running on Intel(R) Xeon(R) CPU E5335 @ 2.00GHz. . . .	69
5.1	YLD156 permanent dipole moment, linear polarizabilities, and the first hyperpolarizabilities of static ($\omega = 0$) results with SIESTA (β 1 a.u. = $8.6392 \times 10^{-33} \text{ esu}$).	74
5.2	Frequency dependence of the nonlinear coefficients $\beta(0; -\omega, \omega)$ and $\beta(-2\omega; \omega, \omega)$ of YLD156 (β 1 a.u. = $8.6392 \times 10^{-33} \text{ esu}$).	75
5.3	Comparison of theoretical and HRS experimental values for YLD156. All β values are in 10^{-30} esu (β 1 a.u. = $8.6392 \times 10^{-33} \text{ esu}$).	76
6.1	The static properties of “local” solvent CH_3OH or CHCl_3 near pNA. The values presented in parenthesis are the calculations of the solvent molecule alone but keeping the orientation the same as corresponding geometry with pNA.	84
6.2	The first absorption peak ω_{max} and λ_{max} of pNA with “local” solvent CH_3OH or CHCl_3	85
6.3	The first hyperpolarizability β at $\omega = 1.165 \text{ eV}$ with “local” solvent CH_3OH near pNA. The values presented in parenthesis are the calculations of the solvent molecule alone but keeping the orientation the same as corresponding geometry with pNA.	88
6.4	The first hyperpolarizability β at $\omega = 1.165 \text{ eV}$ with “local” solvent CHCl_3 near pNA. The values presented in parenthesis are the calculations of the solvent molecule alone but keeping the orientation the same as corresponding geometry with pNA.	89

ACKNOWLEDGMENTS

I wish to express my most sincere thanks and appreciation to my advisor, John Rehr, for all of his help and guidance.

I would especially like to express my thanks to Dr. Fernando Vila for his support and for sharing his indispensable knowledge of quantum chemistry.

Both John and Fernando also provided support and assistance for various computational methods, techniques, and insights that have truly enlightened this work and helped to move this project forward throughout.

In addition, I would like to thank Dr. Bruce Eichinger, Professor Bruce Robinson, and Professor Larry Dalton for their encouragement of this work, and for their continuous, insightful suggestions and support.

I am grateful to Professor George Bertsch for his expertise, comments, and suggestions, and to Dr. Argyrios Tsolakidis and Professor Richard Martin for allowing us to use their code, as well as for their exchange of knowledge and assistance.

I also acknowledge that this project benefited from fruitful discussions and philosophical debates with my colleagues, Micah Prange and Joshua Kas.

I must acknowledge Nancy Kool for her editing assistance, in particular, her expertise in editing technical articles as well as understanding the characteristic differences between English and Japanese authors.

Finally, I would like to acknowledge the support of my family for their patience understanding and for their continuing cheerful support.

Chapter 1

INTRODUCTION

1.1 Overview

The theme of this dissertation is the theory of linear and nonlinear optical response in real time. The approach is complementary to the conventional treatment in terms of harmonically varying sources of a monochromatic wave of light and provides a novel approach to understanding the physics of optical interaction with electrons. The history of nonlinear optics starts from the study of nonlinear crystals. In recent years, there has been considerable interest in organic materials with high nonlinear optical (NLO) coefficients as potential alternatives to the inorganic materials in current use for integrated optical devices. The main reason is that the performance of the organic materials has been found to be more than an order of magnitude higher than that of the best inorganic materials. As a result, there is a demand for theoretical characterization of nonlinear organic materials and interests in searching and designing new organic materials with the desired linear and nonlinear optical properties.

The objective of this dissertation is to calculate the linear and nonlinear optical properties of organic materials from a first principle. The brief history of the first principle (*ab initio*) begins as follows. In 1926 E. Schrödinger published the celebrated paper on wave mechanics and presented the Schrödinger equation for the wave function Ψ of electrons [5]. In 1998 Nobel Prize in chemistry was awarded for the development of the modern computational method in quantum chemistry.¹ Half of the prize went to John A. Pople for his development of computational methods in quantum chemistry, and the other half was awarded to Walter Kohn for his development of the density-functional theory (DFT). In

¹http://nobelprize.org/nobel_prizes/chemistry/laureates/1998/

their Nobel lectures, both quoted a famous remark made by Dirac in 1929 for the successful of the ultimate theory of many electrons by wave-mechanics:

“The fundamental laws necessary for the mathematical treatment of a large part of physics and the whole of chemistry are thus completely known, ...”

Unfortunately, his delightful remark continues.

“And, the difficulty lies only in the fact that application of these laws leads to equations that are too complex to be solved.”

As a result, Schrödinger created not only wave-mechanics of electrons, but also the field of *ab initio* electronic structure as attempt to solve the complex equation from the first principle. However, the true birth of the field had to wait for the first working programmable digital computer. The history of the programmable digital computer begins in Germany in 1938 when Konrad Zuse built the first electro-mechanical binary programmable computer, called Z1, with all the essential components of modern processors. The Z1 had a 64-word memory (22 bits/word) running a clock speed of 1 Hz with input/output through punch tape. Today’s highest “official” ranking of supercomputers according to the LINPACK benchmark² is the IBM supercomputer “RoadRunner” housed in Los Alamos National Laboratory, which has 122,400 processors and a main memory of 98 TB. It recorded the peak floating point operations at 1.026 PFlops (over 10^{15} operations in a second).

Although Dirac could probably not imagine today’s exponential growth in digital computing power, his comment that the full treatment of the Schrödinger-Dirac equation is far too complicated to solve exactly, except for very small molecules is still correct. During the 1930s, one of the great successes of the early theory to find the approximate solution of many-body Schrödinger equation is the Hartree-Fock theory, where the wave function Ψ of n electrons is constructed from independent dynamics of n electrons using the Slater determinant, in which the $2n$ electrons are assigned to a set of n orbitals $\psi_i (i = 1, \dots, n)$, where each orbital has two degrees of freedom for spins σ . Then, the many-electron wave function for the theory is formed as:

$$\Psi = \frac{1}{\sqrt{n!}} \det |\psi_1(\mathbf{x}_1)\psi_2(\mathbf{x}_2) \dots \psi_n(\mathbf{x}_n)|, \quad (1.1)$$

²TOP500 Supercomputing Sites <http://www.top500.org/>

where $\mathbf{x}_i \equiv (\mathbf{r}, \sigma)$ includes both the spatial coordinate and the spin coordinate of the i -th electron. The method of the Hartree-Fock theory is to find the wave function Ψ by varying the orbital ψ_i to minimize the total energy of the system by calculating the full hamiltonian H for the independent electrons,

$$E = \langle \Psi | H | \Psi \rangle. \quad (1.2)$$

1.2 Goals

In this thesis, I set the goal as to carry out the linear and nonlinear dynamics of the optical response of a “large” molecule. More precisely, the main goals of this dissertation are:

- Develop an implementation of optical response based on the general theory of linear and nonlinear response for a system of many electrons due to an external electric field (optical response).
- Parameter free *ab initio* method of computation to calculate observable linear and nonlinear optical quantities at an accuracy comparable to that of experiments within reasonable fractions of “human” time scale (*not* astronomical time scale).
- The method must enable the simulation of the *real* laboratory and characterize optical devices to help designing better organic materials and new devices. In particular, it is desirable to compute optical properties of “large” molecules, including the “state-of-art” molecules used in engineering of optical integrated devices.

In order to achieve these goals, I selected “tools” according to following criteria:

- To avoid the “exponential well” of solving the problem of correlated many-electron systems, the density functional theory (DFT) described below is favored over the wave function method.
- The scale of simulation should not grow exponentially as the number of electrons increases, but grows with the small polynomial power of the number of atoms involved.

A fast and scalable numerical method and its implementation are necessary to handle the very large system of N atoms.

- The method must have an extension to optical excitation, and not be limited to ground-state properties. This requires the time-dependent density functional theory (TDDFT) rather than ground-state DFT.

Indeed, the linear properties of optical properties is already mature, and many different methods are widely available. This dissertation is focused mainly on the implementation of the nonlinear optical properties.

1.3 A Brief History and Dissertation Plan

The study of nonlinear optics is conceptually simple as it can be described by the classical theory of electro-magnetism. One of the early observations of the nonlinear effect in the luminescence of dye molecules is reported by Lewis *et al.* in 1941 [6]. However, the field of nonlinear optics gained wide popularity only after the invention of the first working laser by Maiman in 1960 [7, 8]. Subsequently, the birth of nonlinear optics is often referred to as the discovery of the second harmonic generation (SHG) with a laser source by Franken *et al.* [9]. The qualitative explanation of the second harmonic generation or nonlinear properties is easily understood via classical nonlinear response function as well as in terms of hyperpolarizabilities $\beta(-2\omega; \omega, \omega)$. Another important second-order nonlinear effect is the optical rectification (OR) first reported by Bass *et al.* [10], which is the generation of a DC polarization in a nonlinear medium through an intense laser beam. The optical rectification is explained in terms of hyperpolarizabilities $\beta(0; -\omega, \omega)$. The quantitative study of *ab initio*, parameter free calculation becomes possible much later than the discovery of the nonlinear phenomena. Chong in 1992 [11] and Guan *et al.* in 1993 [12] were among the first to study hyperpolarizability in the static limit by DFT at the LDA level using a finite-difference technique. In 1998, the first calculations of dynamic, frequency-dependent hyperpolarizabilities were performed by Gisbergen *et al.* [13] using adiabatic LDA (ALDA). Frequency-dependent hyperpolarizabilities beyond ALDA were presented by Salek *et al.* [14] in 2002 using the calculation of quadratic response functions at the LDA, GGA, and hybrid

functional levels of DFT. In fact, most of the developments are made in the frequency space, which requires accurate description of the “excited states” of the system of interests. Moreover, the frequency domain calculation of hyperpolarizabilities relies on a perturbation expansion due to external perturbation, and such expansion fails at resonant frequencies. As a result, such calculations are prohibitively difficult as the system size grows, and the method has not been demonstrated to perform for a large system. Only in 2005 did the best, most detailed study of the hyperpolarizabilities at the high-level *ab initio* method such as the coupled-cluster single and double excitation model (CCSD) has been tested for a medium-sized molecules like *para*-Nitroaniline (pNA) [3], although the authors called this 16-atom molecule “large.”

There are many cases, both experimental and theoretical, in which it is more convenient to work in the time (rather than the frequency) domain. In 1996 Yabana and Bertsch first demonstrated the dipole response of atomic clusters in real time within TDDFT/ALDA [15]. Since then, the real-time method has gained wide popularity due to its accuracy, where the first absorption peak can often be predicted within a few tenths of eV, as well as its scalability to the large system, where the method can easily applied to several hundreds of atoms. Unlike the most of frequency domain methods, the real-time methods can be efficiently implemented in $\mathcal{O}(N)$ with N being the number of atoms involved. However, the real-time study of nonlinear hyperpolarizabilities has not been demonstrated until recently. It has been generally considered that the extension of the real-time method to the nonlinear calculation is non-trivial in contrast to the perturbation method in the frequency space perturbation. Shortly before our publication of the real-time method in 2007 [16], Wang *et al.* also demonstrated and compared both real-time and frequency domain methods for binary molecules, CO, HF, HCl, and LiF [17], and they have concluded the former is much more time consuming than the frequency domain calculation. However, our generic method of calculating dynamic properties of nonlinear hyperpolarizabilities in real-time methodology concluded the exact opposite for the large system. Our method is build upon previous work by Tsolakidis *et al.* [18] which mainly developed for calculating linear properties. The implementation over efficient $\mathcal{O}(N)$ DFT method enables the calculation of frequency-dependent hyperpolarizability for the large system efficiently, including several hundreds

atoms, within experimental accuracy.

In the following sections, a brief background will be presented for the theoretical “tools” that are required for completing this dissertation in the rest of this introductory chapter. We will then proceed to the main body and describe the method and applications in the subsequent chapters. In chapter 2, the construction and generic properties of the linear and nonlinear response functions are described. In chapter 3, the detailed description of the real-time TDDFT (RT-TDDFT) calculation will be presented. In chapter 4, the illustration with small molecules is presented. We also discuss the dependence and variation of results by the choice of the basis set of atomic orbitals and their time-domain behavior in this chapter. The application to one of the “state-of-art” large photonic molecule will be presented in chapter 5. Then, some preliminary studies on the solvent-effect are described in chapter 6. Final conclusions and future prospects are discussed in the last chapter.

1.3.1 Units

We use a system of atomic units (a.u.) throughout this dissertation unless otherwise denoted. In this unit of convention, all equations are presented following physical constants are set to one,

$$e = m_e = \hbar = 1 \quad (1.3)$$

where e is the elementary charge on the proton, m_e is the electron mass, \hbar Planck’s constant divided by 2π . Other atomic units having magnitudes of unity can be obtained by the dimensional analysis. For example, the quantity $\hbar^2/m_e e^2$ has unit of distance and called Bohr radius a_0 , and the quantity e^2/a_0 has units of energy and called Hartree energy (Har) E_h . The equations expressed in SI units Coulomb’s constant $1/4\pi\epsilon_0$ also have magnitude 1. Note that the speed of light c in the atomic unit is $1/\alpha = 137$.

1.4 Density Functional Theory (DFT)

The density functionary theory (DFT) provides a rather different approach to solving the electron dynamics of nature in contrast to the wave function method. The foundation of DFT is based on the theorem published by Kohn and Hohenberg [19] in 1964, and its

clever implementation shortly after by Kohn and Sham [20] in 1965, almost 40 years after Schrödinger's work. The philosophy of the density functional theory is to use the physical *observable*, the electron charge density $\rho(\mathbf{r})$, to compute the total energy as well as the other physical properties of a system in the ground-state. It is said to be the *energy functional*,

$$E[\rho(\mathbf{r})]. \quad (1.4)$$

If such a construction is possible, the immediate advantages over the previously described wave function method is that we have reduced the number of degrees of freedom down to three instead of $3n$ spatial coordinates for a wave function of an n electron system.

1.4.1 The Hohenberg-Kohn Existence Theorem

The rigorous foundation of the first theorem of DFT is an “existence theorem.” It states that there exists a universal functional of the density $\rho(\mathbf{r})$, $F[\rho(\mathbf{r})]$, independent of an external potential $v(\mathbf{r})$ of interacting electrons, such that the expression $E = \int v(\mathbf{r})\rho(\mathbf{r})d\mathbf{r} + F[\rho(\mathbf{r})]$ has its minimum value when the correct ground-state energy associated uniquely with $v(\mathbf{r})$ (except the constant energy) [19]. In the case of a degenerate ground-state, the theorem refers to *any* ground-state density ρ . The proof is very simple and proceeds via *reductio ad absurdum* that shows that an assumption to the contrary generates a contradictory result. Here, we proceed the proof for a non-degenerate ground-state density ρ_0 . Thus, let us assume that two *different* external potentials can consistently associate with the same non-degenerate ground-state density ρ_0 .

Let the two potentials $v_1(\mathbf{r})$ and $v_2(\mathbf{r})$ correspond to Ψ_1 and Ψ_2 of n electrons with the ground-state density of ρ_0 , and the energy E_1 and E_2 of the total Hamiltonian H_1 and H_2 , respectively. Without loss of generality, we assume that Ψ_1 to be non-degenerate ground-state. Then,

$$E_1 = \langle \Psi_1 | H_1 | \Psi_1 \rangle = \int v_1(\mathbf{r})\rho_0(\mathbf{r}) d\mathbf{r} + \langle \Psi_1 | T + U | \Psi_1 \rangle, \quad (1.5)$$

where T and U are the kinetic and interaction operators. And similarly, we have,

$$E_2 = \int v_2(\mathbf{r})\rho_0(\mathbf{r}) d\mathbf{r} + \langle \Psi_2 | T + U | \Psi_2 \rangle, \quad (1.6)$$

where $v_2(\mathbf{r})$ *not* equal to $v_1(\mathbf{r}) + \text{constant}$, and the ground-state Ψ_2 must differ more than phase from Ψ_1 under the assumption. The Rayleigh-Ritz minimal principle for Ψ_1 gives the inequality for non-degenerate Ψ_1 ,

$$E_1 < \langle \Psi_2 | H_1 | \Psi_2 \rangle = \int v_1(\mathbf{r}) \rho_0(\mathbf{r}) d\mathbf{r} + \langle \Psi_2 | T + U | \Psi_2 \rangle, \quad (1.7)$$

Similarly,

$$E_2 \leq \langle \Psi_1 | H_2 | \Psi_1 \rangle = E_1 + \int (v_2(\mathbf{r}) - v_1(\mathbf{r})) \rho_0(\mathbf{r}) d\mathbf{r}, \quad (1.8)$$

where non-strict inequality is used, since the non-degeneracy of Ψ_2 was not assumed. Adding the Eq. (1.7) and Eq. (1.8) leads to the contradiction,

$$E_1 + E_2 < E_1 + E_2. \quad (1.9)$$

The contradiction leads us to conclude that the assumption of two *different* external potentials gives the same ground-state ρ_0 must be wrong. The external potential $v(\mathbf{r})$ provides the charges and positions of the nuclei, and the integration of $\rho(\mathbf{r})$ already gives the number of electrons n . Hence, the density $\rho(\mathbf{r})$ determines the Hamiltonian operator H and implicitly determines *all* properties from H through the solution of the time-independent or time-dependent Schrödinger equation, including additional perturbations such as the electromagnetic fields.

1.4.2 The Hohenberg-Kohn Variational Principle

The wave function method, including the HF method described earlier, has a searching algorithm for the ground-state wave function from trial wave functions $\tilde{\Psi}$. That we search for the minimum of the total energy equation by the trial wavefunctions $\tilde{\Psi}$,

$$E = \min_{\tilde{\Psi}} \langle \tilde{\Psi} | H | \tilde{\Psi} \rangle. \quad (1.10)$$

The global minimum of the total energy equation gives the true ground-state wave function Ψ . In the case of the density ρ , the same principle applies by virtue of the Hohenberg-Kohn existence theorem. That is, we seek for minimum of the total energy of the system as a functional of density $\rho(\mathbf{r})$,

$$E[\rho(\mathbf{r})]. \quad (1.11)$$

The procedure has two steps, and is called the constrained search method. The total number of electrons n is fixed for a given system with density $\rho(\mathbf{r})$, and we consider a class of trial wave functions that yield the same density, say $\tilde{\Psi}_\rho$. We then define the constrained energy minima by fixing the density ρ ,

$$E[\rho(\mathbf{r})] \equiv \min_{\tilde{\Psi}_\rho} \langle \tilde{\Psi}_\rho | H | \tilde{\Psi}_\rho \rangle = \int v(\mathbf{r})\rho(\mathbf{r}) d\mathbf{r} + F[\rho(\mathbf{r})], \quad (1.12)$$

where

$$F[\rho(\mathbf{r})] \equiv \min_{\tilde{\Psi}_\rho} \langle \tilde{\Psi}_\rho | T + U | \tilde{\Psi}_\rho \rangle, \quad (1.13)$$

where $F[\rho]$ is a universal functional of the density ρ without explicit dependence of $v(\mathbf{r})$. The second step is to minimize the total energy by varying the density ρ ,

$$E = \min_{\rho(\mathbf{r})} E[\rho(\mathbf{r})] = \min_{\rho(\mathbf{r})} \left\{ \int v(\mathbf{r})\rho(\mathbf{r}) d\mathbf{r} + F[\rho(\mathbf{r})] \right\}. \quad (1.14)$$

The last minimization yields the ground-state density $\rho_0(\mathbf{r})$.

1.4.3 The Kohn-Sham Self-consistent Field Equations

The energy functional $E[\rho(\mathbf{r})]$ is, in principle, only dependent on 3-spatial variables of the density $\rho(\mathbf{r})$ and *much* simpler than the minimization of $\langle \tilde{\Psi} | H | \tilde{\Psi} \rangle$ including $3n$ -dimensional variables of trial function $\tilde{\Psi}$. However, the real difficulty is the evaluation of functional Eq. (1.11); neither its explicit functional form is known nor is there a systematic procedure for finding such functional dependence on ρ . Indeed, the definition of Eq. (1.13) for $F[\rho(\mathbf{r})]$ requires the minimization of $3n$ -dimensional trial wave functions.

At this point, DFT is just a formalism without providing any implementation, i.e., too abstract to find use in practice. The key realization is made by Kohn-Sham in 1965 [20] with the emergence or “invention” of the Kohn-Sham(KS) *fictitious non-interacting* system. More precisely, constructing a *fictitious* system of *non-interacting* electrons that have the same ground-state density as the *true* system of *interacting* electrons. By Eq. (1.12), this *fictitious* system necessarily determines the external potential including the position and atomic numbers of the nuclei identical to the *true* system. The remaining problem of

evaluating complex functional dependence on ρ of Eq. (1.13) can be broken down into,

$$E[\rho(\mathbf{r})] = \int v(\mathbf{r})\rho(\mathbf{r}) d\mathbf{r} + F[\rho(\mathbf{r})] \quad (1.15)$$

$$= \int v(\mathbf{r})\rho(\mathbf{r}) d\mathbf{r} + \tilde{T}[\rho(\mathbf{r})] + \tilde{U}[\rho(\mathbf{r})] + E_{\text{xc}}[\rho(\mathbf{r})], \quad (1.16)$$

where \tilde{T} , \tilde{U} , and E_{xc} are the kinetic energy of the non-interacting electrons, the Coulomb repulsion of a classical charge distribution, and the exchange and correlation energy of interacting electrons called the "exchange-correlation" energy, respectively. In the case of a non-interacting system of n electrons, we can construct the wave function from the single-electron wave function $\phi_i(\mathbf{r})$ ($i = 1 \dots n$), called the Kohn-Sham(KS) orbitals, and the density is given by,

$$\rho(\mathbf{r}) = \sum_{i=1}^n \phi_i^*(\mathbf{r})\phi_i(\mathbf{r}). \quad (1.17)$$

The Eq. (1.16) in terms of the KS orbitals can be written as,

$$E[\rho(\mathbf{r})] = \int v(\mathbf{r})\rho(\mathbf{r}) d\mathbf{r} + \sum_i^n \langle \phi_i | -\frac{1}{2}\nabla_i^2 | \phi_i \rangle \quad (1.18)$$

$$+ \sum_i^n \langle \phi_i | \frac{1}{2} \int \frac{\rho(\mathbf{r}')}{|\mathbf{r}_i - \mathbf{r}'|} d\mathbf{r}' | \phi_i \rangle + E_{\text{xc}}[\rho(\mathbf{r})]. \quad (1.19)$$

The corresponding eigenvalue equation to solve the KS orbitals is known as the Kohn-Sham(KS) equation

$$h_i^{\text{KS}}\phi_i = \epsilon_i\phi_i, \quad (1.20)$$

where the KS single-electron Hamiltonian is defined as

$$h_i^{\text{KS}} = v(\mathbf{r}) - \frac{1}{2}\nabla^2 + \int \frac{\rho(\mathbf{r}')}{|\mathbf{r} - \mathbf{r}'|} d\mathbf{r}' + V_{\text{xc}}, \quad (1.21)$$

and

$$V_{\text{xc}} \equiv \frac{\delta E_{\text{xc}}[\rho(\mathbf{r})]}{\delta \rho(\mathbf{r})}. \quad (1.22)$$

V_{xc} is the functional derivative of the exchange-correlation energy.

Note that up to this point, the formalism is "exact" in that we can obtain the exact ground-state density when we find the minimum of the energy functional of the self-consistent Eq. (1.19).

1.4.4 The Exchange-correlation Functionals

The only remaining part, and the most difficult task, is the explicit evaluation of the exchange-correlation functional $E_{\text{xc}}[\rho(\mathbf{r})]$. Unfortunately, there is no systematic method of evaluating E_{xc} for the real system of many electrons. Unlike many-body perturbation theory of the wave function method, the approximation of E_{xc} must start from a “guess.”

The first approximation for E_{xc} is to assume a local dependence on the density ρ . That can be written as

$$E_{\text{xc}} = \int \varepsilon_{\text{xc}}(\mathbf{r}; [\rho(\mathbf{r})]) \rho(\mathbf{r}) d\mathbf{r}, \quad (1.23)$$

where ε_{xc} is the exchange-correlation energy density at point \mathbf{r} with functional dependence on the density $\rho(\mathbf{r})$. The simplest of this class is called the local density approximation (LDA) where the value of ε_{xc} at the position \mathbf{r} is exclusively determined from the value of the density ρ at the position,

$$E_{\text{xc}}^{\text{LDA}} \equiv \int \varepsilon_{\text{xc}}[\rho(\mathbf{r})] \rho(\mathbf{r}) d\mathbf{r}. \quad (1.24)$$

Indeed, the only physical system to accommodate LDA functional is that of homogeneous electron gas. The exchange part of the functional for such a system can be determined explicitly by the Slater determinant of the KS wave functions, that is,

$$\varepsilon_{\text{x}}[\rho(\mathbf{r})] = -\frac{9}{8} \left(\frac{3}{\pi} \right)^{1/3} \rho^{1/3}(\mathbf{r}). \quad (1.25)$$

The correlation part has no analytic form even for homogeneous electron gas, but has been determined numerically to very high precision using quantum Monte Carlo techniques by Ceperley and Alder [21].

The next construction is to include both density and the gradient of the density in the evaluation, called the generalized gradient approximation (GGA),

$$E_{\text{xc}}^{\text{GGA}} = \int \varepsilon_{\text{xc}}[\rho(\mathbf{r}), \nabla \rho(\mathbf{r})] \rho(\mathbf{r}) d\mathbf{r}. \quad (1.26)$$

The hybrid approach to the exchange-correlation functional was first introduced by Becke in 1993 [22]. The functional is constructed by a linear combination or the parameterized

mixture of combining Hartree-Fock (HF) (exact) exchange and DFT exchange-correlation functionals. Hybridization with the HF exchange has found to provide a simple scheme for improving many molecular properties including bond lengths and vibration frequencies which tend to fail with simple the LDA or GGA functionals [23].

1.5 Implementation of Order- N method in SIESTA

SIESTA is a general-purpose *ab initio* fully self-consistent DFT code, using linear combination of atomic orbitals (LCAO) basis set [24, 25, 26, 27]. Some of critical features of SIESTA code during the implementation of linear and nonlinear optical response calculation are described briefly in this section. SIESTA is capable of solving the electronic structure with essentially $\mathcal{O}(N)$ scaling where N is the number of atoms. The main players of optical response are valence electrons; unnecessary core electrons are conveniently replaced by norm-conserving pseudopotentials of the Troullier-Martins parametrization [28]. These semilocal pseudopotentials are subsequently transformed into the fully nonlocal Kleinman-Bylander (KB) [29] form. The basis set is a generic linear combination of numerical atomic orbitals (NAOs), and the atomic basis orbitals are products of a numerical radial function and a spherical harmonic,

$$\phi_{I,lmn}(\mathbf{r}) = \phi_{Iln}(r_I)\hat{Y}_{lm}(\hat{\mathbf{r}}_I), \quad (1.27)$$

where $\mathbf{r}_I = \mathbf{r} - \mathbf{R}_I$ for atom I located at \mathbf{R}_I . This numerical radial functions are made strictly zero beyond a certain cut-off radius r_c [30]. This confinement of NAOs is crucial for making the Hamiltonian and overlap matrices in sparse form and very important for efficiency of SIESTA code. This sparseness construction is critical for designing $\mathcal{O}(N)$ method to enable both computational and storage cost to scale linearly with the number of atoms. The minimal basis set has a single radial function $\phi_{Iln}(r)$ per angular momentum per atom. In general, multiple radial functions are introduced with the same angular dependence for flexibility, which is conventionally named the “multiple- ζ ” basis. In this scheme, the minimal basis is called single- ζ (SZ), and higher basis orbitals are called double- ζ (DZ), triple- ζ (TZ), and so on.

The construction of the first basis orbital (SZ) in SIESTA uses the method of Sankey and

Niklewski [30, 31]. Here the basis orbitals are the eigenfunction of the atomic pseudopotentials within a spherical box. More precisely, the radial eigenfunctions $\phi_l(r)$ (where l and n are implicit) of the atomic pseudopotentials $V_l(r)$, and energy $\epsilon_l + \delta\epsilon_l$ are chosen such that the first node is located at the cut-off radius r_c ,

$$\left[-\frac{1}{2r} \frac{d^2}{dr^2} + \frac{l(l+1)}{2r^2} + V_l(r) \right] \phi_l(r) = (\epsilon_l + \delta\epsilon_l) \phi_l(r), \quad (1.28)$$

with setting $\phi_l(r_c) = 0$. To make a well-balanced basis, a common “energy shift” $\delta\epsilon_l$ is usually enforced on all the atoms rather than using a fixed cut-off radius r_c . The scheme of adding higher- ζ is based on the widely used method in quantum chemistry called the *split valence* [32, 33, 34]. The usual construction of an atomic Gaussian type orbitals (GTOs) of the first- ζ is defined by using the most contracted contracted Gaussians, and using the most extended ones for the double- ζ . In SIESTA, the multiple- ζ consists of adding each orbital with a new basis function that matches the tail of the first- ζ orbital at a given “split” radius r_s outwards. The inner part goes smoothly towards the origin as a simple polynomial:

$$\phi_l^{2\zeta}(r) = \begin{cases} r^l(a_l - b_l r^2) & \text{if } r < r_s \\ \phi_l^{1\zeta}(r) & \text{if } r \geq r_s \end{cases}, \quad (1.29)$$

where a_l and b_l are chosen by imposing the continuity of the function and its derivative at r_s . The generalization of higher multiple- ζ is simply accomplished by adding more functions by the same procedure described above.

The atomic orbitals of valence electrons in molecule are necessary to consider the deformation introduced by bond formation as well as by polarization of the electrons due to the presence of an external field for describing optical excitation. In case of pseudo valence orbital $\phi_{lm}(\mathbf{r}) = \phi_l(r)Y_{lm}(\hat{\mathbf{r}})$, the simple addition of valence orbitals with angular momentum $l+1$ is problematic in that they are often too extended or unbound. Instead, the polarization orbital is determined by the first-order perturbation theory, by adding a small electric field \mathbf{E} in the z -direction. Then, we have the equation

$$(h - \epsilon)\delta\phi = -(h_1 - \epsilon_1)\phi, \quad (1.30)$$

where $h_1 = E_z$ and $\epsilon_1 = \langle \phi | h_1 | \phi \rangle = 0$ since h_1 is odd. The dipole selection rule implies that

the perturbed orbital $\delta\phi$ will only have components with $l' = l \pm 1$, $m' = m$. We have

$$h_1\phi_{lm}(\mathbf{r}) = E r \cos(\theta)\phi_l(r)Y_{lm}(\hat{\mathbf{r}}) = E r \phi_l(r) (c_{l-1}Y_{l-1,m}(\hat{\mathbf{r}}) + c_{l+1}Y_{l+1,m}(\hat{\mathbf{r}})) \quad (1.31)$$

and

$$\delta\phi_{lm}(\mathbf{r}) = \varphi_{l-1}(r)Y_{l-1,m}(\hat{\mathbf{r}}) + \varphi_{l+1}(r)Y_{l+1,m}(\hat{\mathbf{r}}). \quad (1.32)$$

Generally, the orbitals with angular momentum $l - 1$ are already present in the basis set. We find the equation for φ_{l+1} by substituting Eq. (1.31) and Eq. (1.32) into Eq. (1.30), then multiplying $Y_{l+1,m}^*(\hat{\mathbf{r}})$ and integrating over the angular variables that we have,

$$\left[-\frac{1}{2r} \frac{d^2}{dr^2} r + \frac{(l+1)(l+2)}{2r^2} + V_l(r) - \epsilon_l \right] \varphi_{l+1}(r) = -r \phi_l(r), \quad (1.33)$$

where E and c_{l+1} are eliminated since they only affect the normalization. Finally, the polarization orbitals are set by $\phi_{l+1,m}(\mathbf{r}) = N\varphi_{l+1}(r)Y_{l+1,m}(\hat{\mathbf{r}})$, with a normalization constant N .

The basis set consist of double- ζ and polarization (DZP) usually yields high-quality results for most systems; hence, the DZP basis set is named the “standard” basis in SIESTA. For the calculation of non-linear properties including its static properties, we found a case where the DZP basis fails, especially for a small molecule. We discuss the basis dependence for the optical nonlinearity further in chapter 4.

1.6 Time-dependent Density Functional Theory (TDDFT)

The DFT has been demonstrated its applicability with some successful exchange-correlation functional for a fictitious noninteracting electron system that provides an efficient method for treating ground-state properties of many-electron systems such as solids and molecules. Unfortunately, the excited states calculated within the Kohn-Sham method are not so successful for a time-dependent perturbation such as optical response and the excitation spectra. This time-dependent analogue of the ground-state DFT is called the time-dependent density functional theory (TDDFT) and was first formally proven for (within certain general conditions) by Runge and Gross [35]. The extension to the ground-state DFT formalism shows that there is a one-to-one correspondence between time-dependent density $\rho(\mathbf{r}, t)$ and

time-dependent potentials $v_{\text{ext}}(\mathbf{r}, t)$ for a given initial condition. Indeed, the initial applications of TDHF to atomic systems predated the formal development of TDDFT by Zangwill and Soven [36].

The proof of the Runge-Gross theorem is more involved than that of the Hohenberg-Kohn theorem, and we omit it. What the former have demonstrated is that if two external potentials $v(\mathbf{r}, t)$ and $v'(\mathbf{r}, t)$ differ by more than a purely time-dependent function $c(t)$, they cannot produce the same time-dependent density $\rho(\mathbf{r}, t)$. By the uniqueness and one-to-one correspondence of potential and density, we can take the KS non-interacting electrons density to be the same as the interacting density of the real system. Then, the time-dependent KS electrons obey the time-dependent Schrödinger equation

$$i\frac{\partial}{\partial t}\phi_i(\mathbf{r}, t) = \hat{h}_i^{\text{KS}}(t)\phi_i(\mathbf{r}, t). \quad (1.34)$$

The density of the interacting system is given by

$$\rho(\mathbf{r}, t) = \sum_i^N |\phi_i(\mathbf{r}, t)|^2, \quad (1.35)$$

and the time-dependent KS Hamiltonian is

$$\hat{h}_i^{\text{KS}}(t) = v_{\text{ext}}(\mathbf{r}, t) - \frac{1}{2}\nabla^2 + \int \frac{\rho(\mathbf{r}', t)}{|\mathbf{r} - \mathbf{r}'|} d\mathbf{r}' + V_{\text{xc}}(\mathbf{r}, t). \quad (1.36)$$

Again, the last term is the time-dependent exchange-correlation potential, which includes all the non-trivial many-body effects. It was formally solved by van Leeuwen [37] using the Keldish formalism of a new action function $\tilde{\mathcal{A}}$ based on the quantum mechanical action \mathcal{A} ,

$$\mathcal{A}[\Phi] = \int_{t_0}^{t_1} \langle \Phi(t) | i\frac{\partial}{\partial t} - \hat{H}(t) | \Phi(t) \rangle dt, \quad (1.37)$$

where $\Phi(t)$ is a n-body function defined in some convenient space. The time-dependent exchange-correlation (xc) can be written as the functional derivative of the xc part of $\tilde{\mathcal{A}}$,

$$V_{\text{xc}}(\mathbf{r}, t) = \left. \frac{\delta \tilde{\mathcal{A}}_{\text{xc}}}{\delta \rho(\mathbf{r}, \tau)} \right|_{\rho(\mathbf{r}, t)}, \quad (1.38)$$

where τ is the Keldish pseudo-time.

As the ground-state DFT, the explicit form of the time-dependent exchange-correlation potential $V_{\text{xc}}(\mathbf{r}, t)$ is unknown. Moreover, our knowledge about the time-dependent V_{xc} is

less than that of the ground-state DFT, where very good functionals are available. The simplest of all is called the adiabatic local density approximation (ALDA) where the value of V_{xc} at point \mathbf{r} and time t is equal to the V_{xc} of a static homogeneous electron gas (HEG) of density $\rho(\mathbf{r}, t)$ that is,

$$V_{\text{xc}}(\mathbf{r}, t) = V_{\text{xc}}^{\text{HEG}}(\rho)|_{\rho=\rho(\mathbf{r}, t)}. \quad (1.39)$$

Following the same procedure it is simple to derive an adiabatic GGA that includes the gradient correction, $\nabla\rho(\mathbf{r})$, as widely used in the ground-state DFT.

From the density obtained by TDDFT within ALDA/GGA level, we are able to obtain the time-dependent polarizability $\mathbf{p}(t)$ of a system with a given external time-dependent potential, in which essentially *all* information of the system interacting with the external field is contained.

Chapter 2

NONLINEAR RESPONSE FUNCTION IN THE TIME AND FREQUENCY DOMAIN

2.1 *Description of Optical Response*

Optical phenomena on materials enable the study of the modification of the optical properties of a system by the presence of the external field or simply light. We can “enjoy” the color of light we observe in everyday life, or even utilize and control the light as we desire. Indeed, the utilization of light has unlimited potential, in the same way we see in electronics. The emerging field of engineering light is called photonics. The optical nonlinearity is as important as the electrical nonlinearity.

A precise description of the microscopic optical response involves consideration of the change in the induced dipole moment $\mathbf{p}(t)$ of a medium on the strength $\mathbf{E}(t)$ of an applied field. The conventional linear and static response is

$$\mathbf{p} = \alpha \mathbf{E}, \quad (2.1)$$

where α is the polarizability. In the bulk system, the response is considered in terms of the dipole moment per unit volume. Here, we will study the microscopic response and consider the dipole moment, $\mathbf{p}(t)$, response of a molecule of interest. In the case of a non-spherically symmetric molecule, the polarizability depends on the direction of the applied field and becomes a tensor $p_i = \alpha_{ij} E_j$, where $i, j, k \equiv x, y, z$ denotes the Cartesian axes and summations are implicit for repeated indices. In nonlinear optics, optical response can be described by generalizing Eq. (2.1) as a power series in the field strength \mathbf{E} . Here, we write in terms of the total dipole moment \mathbf{p} ,

$$p_i = \mu_i + \alpha_{ij} E_j + \beta_{ijk} E_j E_k + \gamma_{ijkl} E_j E_k E_l + \dots, \quad (2.2)$$

where μ_i is the permanent dipole moment, α is the linear polarizability, β and γ are the first- and the second-hyperpolarizabilities (second- and the third-order nonlinearity), respectively.

2.2 Time-domain Response Function

For time-dependent applied fields $\mathbf{E}(t)$, the static expansion of Eq. (2.2) must be modified in several respects, since there is always a finite time lag in the response of a dispersive medium. Here, we can safely assume the interaction is local in space and ignore nonlocality. This approximation is valid when the wavelength of the optical waves of interest is long compared to the range of the response functions $\chi^{(n)}$ considered below. This approximation is appropriate for typical optical devices where the wavelength of visible light $\lambda \approx 5000 \text{ \AA}$ is much longer than typical length scale of the organic molecules ($\approx 100 \text{ \AA}$). Then the most generic extension of the static-nonlinear response to the time-dependent case becomes

$$\begin{aligned} p_i(t) = & \mu_i + \int dt_1 \chi_{ij}^{(1)}(t; t_1) E_j(t_1) \\ & + \int dt_1 \int dt_2 \chi_{ijk}^{(2)}(t; t_1, t_2) E_j(t_1) E_k(t_2) \\ & + \int dt_1 \int dt_2 \int dt_3 \chi_{ijkl}^{(3)}(t; t_1, t_2, t_3) E_j(t_1) E_k(t_2) E_l(t_3) + \cdots \end{aligned} \quad (2.3)$$

$$\equiv p_i^{(0)} + p_i^{(1)}(t) + p_i^{(2)}(t) + p_i^{(3)}(t) + \cdots, \quad (2.4)$$

where $p_i^{(0)} = \mu_i$ is the permanent dipole, $p_i^{(1)}(t)$ is linear in the field strength, $p_i^{(2)}(t)$ is quadratic, and so on. The equation above also defines the “microscopic” quantities $\chi^{(1)}$ of the linear response function, as well as $\chi^{(2)}$ and $\chi^{(3)}$ of the second- and third-order nonlinear response functions.

2.2.1 Linear response

The general form of the each term in the series Eq. (2.4) can be found by the fundamental principle of time-invariance symmetry. The meaning of time-invariance symmetry is that dynamical properties of the system are assumed to be unchanged by a translation of the origin of the time, or, simply says that *when* the interaction occurs is unimportant as long as we have the same initial condition. The linear polarizability is given by

$$p_i^{(1)}(t) = \int_{-\infty}^{\infty} dt_1 \chi_{ij}^{(1)}(t; t_1) E_j(t_1). \quad (2.5)$$

The time-invariance symmetry imposes the quantity $\chi_{ij}^{(1)}(t; t_1)$ depends only on the *difference* between the times t and t_1 . Hence, the time-invariance implies the linear response

function of Eq. (2.5) as follows:

$$p_i^{(1)}(t) = \int_{-\infty}^{\infty} dt_1 \chi_{ij}^{(1)}(t - t_1) E_j(t_1). \quad (2.6)$$

There are two important restrictions imposed on the response function. The first is the causality condition where $\mathbf{p}^{(1)}(t)$ depends only on the values of the field before t ; so that $\chi_{ij}^{(1)}(t)$ must be zero for $t < 0$. The second is the reality condition where $\mathbf{E}(t)$ and $\mathbf{p}^{(1)}(t)$ are both real, so that as the response function must also be real.

2.2.2 Nonlinear Response

Similar to the linear response function, we can apply the symmetry requirements to the second- and third-order nonlinear response functions,

$$p_i^{(2)}(t) = \int_{-\infty}^{\infty} dt_1 \int_{-\infty}^{\infty} dt_2 \chi_{ijk}^{(2)}(t; t_1, t_2) E_j(t_1) E_k(t_2) \quad (2.7)$$

and

$$p_i^{(3)}(t) = \int_{-\infty}^{\infty} dt_1 \int_{-\infty}^{\infty} dt_2 \int_{-\infty}^{\infty} dt_3 \chi_{ijkl}^{(3)}(t; t_1, t_2, t_3) E_j(t_1) E_k(t_2) E_l(t_3). \quad (2.8)$$

The nonlinear response functions appear in Eq. (2.7) and Eq. (2.8) as not uniquely determined, since there are permutation symmetries of the applied field $\mathbf{E}(t)$ that may appear in different order. To see this for the second-order response function, we write $\chi_{ijk}^{(2)}(t; t_1, t_2)$ as the sum of a symmetric part and an antisymmetric part,

$$\chi_{ijk}^{(2)}(t; t_1, t_2) = \chi_{ijk}^{S(2)}(t; t_1, t_2) + \chi_{ijk}^{A(2)}(t; t_1, t_2), \quad (2.9)$$

where

$$\chi_{ijk}^{S(2)}(t; t_1, t_2) = \frac{1}{2} \left[\chi_{ijk}^{(2)}(t; t_1, t_2) + \chi_{ikj}^{(2)}(t; t_2, t_1) \right] \quad (2.10)$$

and

$$\chi_{ijk}^{A(2)}(t; t_1, t_2) = \frac{1}{2} \left[\chi_{ijk}^{(2)}(t; t_1, t_2) - \chi_{ikj}^{(2)}(t; t_2, t_1) \right], \quad (2.11)$$

which are symmetric and antisymmetric under the interchanging the pairs of variables (j, t_1) and (k, t_2) . Such an interchange does not affect the expression of Eq. (2.7). It follows that

$\chi_{ijk}^{A(2)}(t; t_1, t_2)$ makes no contribution to $p_i^{(2)}(t)$ and the antisymmetric part is arbitrary. We set the antisymmetric part to zero to remove arbitrariness and to make $\chi_{ijk}^{(2)}(t; t_1, t_2)$ unique such that

$$\chi_{ijk}^{(2)}(t; t_1, t_2) = \chi_{ijk}^{(2)}(t; t_2, t_1). \quad (2.12)$$

We can make the same conclusion for the third-order response function $\chi_{ijkl}^{(3)}(t; t_1, t_2, t_3)$ to have 3! permutation symmetry for the variables t_1 , t_2 , and t_3 .

By the principle of time-invariance similar to the construction of the linear response function, we conclude that $\chi_{ijk}^{(2)}(t; t_1, t_2)$ depends only on the two time differences $t - t_1$ and $t - t_2$, and similarly $\chi_{ijkl}^{(3)}(t; t_1, t_2, t_3)$ depends only on the three time differences $t - t_1$, $t - t_2$, and $t - t_3$. Those define our second- and third-order nonlinear response function,

$$\chi_{ijk}^{(2)}(t; t_1, t_2) \equiv \chi_{ijk}^{(2)}(t - t_1, t - t_2) \quad (2.13)$$

and

$$\chi_{ijkl}^{(3)}(t; t_1, t_2, t_3) \equiv \chi_{ijkl}^{(3)}(t - t_1, t - t_2, t - t_3) \quad (2.14)$$

or by the substitution on Eq. (2.7) and Eq. (2.8),

$$p_i^{(2)}(t) = \int_{-\infty}^{\infty} dt_1 \int_{-\infty}^{\infty} dt_2 \chi_{ijk}^{(2)}(t - t_1, t - t_2) E_j(t_1) E_k(t_2) \quad (2.15)$$

and

$$p_i^{(3)}(t) = \int_{-\infty}^{\infty} dt_1 \int_{-\infty}^{\infty} dt_2 \int_{-\infty}^{\infty} dt_3 \chi_{ijkl}^{(3)}(t - t_1, t - t_2, t - t_3) E_j(t_1) E_k(t_2) E_l(t_3). \quad (2.16)$$

Both causality and reality conditions also apply to the nonlinear response functions. Moreover, we further have “intrinsic permutation symmetry” for the interchanges of the two pairs (j, t_1) and (k, t_2) for $\chi_{ijk}^{(2)}(t - t_1, t - t_2)$, as well as the three pairs (j, t_1) , (k, t_2) , and (l, t_3) for $\chi_{ijkl}^{(3)}(t - t_1, t - t_2, t - t_3)$.

2.3 Frequency-domain Response Function

The time-domain linear and nonlinear response functions can be transformed to the frequency domain by Fourier transformation. We use the following definition of the Fourier

transformation:

$$E(\omega) = \int_{-\infty}^{\infty} dt E(t) e^{-i\omega t} \quad (2.17)$$

$$E(t) = \int_{-\infty}^{\infty} \frac{d\omega}{2\pi} E(\omega) e^{i\omega t}. \quad (2.18)$$

In summary, we found the time-domain response function expansion of the dipole moment as follows.

$$\begin{aligned} p_i(t) &= \mu_i + \int_{-\infty}^{\infty} dt_1 \chi_{ij}^{(1)}(t-t_1) E_j(t_1) \\ &\quad + \int_{-\infty}^{\infty} dt_1 \int_{-\infty}^{\infty} dt_2 \chi_{ijk}^{(2)}(t-t_1, t-t_2) E_j(t_1) E_k(t_2) \\ &\quad + \int_{-\infty}^{\infty} dt_1 \int_{-\infty}^{\infty} dt_2 \int_{-\infty}^{\infty} dt_3 \chi_{ijkl}^{(3)}(t-t_1, t-t_2, t-t_3) \\ &\quad \times E_j(t_1) E_k(t_2) E_l(t_3) + \cdots \end{aligned} \quad (2.19)$$

$$\equiv p_i^{(0)} + p_i^{(1)}(t) + p_i^{(2)}(t) + p_i^{(3)}(t) + \cdots, \quad (2.20)$$

where $p_i^{(1)}(t)$, $p_i^{(2)}(t)$, and $p_i^{(3)}(t)$ are respectively given in Eq. (2.6), Eq. (2.15), and Eq. (2.16).

Inserting Eq. (2.18) into the right-hand side of $p_i^{(1)}(t)$ we have,

$$\begin{aligned} p_i^{(1)}(t) &= \int_{-\infty}^{\infty} dt_1 \int_{-\infty}^{\infty} \frac{d\omega}{2\pi} \chi_{ij}^{(1)}(t-t_1) E_j(\omega) e^{i\omega t_1} \\ &= \int_{-\infty}^{\infty} \frac{d\omega}{2\pi} \int_{-\infty}^{\infty} dt_1 \chi_{ij}^{(1)}(t-t_1) e^{-i\omega(t-t_1)} E_j(\omega) e^{i\omega t} \end{aligned} \quad (2.21)$$

or

$$p_i^{(1)}(t) = \int_{-\infty}^{\infty} \frac{d\omega}{2\pi} \chi_{ij}^{(1)}(-\omega_\sigma; \omega) E_j(\omega) e^{i\omega t}, \quad (2.22)$$

where we have defined the linear response function in frequency domain as

$$\chi_{ij}^{(1)}(-\omega_\sigma; \omega) = \int_0^{\infty} d\tau \chi_{ij}^{(1)}(\tau) e^{-i\omega\tau}, \quad (2.23)$$

with the lower limit respects the causality condition $\chi_{ij}^{(1)}(\tau) = 0$ for $\tau < 0$ explicitly. The first frequency argument ω_σ in $\chi_{ij}^{(1)}(-\omega_\sigma; \omega)$ is the dependence of the inverse Fourier transformation of the left-hand side of Eq. (2.22) with $\int d\omega_\sigma / 2\pi p_i^{(1)}(\omega_\sigma) \exp(i\omega_\sigma t)$. The equality must be held for every frequency, hence we conclude that $\omega_\sigma = \omega$ for all ω and recover the usual frequency domain linear response,

$$p_i^{(1)}(\omega) = \chi_{ij}^{(1)}(-\omega_\sigma; \omega) E_j(\omega) \Big|_{\omega_\sigma=\omega}. \quad (2.24)$$

The nonlinear response can be obtained similarly, e.g. for Eq. (2.18) we have,

$$\begin{aligned}
p_i^{(2)}(t) &= \int_{-\infty}^{\infty} dt_1 \int_{-\infty}^{\infty} dt_2 \int_{-\infty}^{\infty} \frac{d\omega_1}{2\pi} \int_{-\infty}^{\infty} \frac{d\omega_2}{2\pi} \chi_{ijk}^{(2)}(t-t_1, t-t_2) \\
&\quad \times E_j(\omega_1) e^{i\omega_1 t_1} E_k(\omega_2) e^{i\omega_2 t_2} \\
&= \int_{-\infty}^{\infty} dt_1 \int_{-\infty}^{\infty} dt_2 \int_{-\infty}^{\infty} \frac{d\omega_1}{2\pi} \int_{-\infty}^{\infty} \frac{d\omega_2}{2\pi} \chi_{ijk}^{(2)}(t-t_1, t-t_2) \\
&\quad \times e^{-i\omega_1(t-t_1)} e^{-i\omega_2(t-t_2)} E_j(\omega_1) E_k(\omega_2) e^{i\omega_1 t} e^{i\omega_2 t} \\
&= \int_{-\infty}^{\infty} \frac{d\omega_1}{2\pi} \int_{-\infty}^{\infty} \frac{d\omega_2}{2\pi} \chi_{ijk}^{(2)}(-\omega_\sigma; \omega_1, \omega_2) E_j(\omega_1) E_k(\omega_2) e^{i\omega_\sigma t}, \quad (2.25)
\end{aligned}$$

where we have defined $\omega_\sigma = \omega_1 + \omega_2$ and the second-order response function in frequency domain is given by

$$\chi_{ijk}^{(2)}(-\omega_\sigma; \omega_1, \omega_2) = \int_0^\infty d\tau_1 \int_0^\infty d\tau_2 \chi_{ijk}^{(2)}(\tau_1, \tau_2) e^{-i(\omega_1 \tau_1 + \omega_2 \tau_2)}. \quad (2.26)$$

We can readily generalize this procedure to higher-order response functions. The result for the third-order response function is

$$\begin{aligned}
p_i^{(3)}(t) &= \int_{-\infty}^{\infty} \frac{d\omega_1}{2\pi} \int_{-\infty}^{\infty} \frac{d\omega_2}{2\pi} \int_{-\infty}^{\infty} \frac{d\omega_3}{2\pi} \chi_{ijkl}^{(3)}(-\omega_\sigma; \omega_1, \omega_2, \omega_3) \\
&\quad \times E_j(\omega_1) E_k(\omega_2) E_l(\omega_3) e^{i\omega_\sigma t}, \quad (2.27)
\end{aligned}$$

where $\omega_\sigma = \omega_1 + \omega_2 + \omega_3$ and the response function is given by

$$\chi_{ijk}^{(3)}(-\omega_\sigma; \omega_1, \omega_2, \omega_3) = \int_0^\infty d\tau_1 \int_0^\infty d\tau_2 \int_0^\infty d\tau_3 \chi_{ijkl}^{(3)}(\tau_1, \tau_2, \tau_3) e^{-i(\omega_1 \tau_1 + \omega_2 \tau_2 + \omega_3 \tau_3)}. \quad (2.28)$$

Chapter 3

METHOD OF CALCULATION (RT-TDDFT)

3.1 *Real-time Method in TDDFT*

The technique of linear response based on TDDFT is by now well-developed, and has been applied both to molecules and solid states [15, 38, 39, 18, 40, 41, 42, 43, 44, 45, 46, 47, 48, 49, 50, 51, 52]. The first *ab initio* calculation of real time and real space within TDLDA was by Yabana and Bertsch [15], who performed calculations of the linear response of sodium and lithium clusters and for the C₆₀ molecule. The photoabsorption cross-section and other optical constants are key quantities of interest in testing TDDFT, since they can be measured in high-precision spectroscopy experiments. Although nonlinear TDDFT has been studied theoretically and applied to a few systems [53, 54, 14, 13, 55, 56, 57, 58, 1], the nonlinear response of nano-scale molecular systems has been difficult to calculate quantitatively, since conventional frequency-space calculation becomes prohibitively difficult for the large systems which require elaborate summations over occupied and excited states. The advantage of RT-TDDFT becomes even more obvious for nonlinear response, since the calculations are no more difficult than that in linear response, and hence can be computationally simpler, only requiring the accurate description of the “occupied states” of the valence electrons. As an alternative, frequency-space TDDFT calculations of non-linear response have recently been carried out by Andrade *et al.* [1].

3.2 *Numerical Time Evolution*

The real-time method of computing the time evolution of the density $\rho(\mathbf{r}, t)$ from the time-dependent KS equation Eq. (1.34) relies heavily on the efficiency of the numerical integration method.

The equation of motion of the wave function in the SIESTA DFT code is reduced into that of the coefficients c_i of the non-interacting KS orbital basis ϕ_i , and Eq. (1.34) takes

the form

$$i \frac{\partial c}{\partial t} = S^{-1} H c, \quad (3.1)$$

where S is the overlap matrix between the orbitals. Thus Eq. (3.1) can be expressed formally as

$$c(t) = \hat{U}(t, 0) c(0) \quad (3.2)$$

$$= \hat{T} \exp \left(-i \int_0^t dt' S^{-1} H(t') \right) c(0), \quad (3.3)$$

where \hat{T} is the time-ordering operator. The above propagator can be calculated using various numerical time-integration algorithms. The total evolution operator \hat{U} in numerical algorithms is usually approximated using a small time step Δt ,

$$U(t, 0) \approx \prod_{n=0}^{N-1} U_n(\Delta t), \quad (3.4)$$

where $\Delta t = t/N$, N is the total number of time steps, and

$$U_n(\Delta t) = \exp \left[-i S^{-1} H(n\Delta t) \Delta t \right]. \quad (3.5)$$

The time step Δt must be chosen small enough such that $\Delta t \ll 1/\omega_0$ where ω_0 is the smallest natural frequency of transition of interests. In the case of optical response, it is usually bounded by the lowest dipole transition energy.

3.2.1 Crank-Nicholson Integration Algorithm

The approximation of the exponential in Eq. (3.3) following the Crank-Nicholson algorithm [59] for the coefficients $c(t + \Delta t)$ and $c(t)$ is given by

$$c(t + \Delta t) = \frac{1 - iS^{-1}H(t)\Delta t/2}{1 + iS^{-1}H(t)\Delta t/2} c(t) + \mathcal{O}(\Delta t^2). \quad (3.6)$$

The main advantage of this algorithm is that it maintains unitarity of the operator, i.e., the norm of the wave function is conserved explicitly, apart from roundoff errors. This permits to use a long time step, Δt , while still maintaining reasonable accuracy. This operator has time reversal symmetry, and conserves energy when Hamiltonian is not explicitly dependent on time.

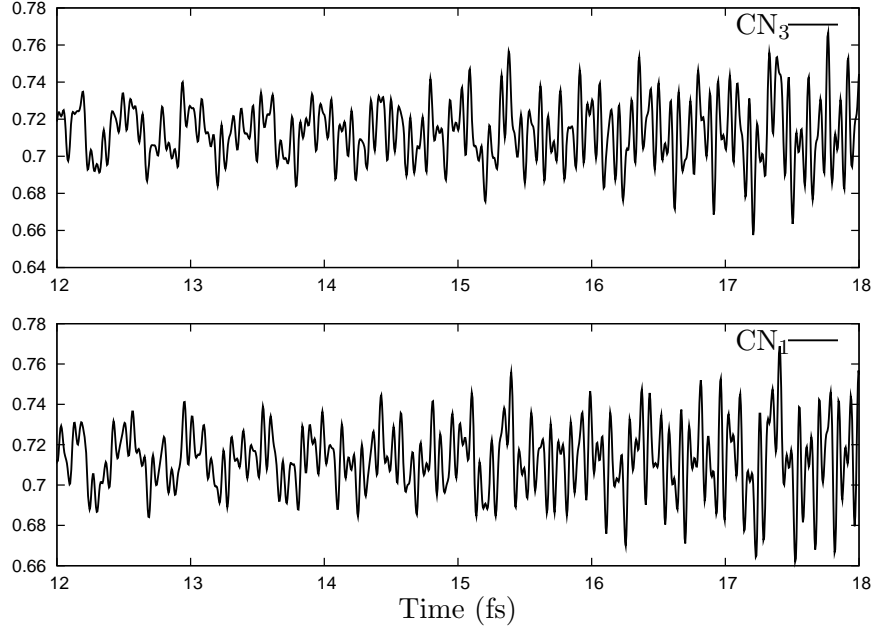


Figure 3.1: Addition of more expansion terms in the Crank-Nicholson operator. The evolution of dipole moment H_2O in time described as in Fig. 3.2 is evaluated with Eq. (3.6) labeled by CN_1 , and CN_3 with additional cubic term of Eq. (3.7). We have concluded that the additional term does not necessary help stability and the difference is too small to appear in the final optical spectra.

Addition of more terms in the expansion in the numerator and denominator of the Crank-Nicholson is suggested for stability [18], i.e.

$$c(t + \Delta t) = \frac{1 - iS^{-1}H(t)\Delta t/2 - 1/2(S^{-1}H(t)\Delta t/2)^2 + i1/6(S^{-1}H(t)\Delta t/2)^3}{1 + iS^{-1}H(t)\Delta t/2 - 1/2(S^{-1}H(t)\Delta t/2)^2 - i1/6(S^{-1}H(t)\Delta t/2)^3} c(t). \quad (3.7)$$

Making the evolution more stable is very important for the possibility of running longer simulations T as well as using larger time step Δt as both affect the accuracy and the runtime cost. In practice, we found that the addition of more terms does not actually help the stability, i.e. the use of operators of Eq. (3.6) and Eq. (3.7) start to diverges about the same time, but the difference is very subtle that appears the later part of a simulation as shown in Fig. 3.1. The difference is only visible on the final spectra at very high frequency above 100 eV ($\sim 1/\Delta t$). Therefore, we will not use the additional terms in the expansion, and will instead keep the simplest form. Note that two schemes start to diverge around 16 fs in this particular simulation setup.

3.2.2 Leapfrog Integration Algorithm

In an attempt to improve on the Crank-Nicholson algorithm, we also investigated an alternative approach for approximating the exponential which uses a “leapfrog” integration scheme [60]

$$c(t + \Delta t) = c(t - \Delta t) - 2i S^{-1} H c(t) \Delta t + \mathcal{O}(\Delta t^2). \quad (3.8)$$

Unfortunately, this method is not unitary, and it requires the use of sufficiently small time-steps to suppress the accumulation of error during the evolution. Since the overlap matrix S is fixed for a given atomic configuration, and only has to be inverted once, this method has the advantage of avoiding the need for inversion and only involves matrix multiplications during each time step. Despite this advantage, we found in practice that the Crank-Nicholson time evolution can be more efficient than the leapfrog method for small systems, e.g. those investigated here with fewer than 100 atoms. The reason is that the unitary property of the Crank-Nicholson operator allows one to use much larger time steps for the same degree of accuracy. In addition, although the number of numerical operations in each time step of the leapfrog method is smaller than that in the Crank-Nicholson operator, the most expensive part of the time evolution calculation in the RT-TDDFT is the preparation of the Hamiltonian $H(t)$, rather than the algebraic operations involved in the matrix inversion in $U_n(\Delta t)$. A collection of other commonly used time-evolution operators for the real-time approach is given by Martin [61]. Further review and detailed analysis of propagators for the time-dependent Kohn-Sham equations is also given by Castro *et al.* [62].

3.3 The Time-dependent External Field

The first step of calculating the response of a system to an arbitrary time-dependent external field is determined initially by applying a constant electric field \mathbf{E}_0 and find its ground-state density for time $t < 0$, where the Hamiltonian includes a dipole perturbation linear in \mathbf{E}_0 , $\Delta H = -\mathbf{E}_0 \cdot \mathbf{x}$. That is, the system is first solved for the ground-state of the system, including a fixed electric field, using conventional *time-independent* self-consistent DFT. Next, beginning at $t = 0$, we apply a time-dependent electric field $\mathbf{E}(t)$ and then compute the time-evolution of the system. For each time step, we solve the time-dependent KS

equation of Eq. (1.34) and form the new wave functions and subsequently the new density matrix

$$\rho^{\mu\nu}(t) = \sum_i^{\text{occ}} c_i^\mu c_i^\nu(t), \quad (3.9)$$

where c_i^μ are the coefficients of the occupied wave functions for the basis orbitals $\phi_\mu(\mathbf{r})$. The total charge density is then obtained as

$$\rho(\mathbf{r}, t) = \sum_{\mu, \nu} \rho^{\mu\nu}(t) \phi_\mu(\mathbf{r}) \phi_\nu(\mathbf{r}) \quad (3.10)$$

and used for the calculation of the Hamiltonian in the next time step. We update as well $\Delta H(t) = -\mathbf{E}(t) \cdot \mathbf{x}$ in every time step. Now, the total dipole moment at given time $\mathbf{p}(t)$ is

$$\mathbf{p}(t) = \int d^3\mathbf{r} \rho(\mathbf{r}, t) \mathbf{r}, \quad (3.11)$$

where $\mathbf{p}(t)$ defines the polarizability response to all orders. Fig. 3.2 illustrates the time evolution of the z -component of the polarization $p_z(t)$ for H_2O , in response to the step function external field.

3.4 The Static Finite Field Perturbation Theory

The usual technique for determining static polarizabilities is based on a fit to a perturbation expansion in the external electric field components of Eq. (2.2), again as follows:

$$p_i = \mu_i + \alpha_{ij} E_j + \beta_{ijk} E_j E_k + \gamma_{ijkl} E_j E_k E_l + \dots$$

The components of polarizability tensors are then calculated with finite field perturbation theory (FFPT) [63, 64] using five field strengths, $-2E$, $-E$, 0 , E , and $2E$, to obtain μ_i , α_{ij} , and β_{ijk} components (we do not demonstrate the calculation of γ_{ijkl} in this thesis) with the typical strength of electric field $E \sim 0.001$ (a.u.) for each axis direction, and then fitting to the 4th order polynomial to obtain the tensor components from the total dipole moment responses. This polynomial fitting method is usually the best and most practical way to eliminate the contamination from the higher-order terms that is often a problem with the finite difference method. This method enables one to calculate the first hyperpolarizability

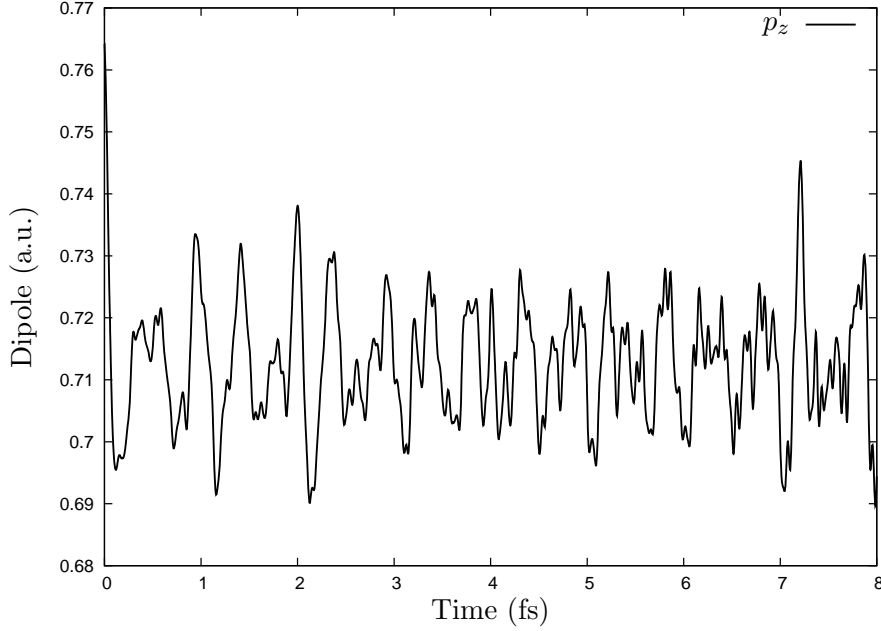


Figure 3.2: Time evolution of the dipole moment $\mathbf{p}(t)$ along the z -axis for H_2O , with a static \mathbf{E} field applied in the z -direction for $t < 0$ and turned off at $t = 0$. The z -axis is defined by the direction of permanent dipole of H_2O .

tensor components β_{iii} and β_{ijj} with $i, j = xyz$ but not β_{ijk} with $i \neq j \neq k$ components explicitly. In practice, either β_{ijk} with $i \neq j \neq k$ does not appear in the experimental averaging or it is negligibly small, and thus we will simply set it to zero.

3.4.1 Finite Difference Formula

If we need to evaluate all tensor components explicitly, the finite difference derivative formula will be more convenient. In particular, the numerical first-, second-, and third-derivatives of the total dipole moment p_i can be used to obtain α_{ij} , β_{ijk} , and γ_{ijkl} with given field strengths F .

$$\alpha_{ij} = [p_i(-2F_j) - 8p_i(-F_j) + 8p_i(F_j) - p_i(2F_j)]/12F_j \quad (3.12)$$

$$\beta_{ijj} = [-p_i(-2F_j) + 16p_i(-F_j) - 30p_i(0) + 16p_i(F_j) - p_i(2F_j)]/24F_j^2 \quad (3.13)$$

$$\beta_{ijk} = [p_i(-F_j, -F_k) - p_i(-F_j, F_k) - p_i(F_j, -F_k) + p_i(F_j, F_k)]/8F_jF_k \quad (3.14)$$

and

$$\begin{aligned}\gamma_{ijjj} = & [p_i(-3F_j) - 8p_i(-2F_j) + 13p_i(-F_j) \\ & - 13p_i(F_j) + 8p_i(2F_j) - p_i(3F_j)]/48F_j^3\end{aligned}\quad (3.15)$$

$$\begin{aligned}\gamma_{ijkk} = & [-90p_i(0) - 3p_i(-2F_k) + 48p_i(-F_k) + 48p_i(F_k) - 3p_i(2F_k) \\ & - 30p_i(-2F_j) - p_i(-2F_j, -2F_k) + 16p_i(-2F_j, -F_k) \\ & + 16p_i(-2F_j, F_k) - p_i(-2F_j, 2F_k) + 180p_i(-F_j) \\ & + 6p_i(-F_j, -2F_k) - 96p_i(-F_j, -F_k) - 96p_i(-F_j, F_k) \\ & + 6p_i(-F_j, 2F_k) - 60p_i(F_j, 0) - 2p_i(F_j, -2F_k) \\ & + 32p_i(F_j, -F_k) + 32p_i(F_j, F_k) - 2p_i(F_j, 2F_k)]/432F_jF_k^2,\end{aligned}\quad (3.16)$$

where $p_i(m F_j, n F_k)$ denotes the i -th component of total dipole moment response when fields are present in F_j and F_k direction with strength m and n .

3.5 The Time-dependent Finite Field Perturbation

For time-dependent applied fields, the FFPT must be modified in several respects, since there is always a finite time lag in the response of a dispersive medium. In particular, we are interested in the linear and nonlinear response functions appearing Eq. (2.19) in the time domain, as well as in the frequency domain Eq. (2.23), Eq. (2.26), and Eq. (2.28).

Instead of using the expansion of the total dipole moment $\mathbf{p}(t)$ as in Eq. (2.20), it becomes convenient to separate purely time-dependent function, $F(t)$, and the vector components of the electric field including its strength, E_i , and thus we write $E_i(t) = F(t)E_i$. The formula then takes a form similar to that for the static case,

$$p_i(t) = \mu_i + \tilde{p}_{ij}^{(1)}(t)E_j + \tilde{p}_{ijk}^{(2)}(t)E_jE_k + \tilde{p}_{ijkl}^{(3)}(t)E_jE_kE_l + \cdots, \quad (3.17)$$

where

$$\tilde{p}_{ij}^{(1)}(t) = \int_{-\infty}^{\infty} dt_1 \chi_{ij}^{(1)}(t-t_1)F(t_1), \quad (3.18)$$

$$\tilde{p}_{ijk}^{(2)}(t) = \int_{-\infty}^{\infty} dt_1 \int_{-\infty}^{\infty} dt_2 \chi_{ijk}^{(2)}(t-t_1, t-t_2)F(t_1)F(t_2), \quad (3.19)$$

$$\begin{aligned} \tilde{p}_{ijkl}^{(3)}(t) &= \int_{-\infty}^{\infty} dt_1 \int_{-\infty}^{\infty} dt_2 \int_{-\infty}^{\infty} dt_3 \chi_{ijkl}^{(3)}(t-t_1, t-t_2, t-t_3) \\ &\quad \times F(t_1)F(t_2)F(t_3). \end{aligned} \quad (3.20)$$

Hence, $\tilde{p}_{ij}^{(1)}(t)$, $\tilde{p}_{ijk}^{(2)}(t)$, and $\tilde{p}_{ijkl}^{(3)}(t)$ can be obtained using techniques similar to those for the static case. Thus, the relation to the response functions in the frequency domain are given by

$$\tilde{p}_{ij}^{(1)}(t) = \int_{-\infty}^{\infty} \frac{d\omega}{2\pi} \chi_{ij}^{(1)}(-\omega_\sigma; \omega) F(\omega) e^{i\omega t}, \quad (3.21)$$

$$\tilde{p}_{ijk}^{(2)}(t) = \int_{-\infty}^{\infty} \frac{d\omega_1 d\omega_2}{(2\pi)^2} \chi_{ijk}^{(2)}(-\omega_\sigma; \omega_1, \omega_2) F(\omega_1) F(\omega_2) e^{i\omega_\sigma t}, \quad (3.22)$$

$$\begin{aligned} \tilde{p}_{ijkl}^{(3)}(t) &= \int_{-\infty}^{\infty} \frac{d\omega_1 d\omega_2 d\omega_3}{(2\pi)^3} \chi_{ijkl}^{(3)}(-\omega_\sigma; \omega_1, \omega_2, \omega_3) \\ &\quad \times F(\omega_1) F(\omega_2) F(\omega_3) e^{i\omega_\sigma t}. \end{aligned} \quad (3.23)$$

By inverse fourier transform of the left-hand-side of the above equation and equating the integrand $\omega = \omega_\sigma$ for all ω , we have,

$$\tilde{p}_{ij}^{(1)}(\omega) = \chi_{ij}^{(1)}(-\omega; \omega) F(\omega), \quad (3.24)$$

$$\tilde{p}_{ijk}^{(2)}(\omega) = \int_{-\infty}^{\infty} \frac{d\omega_2}{2\pi} \chi_{ijk}^{(2)}(-\omega; \omega - \omega_2, \omega_2) F(\omega - \omega_2) F(\omega_2), \quad (3.25)$$

$$\begin{aligned} \tilde{p}_{ijkl}^{(3)}(\omega) &= \int_{-\infty}^{\infty} \frac{d\omega_2 d\omega_3}{(2\pi)^2} \chi_{ijkl}^{(3)}(-\omega; \omega - \omega_2 - \omega_3, \omega_2, \omega_3) \\ &\quad \times F(\omega - \omega_2 - \omega_3) F(\omega_2) F(\omega_3). \end{aligned} \quad (3.26)$$

We now recognize that $\chi_{ij}^{(1)}(-\omega; \omega) \equiv \alpha(\omega)$. Hence, the frequency-dependent linear response can be obtained from the Fourier transformation,

$$\chi_{ij}^{(1)}(-\omega; \omega) \equiv \frac{1}{F(\omega)} \int dt e^{-i\omega t - \delta t} P_{ij}^{(1)}(t) \quad (3.27)$$

$$F(\omega) = \int dt e^{-i\omega t} F(t), \quad (3.28)$$

where the damping factor $\delta > 0$ is introduced for computational efficiency in the Fourier transformation, and is chosen such that $e^{-\delta t_{max}} \ll 1$. One effect of this damping factor is a minimum width of the peaks in the imaginary part of the response, which physically can account for the experimental broadening Γ of the spectra taking $\Gamma = 2\delta$ (see Appendix Eq. (B.3)).

The imaginary part of the linear polarizability $\text{Im} \alpha(\omega)$ is directly related to the absorption cross-section $\sigma(\omega)$. In order to show the relation, we look at the dipole-strength function $S(\omega)$ which is also known as the oscillator strength density. From Fermi's golden rule, $S(\omega)$ can be expressed formally in terms of the exact eigenstates ν and energies ω_ν of the ground-state Hamiltonian,

$$S(\omega) = \sum_{\nu} |\langle \nu | \hat{d} | 0 \rangle|^2 \delta(\omega_\nu - \omega), \quad (3.29)$$

where \hat{d} is the dipole operator coupling the electrons to the electric field. The quantity $S(\omega)$ is also related to the imaginary part of frequency-dependent linear polarizability by [36]

$$S(\omega) = \frac{2\omega}{\pi} \text{Im} \frac{\text{Tr} \alpha_{ij}(\omega)}{3}. \quad (3.30)$$

Then, the imaginary part of the average linear polarizability is directly related to the absorption cross-section $\sigma(\omega)$,

$$\langle \text{Im} \alpha(\omega) \rangle = \frac{\pi}{2\omega} S(\omega) \propto \frac{\sigma(\omega)}{\omega}. \quad (3.31)$$

For the case of linear response, typical choices of $F(t)$ include the step function $\Theta(t)$ [18, 65] and the impulse delta function $I_\delta(t)$, i.e., $I_\delta(0) = 2/\Delta t$, and $I_\delta(t) = 0$ for $t \neq 0$ [15, 66, 65]. Both of these choices have Fourier components in frequency space which are non-zero and smoothly varying. Indeed, we have evaluated both of these choices for calculations of linear response and found them equally satisfactory in obtaining accurate absorption spectra.

3.6 Quasi-monochromatic Field Approximation

Because the above real-time approach for non-linear response only involves occupied states of the Hamiltonian $H(t)$ for determining linear and nonlinear polarizabilities, it is generally

much simpler computationally than perturbative methods, which require elaborate summations over excited states. Nevertheless the calculation of frequency-dependent nonlinear polarizabilities is still somewhat more involved than that for linear response. In particular, nonlinear response functions are convoluted with the external fields, and hence one cannot easily invert Eq. (3.24) for $\tilde{p}^{(n)}$ when $n > 1$. Thus one cannot obtain *all* components of the non-linear frequency response by simply applying a particular waveform such as the impulse delta-function only once. Moreover, a complete treatment of non-linear response would require an infinite sequence of such impulses.

Thus in order to develop an efficient approach for the case of nonlinear polarizabilities, we have found it convenient to use a wave-packet superposition of quasi-monochromatic waves of finite duration for the applied field. Then, from the previous results Eq. (3.22), (3.23) and (3.24), and the fact that the superposition of a complete-set of monochromatic wave is proportional to a delta function, we can write $E(\omega) \propto \sum_i a_i \delta(\omega - \omega_i)$. Thus, providing that the frequency dependence of $\chi^{(n)}(\omega)$ is slowly varying in the region of the applied monochromatic field frequency, we can eliminate the integrals and equate Fourier coefficients to obtain the relations

$$\tilde{p}_{ijk}^{(2)}(\omega_\sigma) = \frac{D^{(2)}}{2\pi} \chi_{ijk}^{(2)}(-\omega_\sigma; \omega_1, \omega_2) F_{\omega_1} F_{\omega_2}, \quad (3.32)$$

$$\tilde{p}_{ijkl}^{(3)}(\omega_\sigma) = \frac{D^{(3)}}{(2\pi)^2} \chi_{ijkl}^{(3)}(-\omega_\sigma; \omega_1, \omega_2, \omega_3) F_{\omega_1} F_{\omega_2} F_{\omega_3}, \quad (3.33)$$

where we have assumed an impulse delta-function $F_{\omega'} \approx \delta(\omega - \omega')$ and the frequencies are related by the condition $\omega_\sigma = \omega_1 + \omega_2$ for $p^{(2)}$ and $\omega_\sigma = \omega_1 + \omega_2 + \omega_3$ for $p^{(3)}$. Here $D^{(n)}$ is a degeneracy factor that depends on the character of the input field. For example, $D^{(2)} = 1$ for indistinguishable fields and $D^{(2)} = 2$ for distinguishable fields. We also note that in the literature the Fourier components of the nonlinear polarization are often defined without the 2π factors [67]. Of course, this can be done consistently only when the inverse Fourier transform of $E(\omega)$ and $p(\omega)$ are also defined without the factors of 2π . However, the values of $\chi^{(n)}$ are the same for both definitions.

In carrying out real-time simulations of these quantities, applying pure sinusoidal varying external field in time is problematic because simulation is performed in finite time length. Instead we use quasi-monochromatic wave turning on and off adiabatically within a finite

time simulation, which corresponds inversely to the line width in frequency space. Thus assuming the material response is varying slowly within a band width δ of the input quasi monochromatic wave $F_\delta(\omega)$ that is sharply peaked at $\omega = \omega_0$, we can calculate the second harmonic response using the relation

$$\begin{aligned}\tilde{p}_{ijk}^{(2)}(2\omega_0) &= \int_{-\infty}^{\infty} \frac{d\omega_2}{2\pi} \chi_{ijk}^{(2)}(-2\omega_0; 2\omega_0 - \omega_2, \omega_2) F_\delta(2\omega_0 - \omega_2) F_\delta(\omega_2) \\ &\approx \chi_{ijk}^{(2)}(-2\omega_0; \omega_0, \omega_0) \int_{\omega_0 - \omega_c}^{\omega_0 + \omega_c} \frac{d\omega_2}{2\pi} F_\delta(2\omega_0 - \omega_2) F_\delta(\omega_2) \\ &= \chi_{ijk}^{(2)}(-2\omega_0; \omega_0, \omega_0) \int_{-\omega_c}^{\omega_c} \frac{d\omega'}{2\pi} F_\delta(\omega_0 - \omega') F_\delta(\omega_0 + \omega'),\end{aligned}\quad (3.34)$$

in the limit $\delta \rightarrow 0$ and the integration cut-off $\omega_c \rightarrow \infty$. Thus we have

$$\chi_{ijk}^{(2)}(-2\omega_0; \omega_0, \omega_0) = 2\pi \tilde{p}_{ijk}^{(2)}(2\omega_0) / F_\delta^{(2-)}(\omega_0) \quad (3.35)$$

$$F_\delta^{(2-)}(\omega_0) = \int_{-\omega_c}^{\omega_c} d\omega' F_\delta(\omega_0 - \omega') F_\delta(\omega_0 + \omega'). \quad (3.36)$$

Similarly, we can also calculate the DC ($\omega = 0$) nonlinear response by noting $F(-\omega) = F^*(\omega)$ for real $F(t)$.

$$\begin{aligned}\tilde{p}_{ijk}^{(2)}(0) &= \int_{-\infty}^{\infty} \frac{d\omega_2}{2\pi} \chi_{ijk}^{(2)}(0; -\omega_2, \omega_2) F_\delta(-\omega_2) F_\delta(\omega_2) \\ &= 2 \int_0^{\infty} \frac{d\omega_2}{2\pi} \chi_{ijk}^{(2)}(0; -\omega_2, \omega_2) F_\delta^*(\omega_2) F_\delta(\omega_2) \\ &\approx 2\chi_{ijk}^{(2)}(0; -\omega_0, \omega_0) \int_{\omega_0 - \omega_c}^{\omega_0 + \omega_c} \frac{d\omega_2}{2\pi} F_\delta^*(\omega_2) F_\delta(\omega_2),\end{aligned}\quad (3.37)$$

or

$$\begin{aligned}\chi_{ijk}^{(2)}(0; -\omega_0, \omega_0) &= \pi \tilde{p}_{ijk}^{(2)}(0) / F_\delta^{(2+)}(\omega_0), \\ &= \chi_{ijk}^{(2)}(-\omega_0; \omega_0, 0),\end{aligned}\quad (3.38)$$

$$F_\delta^{(2+)}(\omega_0) = \int_{-\omega_c}^{\omega_c} d\omega' F_\delta^*(\omega_0 + \omega') F_\delta(\omega_0 + \omega'), \quad (3.39)$$

where the last equality of the response function $\chi^{(2)}$ comes from the permutation symmetry (i.e., time-translation symmetry). Under the same assumption, similar relations may be derived for second hyperpolarizability $\gamma(-\omega, \omega_1, \omega_2, \omega_3)$ and for $\tilde{p}_{ijkl}^{(3)}(\omega)$. We remark that

the above equations may not converge smoothly to the static limit $\omega_0 \rightarrow 0$, since both denominator and numerator diverge; however, this does not appear to cause noticeable numerical problems, as we illustrate later. Also the band width δ in the calculations must be smaller than ω_0 , and there is a practical limit to real-time simulations, since a longer simulation time is needed to obtain sharper peaks at low frequency. The current practical limit in our code is a time duration on the order of 10^{-13} sec, which is needed when we have more than two oscillations in the envelope function of $F(t)$. This corresponds to a minimum frequency relation of about 0.08 eV or a wavelength of 16 μm .

3.7 Efficiency of RT-TDDFT Method

The great advantage of our real-time method in nonlinear calculations is its scalability. Typical calculations of nonlinear properties become prohibitively expensive as the number of electrons and thus a system grows; the cost of calculating the excited quantum states increases too rapidly, often with exponential growth. Our implementation of the RT-TDDFT method is based on using the ground-state $\mathcal{O}(N)$ method at each time step, so updating KS Hamiltonian operator in each time step may be performed essentially in $\mathcal{O}(N)$. Here we use the symbol N with subscripts for quantities that scale roughly as number of atoms, and M for quantities are costly but independent of the system size. The total cost of calculating the response in RT-TDDFT is $\mathcal{O}(M_t M_\omega M_F (N_{op} + N))$ where M_t is the number of time steps, M_ω is the number of frequencies to be calculated, M_F is the number of the external field strengths that needs to be calculated to determine each hyperpolarizability tensor component, and N_{op} is the operation cost for time-step forwarding. Since M_t , M_ω , and M_F are independent of system size, the calculation scales as the sum of $\mathcal{O}(N)$ ground-state calculation and $\mathcal{O}(N_{op})$. Here N_{op} in the Crank-Nicholson matrix inversion scheme is $\mathcal{O}(N^3)$. This potential bottleneck for a large system, however, can be improved with faster iterative schemes such as conjugate gradient if necessary. Indeed, when the system size is less than few hundred atoms the pre-factor in front of the Crank-Nicholson operator is much smaller than that of $\mathcal{O}(N)$ operation for preparing Hamiltonian and KS orbitals, usually a fraction of time comparing to the duration of time spend in ground-state calculation. The efficient scaling property of RT-TDDFT is essential for studying nonlinear properties of

large, complex molecules. We believe that this is currently the most efficient method for obtaining *ab initio* calculations at this level of accuracy for the large molecules of interest in NLO applications.

Chapter 4

ILLUSTRATION WITH SMALL MOLECULES

4.1 Details of Simulation Setup

We illustrate the implementation of our method by applying it to the following molecules, all of which have been well studied both experimentally and theoretically: CO, H₂O, CHCl₃, and *para*-nitroaniline (pNA). The main purpose of this calculation was to investigate the accuracy and explore possible limitations of our method in cases with a relatively small basis size. The experimental bond length $r_{\text{C-O}} = 1.13 \text{ \AA}$ is used for CO, $r_{\text{O-H}} = 0.957 \text{ \AA}$ and $\angle\text{HOH} = 104.5^\circ$ for H₂O, $r_{\text{CH}} = 1.0795 \text{ \AA}$, $r_{\text{CCl}} = 1.7814 \text{ \AA}$ and $\angle\text{HCCl} = 107.656^\circ$ for CHCl. We have used the optimized geometry for the pNA molecule with B3LYP aug-cc-pVDZ level, which yields sufficiently good agreement with the experimental geometry [68].

All atomic basis set uses Troullier-Martins GGA pseudopotentials and the PBE exchange-correlation functional [69]. Unless otherwise stated, the cut-off radius r_c is determined by requiring the energy shift $\delta\epsilon$ to be less than $0.5 \times 10^{-6} \text{ Har}$. The corresponding cut-off radius of the first- ζ orbitals are $r_c^s(\text{C}) = 9.33$, $r_c^p(\text{C}) = 12.91$, $r_c^s(\text{O}) = 7.17$, $r_c^p(\text{O}) = 9.93$, $r_c^s(\text{H}) = 12.18$, and $r_c^s(\text{N}) = 8.00$, $r_c^p(\text{N}) = 11.35$, where r_c^s and r_c^p are the cut-off radius for atomic s -orbital, and p -orbital, respectively. The additional polarization orbital has the same cut-off radius as the highest occupied angular momentum orbital. The cut-off radius used for this calculation for small molecules is as much as two times larger than typical cut-off values used in linear response. This is necessary for the hyperpolarizability calculation, as these quantities have non-negligible contributions from the regions far from the nuclei. An auxiliary real-space grid equivalent to a plane-wave cutoff of 60 Har is used in this calculation.

For the dynamic nonlinear studies carried out here, we have chosen a Gaussian enveloped sine wave, $F_\delta(t) = \exp[-(t - t_c)^2 \delta^2 / 2] \sin(\omega_0 t)$, which approaches a pure sine wave as

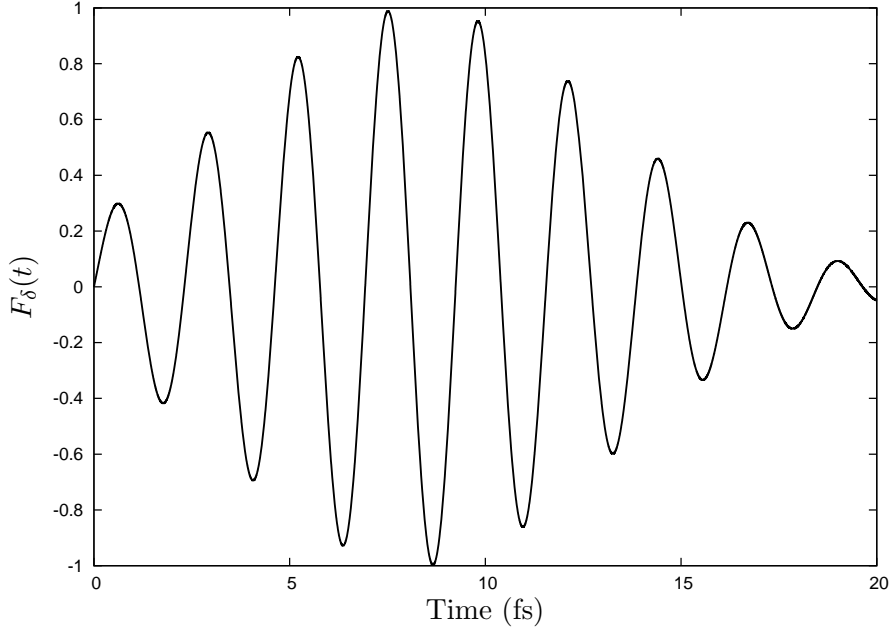


Figure 4.1: Quasi-monochromatic external field of the Gaussian enveloped sine wave $F_\delta(t) = \exp[-(t - t_c)^2 \delta^2 / 2] \sin(\omega_0 t)$ with $\omega_0 = 1.179$ eV, $\delta = 0.1$ eV, and t_c located at 40% of the total simulation time T .

$\delta \rightarrow 0$. The actual shape of our external field is shown in Fig. 4.1 for $\omega_0 = 1.79$ eV ($\lambda = 690$ nm). With this choice, the FWHM in frequency space is about 0.25 eV.

4.1.1 Convention

Our definitions of nonlinear optical properties as well as all theoretical and experimental values as reported here use convention B of Ref. [70] and all referenced values have been converted to this convention. Normally, the dipole moment is expanded as in Eq. (2.2):

$$p_i = \mu_i + \alpha_{ij} E_j + \beta_{ijk} E_j E_k + \gamma_{ijkl} E_j E_k E_l + \dots$$

The other commonly used convention is to expand the dipole moment as a Taylor series in power of \mathbf{E} , referred to as convention AB:

$$p_i = \mu_i + \alpha_{ij} E_j + \frac{1}{2!} \beta_{ijk} E_j E_k + \frac{1}{3!} \gamma_{ijkl} E_j E_k E_l + \dots \quad (4.1)$$

In order to compare with experimental measurements, various tensor averages are introduced for the first hyperpolarizability β . The experimental measurements of the nonlinear

coefficients of a molecule is often carried out in solution. However, a solution is centrosymmetric and hence does not produce macroscopic second-order nonlinearity. To break the symmetry, an external electric field is applied to the solution, and this produces an electric field induced second harmonic generation (EFISH). The EFISH experiment measures the quantity Γ defined by [71].

$$\Gamma = \gamma + \frac{\mu_0 \beta_{\parallel}}{3kT}, \quad (4.2)$$

where γ is a scalar measure of the second hyperpolarizability, μ_0 is the magnitude of the permanent dipole moment, kT is the thermal energy, and the symbol β_{\parallel} is the vector average of β_{ijk} given by

$$\beta_{\parallel} = \frac{3}{5}\beta_z = \frac{1}{5} \sum_i (\beta_{iiz} + \beta_{izi} + \beta_{zii}), \quad (4.3)$$

with z -axis defined by the direction of the dipole.

Another average is related to Hyper-Rayleigh scattering (HRS), which measures the rotational average of all the components of β_{ijk} . It is defined by [72]

$$\beta_{\text{HRS}}^2 = \frac{6}{35} \sum_i \beta_{iii}^2 + \frac{16}{105} \sum_{i \neq j} \beta_{iii} \beta_{ijj} + \frac{38}{105} \sum_{i \neq j} \beta_{ijj}^2 + \frac{16}{105} \sum_{ijk, \text{cyclic}} \beta_{ijj} \beta_{jkk} + \frac{20}{35} \beta_{ijk}^2, \quad (4.4)$$

where the summations over “ $i \neq j$ ” contain six summands each, and the summation over “ ijk, cyclic ” contains three summands ($\beta_{xxy}\beta_{yzz}, \beta_{yyz}\beta_{zxx}, \beta_{zzx}\beta_{xyy}$).

4.2 CO molecule

We begin our discussion with CO. Table 4.1 shows the results of static hyperpolarizabilities including comparison with the other theoretical calculation [73, 13, 74, 1] and experiments [75, 76].

We have included two data columns for two different basis sizes. The DZDP basis set consists of double- ζ plus two polarization functions that has two radial functions per each angular momentum for the occupied orbitals s and p type functions as well as polarization d type functions. The 5Z4P basis set has five- ζ plus four polarization that have five orbitals for s , and four orbitals for p and d type functions. As we can see from the table, our method can obtain as good results as the high-level wave function method of MP4, when a

Table 4.1: Comparison of static polarizabilities and hyperpolarizabilities of CO. The results are in the atomic unit (a.u.). Our results include two different basis sets, DZDP and 5Z4P.

	This work	This work	LDA^a	LDA	HF^d	MP4^d	CCSD(T)^d	Expt.
	DZDP	5Z4P						
μ	0.117	0.0975	0.0631		-0.1052	0.0905	0.057	0.0481 ^e
α_{xx}	11.54	12.00	12.55		11.25	12.00	11.97	
α_{zz}	14.68	15.45	15.82		14.42	15.53	15.63	
$\bar{\alpha}$	12.58	13.15	13.64	13.87 ^b	12.31	13.18	13.19	13.09 ^f
β_{xxz}	2.51	4.18	4.18	4.12 ^c	2.5	4.15	4.2	
β_{zzz}	15.25	14.23	16.67	16.76 ^c	15.6	14.2	15.0	
$\beta_{ }$	12.18	13.56	15.02	15.00 ^c	12.4	13.5	14.0	

^a LDA with the fully self-consistent solution of the Sternheimer equation from Ref. [1].

^b LDA basis set results from Ref. [13].

^c LDA basis set results from Ref. [74].

^d Finite difference results from Ref. [73].

^e Experimental value from Ref. [75].

^f Experimental value from Ref. [76].

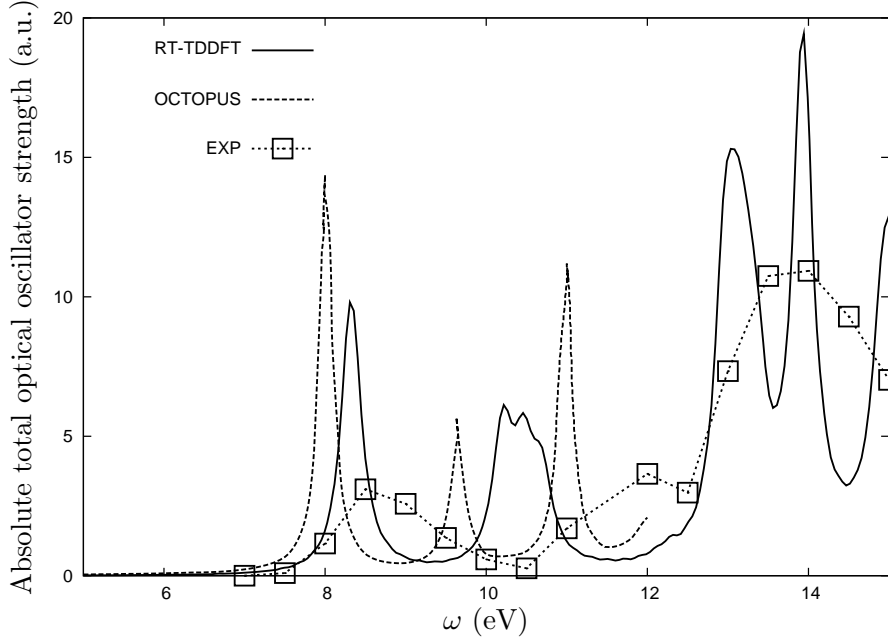


Figure 4.2: Average photoabsorption of the CO molecule calculated within the adiabatic GGA/PBE in real time, including broadening of $\delta = 0.3$ eV. The absolute total optical oscillator strength is normalized by the sum-rule (the valence electron count). TDDFT/ALDA OCTOPUS results from Ref. [1] (their data is available only up to 12 eV). The experimental results from Ref. [2].

sufficiently large basis set is used. This is remarkable given that our exchange-correlation function only includes GGA, rather than using a more complicated hybrid functional such as B3LYP.

For the dynamic properties, Fig. 4.2 shows the absorption cross section of the CO molecule and compares it to the dynamical calculation of the Stenheimer equation within TDDFT/ALDA using OCTOPUS code. From Fig. 4.2 both theoretical results are redshifted with respect to the experimental results. Indeed, OCTOPUS result is redshifted further than our result, which is likely due to the shortcoming of the LDA functional [77].

Table 4.3 and Fig. 4.3 shows our calculations of the frequency-dependent hyperpolarizabilities of CO along with the available experimental data and previous theoretical results. Note that our real-time results using the 5Z4P basis set (PBE functional) are in close agreement with the frequency domain TDDFT results using the hybrid B3LYP functional. This

Table 4.2: Absolute total optical oscillator strength for the $A^1\Sigma^+ \rightarrow A^1\Pi$ transition of CO. The value is determined from the integration of the dipole strength function $S(\omega)$ up to $\omega = 9.5$ eV. It yields the partial number of valence electron count for the transition.

Absolute optical oscillator strength for the $A^1\Pi$ state (unit of partial electron count)	
Theory	
Real-time TDDFT (This work)	0.17
Chantranupong <i>et al.</i> [78]	0.2250
Kirby and Cooper [79]	0.1636
Lynch <i>et al.</i> [80]	0.18
Nielsen <i>et al.</i> [81]	0.1208
Padial <i>et al.</i> [82]	0.342
Wood [83]	0.24
Coughran <i>et al.</i> [84]	0.14
Rose <i>et al.</i> [85]	0.11
Experiment	
Chan <i>et al.</i> [2]	0.1807
Eidelsberg <i>et al.</i> [86]	0.1941
Field <i>et al.</i> [87]	0.187
Lassettre and Skerbele [88]	0.1945

Table 4.3: Frequency-dependent hyperpolarizabilities of CO. Note that our result of smaller DZDP basis set turns out in undesired results that the value of $\beta_{\parallel}(0; -\omega, \omega)$ is higher than that of $\beta_{\parallel}(-2\omega; \omega, \omega)$.

ω (eV)	Real-time DZDP	Real-time 5Z4P	LDA ^a	HF ^a	B3LYP ^a	CCSD ^a	Expt.
$\beta_{\parallel}(0; 0, 0)$	12.18	13.56	15.41	12.50	14.02	12.71	
$\beta_{\parallel}(0; -\omega, \omega)$							
1.79	14.74	14.32	16.34	13.01	14.79	13.35	
1.96	14.83	14.47	16.54	13.11	14.96	13.49	
$\beta_{\parallel}(-2\omega; \omega, \omega)$							
1.79	13.64	16.62	18.52	14.11	16.58	14.78	15.1 ± 1.6^b
1.96	13.97	17.35	19.28	14.47	17.21	15.27	

^a LDA, B3LYP, HF, and CCSD results from Ref. [3].

^b Experimental value from Ref. [4].

agreement is somewhat unexpected since the B3LYP functional includes better correlation effects than the PBE functional. As a result, when two functionals are used within the same methodology, the results of the B3LYP functional is often better than that of the PBE functional. The frequency domain LDA results are known to overestimate the hyperpolarizabilities while HF results underestimate them. The best agreement with the experimental data is obtained by coupled cluster calculations using singles and doubles (CCSD).

In case of the frequency-dependent hyperpolarizabilities of CO, the real-time results with the small basis set of DZDP seems to have a problem, as the value of $\beta_{\parallel}(0; -\omega, \omega)$ is greater than that of $\beta_{\parallel}(-2\omega; \omega, \omega)$, which should not happen below the first resonant frequency; hence their values cannot be trusted for the comparison. To understand why the DZDP basis set is not adequate for this molecule, we have looked at the time-dependent behavior of the wave functions, and the evolution of orbital coefficients $c(t)$ as illustrated in Fig. 4.4 through Fig. 4.7. In the case of CO, only nonzero coefficients of this molecule on each atomic orbitals are $2s$ and $2p_z$ for the occupied valence electrons, and $2d_z$ for the polarization orbitals. The

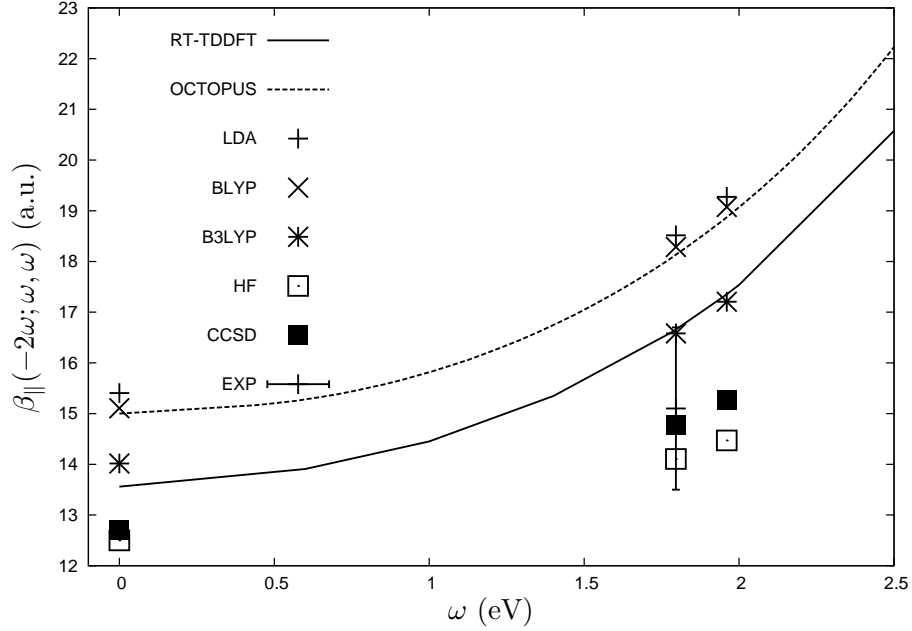


Figure 4.3: Second harmonic generation (SHG) $\beta_{||}(-2\omega; \omega, \omega)$ of CO. TDDFT/ALDA OCTOPUS results from Ref. [1]. LDA, BLYP, B3LYP, HF, and CCSD results from Ref. [3]. The experimental results from Ref. [4]

figures are produced by the step function field applying the constant electric field $\mathbf{E} = \mathbf{E}_0$ in $t < 0$ and set $\mathbf{E} = 0$ for $t \geq 0$. Fig. 4.4 and Fig. 4.5 respectively show the time evolution of the atomic C and the atomic O site with the DZDP basis set for $t \geq 0$ for the highest occupied molecular orbital (HOMO) state. The corresponding orbital energy is -9.11 eV for the 5Z4P basis set and -9.38 eV for the DZDP basis set. As is clear from the figures, all orbitals behave approximately like atomic energy eigenstates that oscillate sinusoidally at the fixed orbital energy and its period is about $T = 2\pi/\omega \sim 0.45$ fs. On the contrary, Fig. 4.6 and Fig. 4.7 show the same plot as the 5Z4P basis set. One of the most prominent changes is the $2p_z$ state on the Carbon atomic site. All four orbitals in that state are subtly different from the previous figures. This is because this $2p_z$ state form the molecular bond between the Carbon and Oxygen atomic sites. The problem with small basis set DZDP is that the contribution of first hyperpolarizabilities β comes mostly from the bond region rather than the atomic site, because β is identically zero for a spherically symmetric system

by the symmetry. The basis dependence will be discussed further with regard to CHCl_3 molecule in a subsequent section.

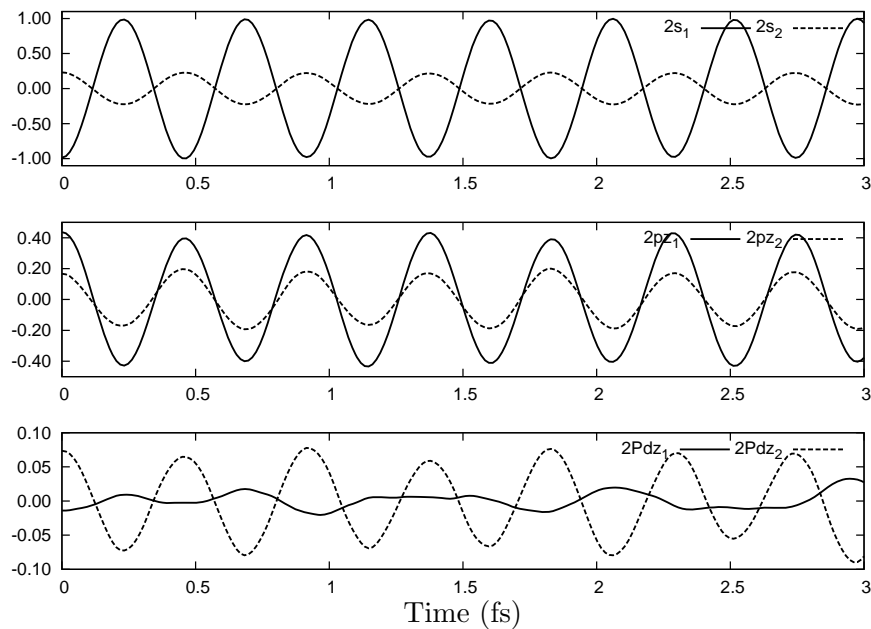


Figure 4.4: Evolution of orbital coefficients $c(t)$ of the Carbon atom for HOMO state in the CO molecule with the DZDP basis set (two radial functions per angular momentum). The z -axis defined along the bond direction.

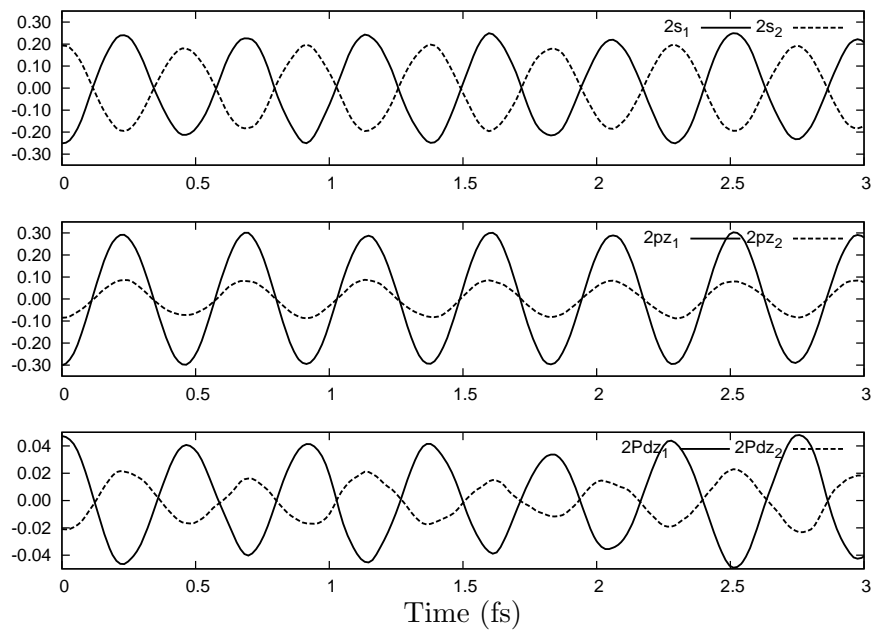


Figure 4.5: Evolution of orbital coefficients $c(t)$ of the Oxygen atom for HOMO state in CO molecule with the DZDP basis set (two radial functions per angular momentum). The z -axis defined along the bond direction.

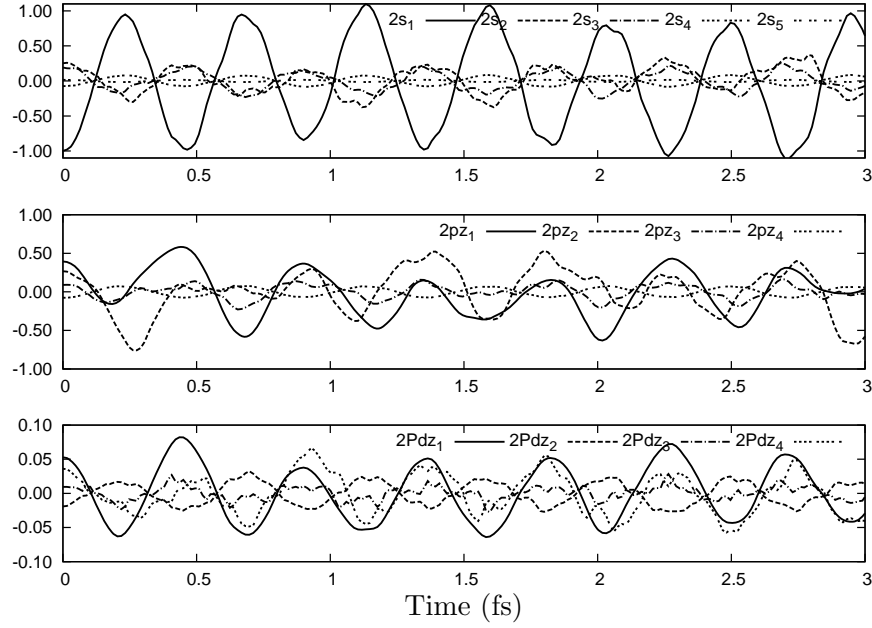


Figure 4.6: Evolution of orbital coefficients $c(t)$ of the Carbon atom for HOMO state in CO molecule with the 5Z4P basis set (five radial functions for s -state, four radial functions for p -state and polarization d -state). The z -axis defined along the bond direction.

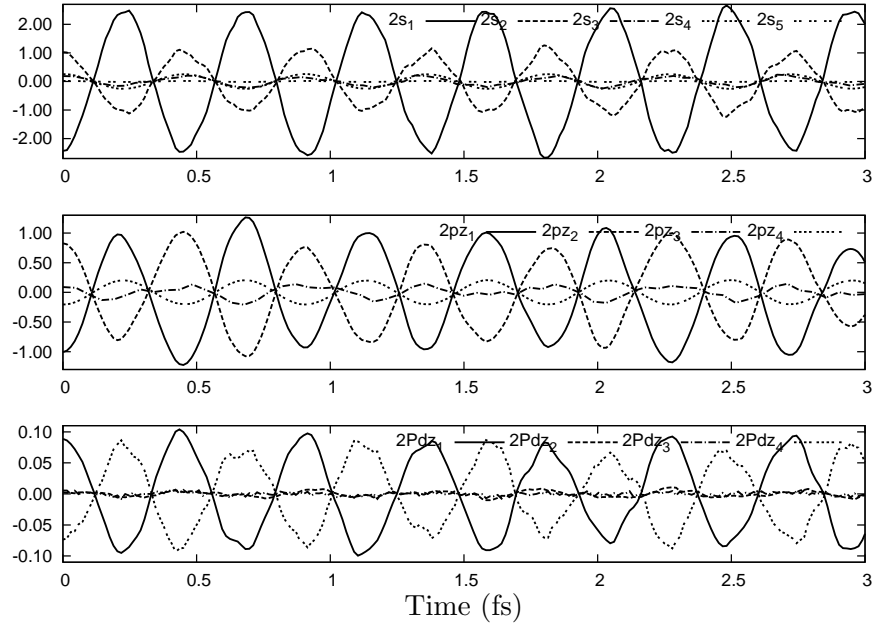


Figure 4.7: Evolution of orbital coefficients $c(t)$ of the Oxygen atom for HOMO state in CO molecule with the 5Z4P basis set (five radial functions for s -state, four radial functions for p -state and polarization d -state). The z -axis defined along the bond direction.

Table 4.4: Frequency-dependent (hyper)polarizabilities of H₂O.

ω (eV)	Real-time	TDLA ^a	LDA ^b	HF ^b	B3LYP ^b	CCSD ^b	Expt.
5Z4P							
μ_0	0.713						0.728 ^c
$\bar{\alpha}(0)$	10.38	10.51	10.59	8.53	10.00	9.65	
$\beta_{ }(0; 0, 0)$	-10.63	-12.95	-11.89	-5.37	-9.27	-8.87	
$\beta_{ }(0; -\omega, \omega)$							
1.79	-11.96	-14.17	-13.05	-5.64	-10.06	-9.45	
1.96	-12.27		-13.30	-5.70	-10.23	-9.58	
$\beta_{ }(-2\omega; \omega, \omega)$							
1.79	-14.45	-17.36	-16.06	-6.26	-12.06	-10.86	-10.45 \pm .5 ^d
1.96	-15.45	-17.62	-17.26	-6.48	-12.82	-11.38	

^a LDA with the fully self-consistent solution of the Sternheimer equation from Ref. [1].

^b LDA, B3LYP, HF, and CCSD results from Ref. [3].

^c Experimental value from Ref. [89].

^d Experimental value from Ref. [4].

4.3 H₂O molecule

We have summarized the results for H₂O dynamic first hyperpolarizabilities in Table 4.4, also shown in Fig. 4.14. The same trends can be seen as in previous calculations for CO, but the deviation is larger in the case of water. All DFT methods overestimate compared to the polarizability of the more accurate CCSD method. Our results lie between the LDA and B3LYP functional predictions. The HF results are about 40% underestimated while LDA overestimate by about 40-50%.

Unlike most of the frequency space methods, the real-time method can be applied at the resonant frequencies of both linear and nonlinear (hyper)polarizabilities. For the illustration of the resonant frequencies, we have explored the wide spectra of (hyper)polarizabilities for H₂O up to 10 eV. Fig. 4.9 shows the imaginary part of polarizability $\alpha(\omega)$, Fig. 4.10 shows the real part and Fig. 4.11 shows the imaginary part of the second harmonic generation

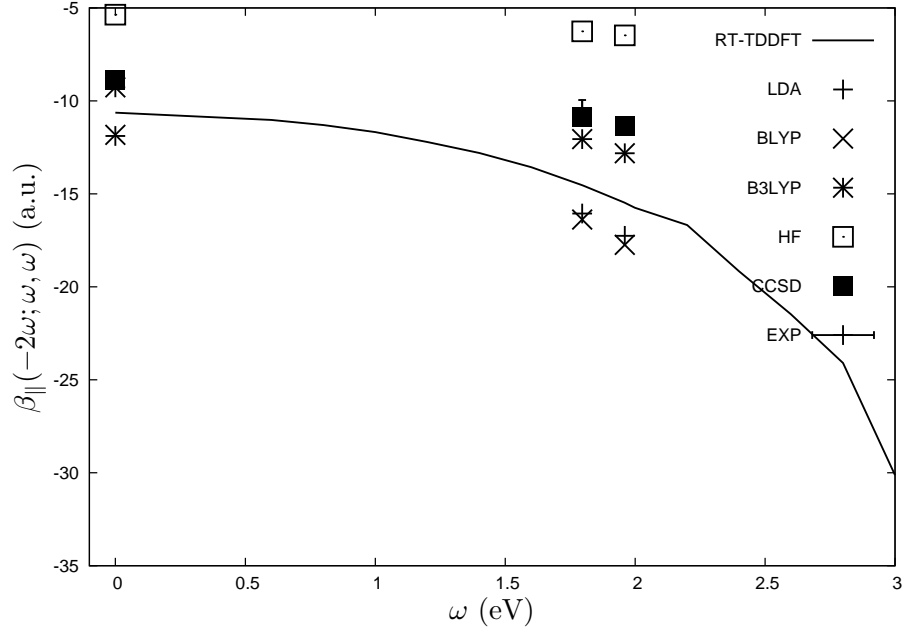


Figure 4.8: Second harmonic generation $\beta_{\parallel}(-2\omega; \omega, \omega)$ of H_2O . TDDFT/ALDA OCTOPUS results from Ref. [1]. LDA, BLYP, B3LYP, HF, and CCSD results from Ref. [3]. The experimental results from Ref. [4].

(SHG) spectra $\beta_{\parallel}(-2\omega; \omega, \omega)$, and Fig. 4.12 shows the real part of optical rectification (OR) spectra $-\beta_{\parallel}(0; \omega, -\omega)$. For the linear response, we can also calculate the response in real time with a standard step function field. Fig. 4.9 includes both spectra from fixed frequency response calculations (quasi-monochromatic) and the all frequency responses (step function) using the same broadening of about 0.1 eV. These results are essentially identical as expected, except that quasi-monochromatic spectra goes slightly negative around the resonant peaks.

Our result for OR spectra includes the comparison with Andrade *et al.*[1] which is based on the solution of a frequency-dependent Sternheimer equation. Their method also works on the resonant frequencies. The difference in the height is due to different damping introduced in the two methods. Notice that the shape of the real part of OR $-\beta_{\parallel}(0; \omega, -\omega)$ spectra is very similar to the shape of imaginary part of polarizability $\alpha(\omega)$.

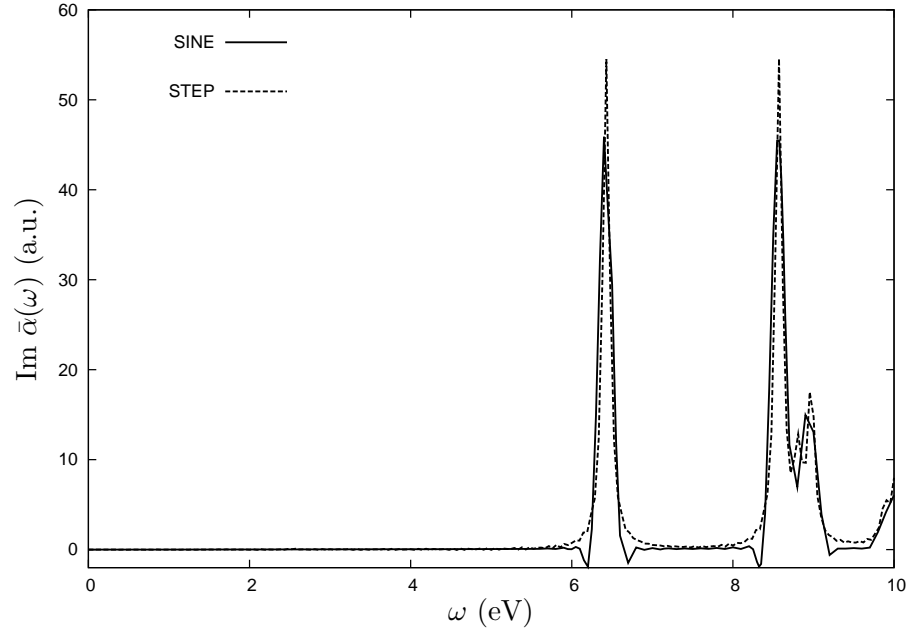


Figure 4.9: The imaginary part of average linear polarizability α of H_2O . The spectra with quasi monochromatic wave is calculated at each fixed frequency point. The spectra with the step function includes all frequency components with single real-time simulation. Both spectra include the same broadening of $\delta \approx 0.1$ eV.

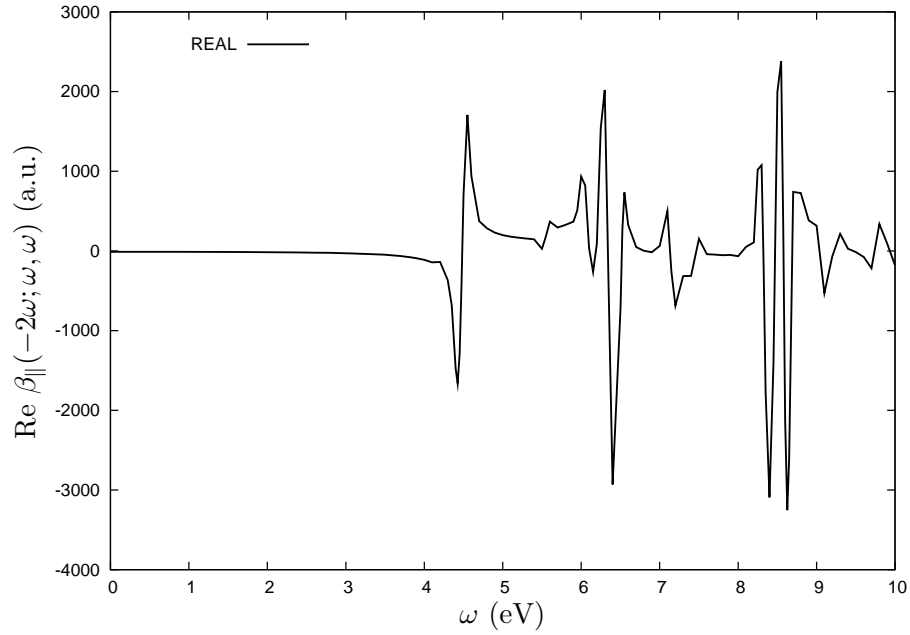


Figure 4.10: Second harmonic generation $\beta_{||}(-2\omega; \omega, \omega)$ of H_2O including optical resonant frequencies.

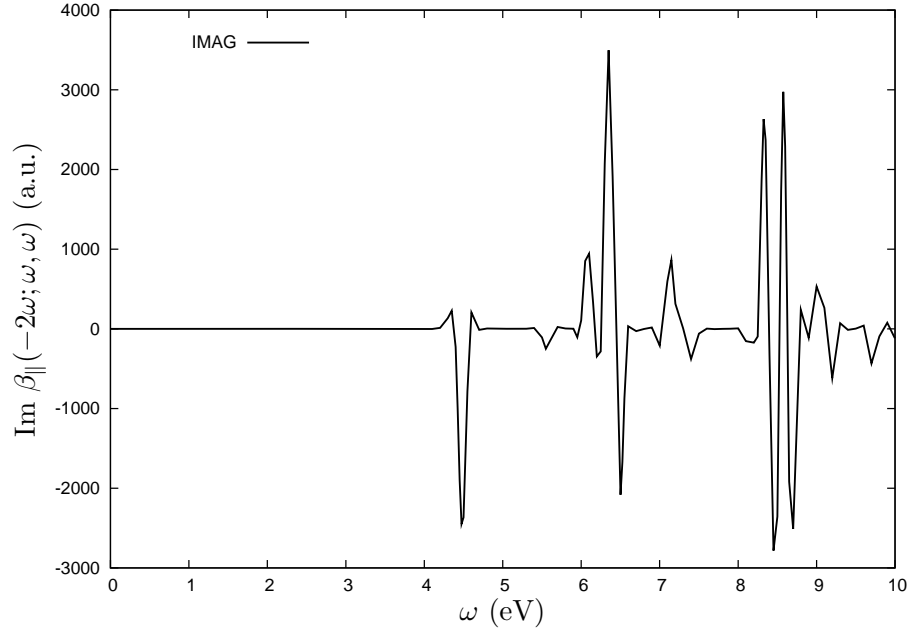


Figure 4.11: The imaginary part of the second harmonic generation coefficient $\beta_{||}(-2\omega; \omega, \omega)$ of H₂O including optical resonant frequencies.

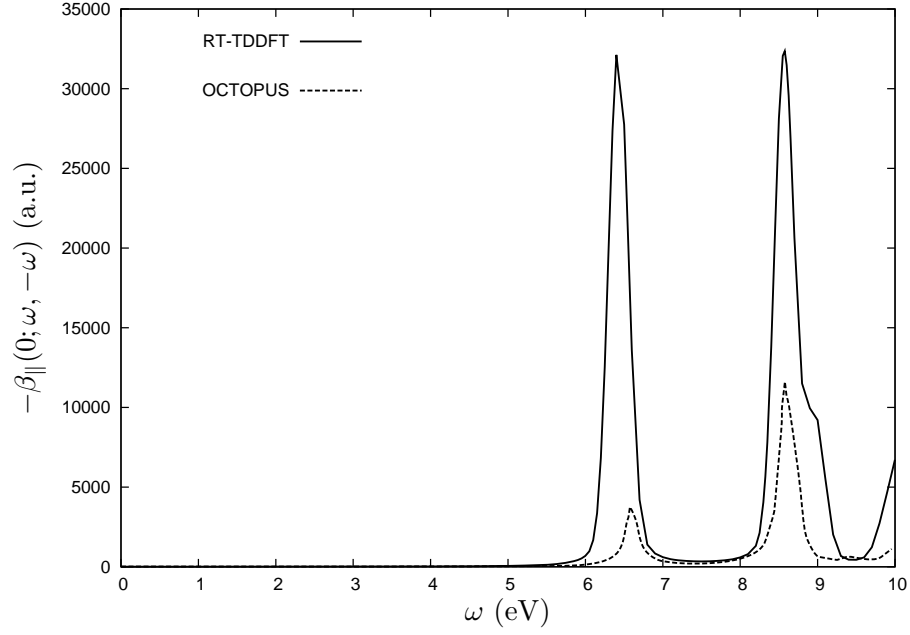


Figure 4.12: Optical rectification $\beta_{||}(0; \omega, -\omega)$ of H₂O including optical resonant frequencies. TDDFT/ALDA OCTOPUS results from Ref. [1].

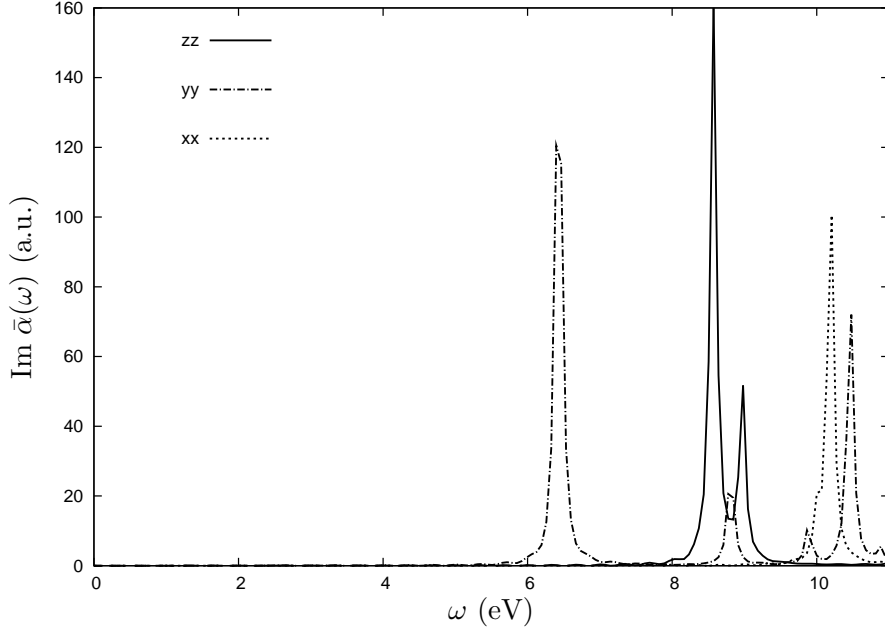


Figure 4.13: The imaginary part of diagonal parts of linear polarizability α of H_2O .

4.4 Resonant Frequencies (H_2O)

For the real-time method, it would be instructive to look further at the resonant behaviors in the time domain. Before looking at the time domain responses, we check the frequency response of each diagonal component of polarizability as shown in Fig. 4.13. Recall that the molecule is in the xz plane and the z -axis is the direction of dipole moment. The lowest excitation is from the hydrogen $1s$, and mainly from the oxygen $2p$ orbital out of the xz plane of molecule due to the “lone pair effects.” This is referred to as the $1b_1$ molecular orbital, and this direction of the absorption peak $\sigma \sim \text{Im } \alpha_{xx}(\omega)$ at 6.43 eV is the lowest among our results. The next lowest peak is $\alpha_{yy}(\omega)$ at 8.57 eV due to the direction of the dipole moment, or $3a_1$ molecular orbital. The peak of lowest $\alpha_{xx}(\omega)$ excitation, the $1b_2$ molecular orbital, only shows up after 10 eV.

The first hyperpolarizability β is the quadratic response to the external field \mathbf{E} . The response without preferred direction will vanish; hence, the only nonzero components for H_2O are β_{zzz} , $(\beta_{yyz} = \beta_{zyy})$, and $(\beta_{xxz} = \beta_{zxx})$.

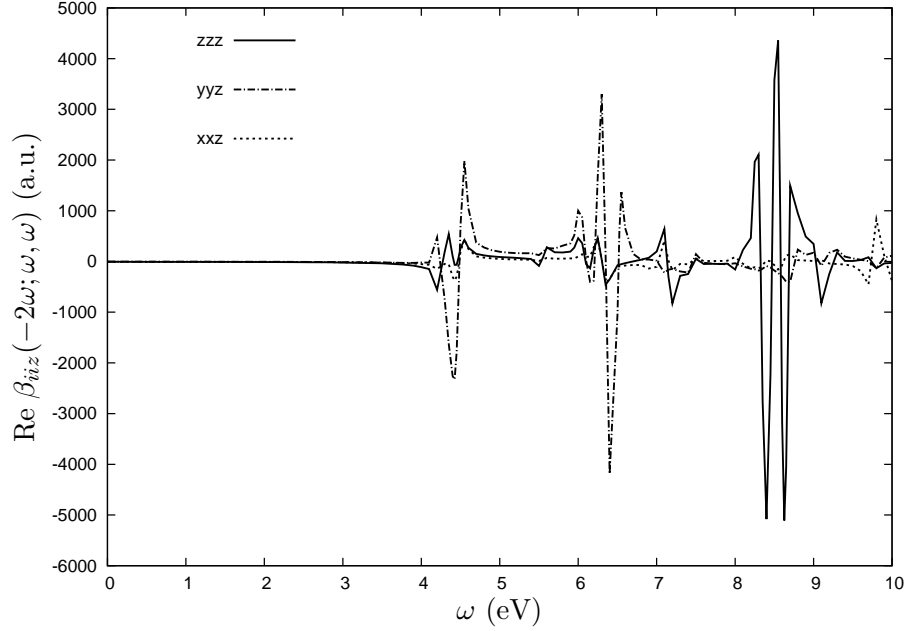


Figure 4.14: Second harmonic generation vector components along the dipole axis of $\beta_{ii}(-2\omega; \omega, \omega)$ of H_2O .

Fig. 4.14 shows the frequency responses of $\beta_{zzz}(\omega)$, $\beta_{yyz}(\omega)$, and $\beta_{xxz}(\omega)$ up to 10 eV. The lowest resonant peak at 4.5 eV is due to $\beta_{yyz}(\omega)$, which is related to the excitation of the $1b_1$ molecular orbital as in $\alpha_{yy}(\omega)$. The next prominent resonant peak is around 6.5 eV, coinciding with the absorption peak of $\alpha_{yy}(\omega)$; hence again it is dominated by the response of $\beta_{yyz}(\omega)$. The third resonant peak around 8.5 eV is due to $\beta_{zzz}(\omega)$ where coinciding with the lowest peak location of $\alpha_{zz}(\omega)$. As expected, the response of $\beta_{xxz}(\omega)$ is almost negligible for the energy, at less than 10 eV.

We now look at the time domain. Based on the frequency responses, the dominant component for the first hyperpolarizability in the time domain is the dipole moment in z direction p_z with applied external electric field in E_x , E_y , or E_z . Fig. 4.15 shows those responses when the external electric field $\mathbf{E}(\omega)$ with $\omega = 3.0$ eV. The broken line represents the quasi-monochromatic external field. The solid lines represent the dipole responses with two different field strengths in the positive direction ($E = 0.001$ and $E = 0.002$ in a.u.), whereas the lines shown with a long dash and dot correspond to applied electric field in

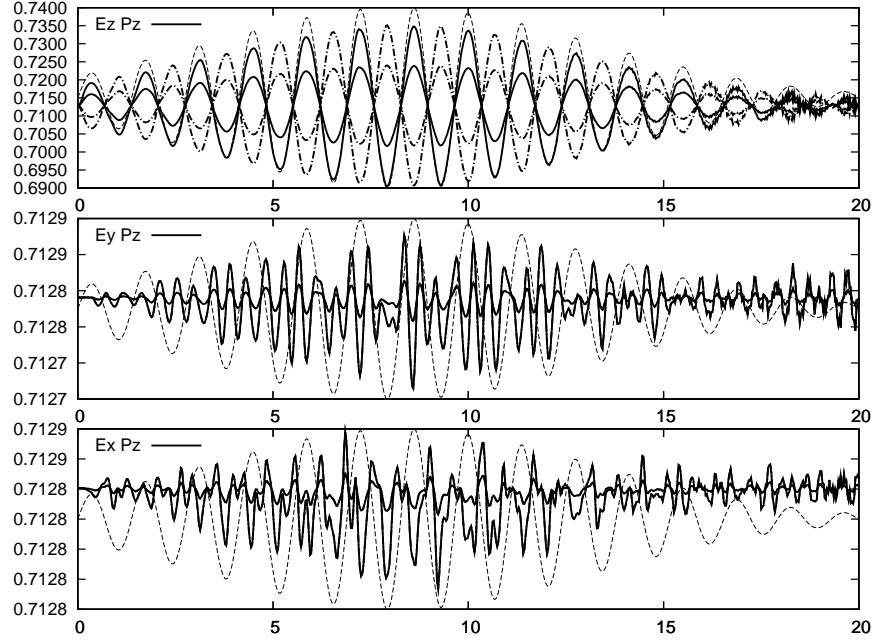


Figure 4.15: Dipole moment (a.u.) v.s. time (fs) with the external frequency $\omega = 3.0$ eV of H_2O .

the negative direction. Since the frequency of $\omega = 3.0$ eV is less than any of the resonant frequencies, the response in the time domain is dominated by the linear response, and no apparent response in p_z can be seen when E_y and E_z are applied, we will label those by (E_y, p_z) and (E_z, p_z) . Fig. 4.15 shows responses at $\omega = 4.5$ eV where the first peak resonant location of the $\beta_{yyz}(\omega)$ coefficient. It is now clear that (E_y, p_z) response is in resonance and is second order, as the frequency of response is twice that of the external field as well as nonlinear in the strength of the fields. We also observe the same resonant feature for (E_x, p_z) response, but in smaller magnitude. Fig. 4.17 shows responses at $\omega = 8.6$ eV where coinciding with the peak resonant location of the $\beta_{zzz}(\omega)$ coefficient. It is again clear that (E_z, p_z) response is in resonance and that oscillation is nonsymmetric and nonlinear in the strength of the field.

There is a technical problem with those resonant features when we try to Fourier transform the time domain responses. Since there is no natural damping mechanism in the simulation, as in Fig. 4.16 and Fig. 4.17, the resonant components continue to oscillate even

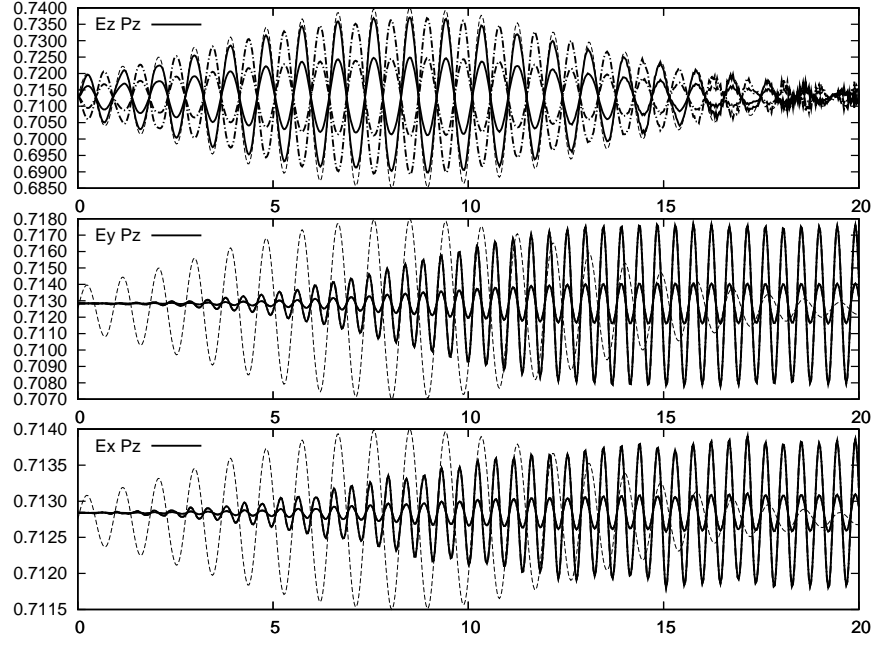


Figure 4.16: Dipole moment (a.u.) v.s. time (fs) with the external frequency $\omega = 4.5$ eV of H_2O . Location of the first resonant peak of the SHG.

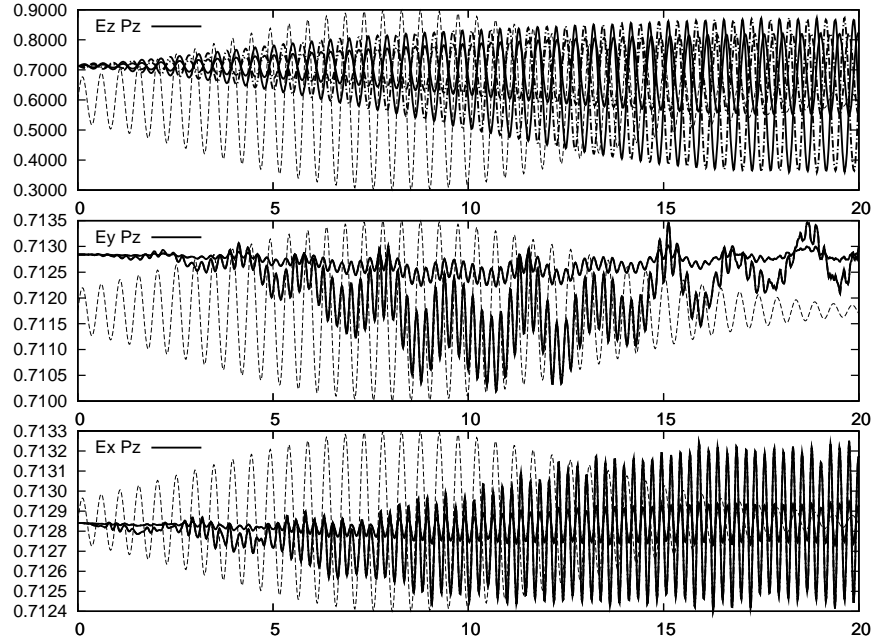


Figure 4.17: Dipole moment (a.u.) v.s. time (fs) with the external frequency $\omega = 8.6$ eV of H_2O . Resonant location for $\beta_{zzz}(\omega)$.

if driving field is no longer present. Since the simulation ends within a finite time, this abrupt cutoff the time domain simulation causes the Fourier ripple error in the frequency domain. The error is especially problematic for the OR spectra $\beta(0; \omega, -\omega)$ components. Unlike linear response, the exponential damping of the dipole signal in the time domain does not really work since there is nonzero external field for $t > 0$. If we simply add damping to the time domain signal when the external field is present, it would affect the magnitude of the dynamic hyperpolarizabilities, both on resonant and off resonant frequencies. To overcome this problem, we have introduced polynomial damping only toward the end of the simulation when the external field becomes negligible. More precisely, the third-order polynomial damping function is used only after the cut-off time t_c

$$p^{(n)}(\omega) \equiv \int_0^T dt e^{i\omega t} \left[1 - 3 \theta(t - t_c) \left(\frac{t - t_c}{T - t_c} \right)^2 + 2 \theta(t - t_c) \left(\frac{t - t_c}{T - t_c} \right)^3 \right] p^{(n)}(t), \quad (4.5)$$

where $\theta(x)$ is the step function which is equal to 0 for $x < 0$ and 1 for $x \geq 0$, and T is the total simulation time. We usually set the Gaussian envelope function of the central peak at $T/2$ and set $t_c = 0.9 * T$ to ensure introduction of this artificial damping will not affect non-resonant calculations.

Fig. 4.18 shows the OR spectra of $\beta_{||}(0; \omega, -\omega)$ near the first resonant frequency of the SHG with and without the damping function described above. The response of the OR spectra should not have any structure at this frequency. We see that there is unreal ripple if no damping is introduced, whereas the damping corrects the problem around the resonant regions and makes no effect in the non-resonant locations.

Another interesting feature of using a quasi-monochromatic wave to study the nonlinear properties is the harmonics of the envelope function itself. Fig. 4.19 shows such an effect for the (Ey, p_z) dipole response, as also seen in Fig. 4.17, in the time domain. We can see sub-harmonics and higher harmonics of the envelope function. Although we do not especially study this effect, this would have important application for the pulsed laser experiments.

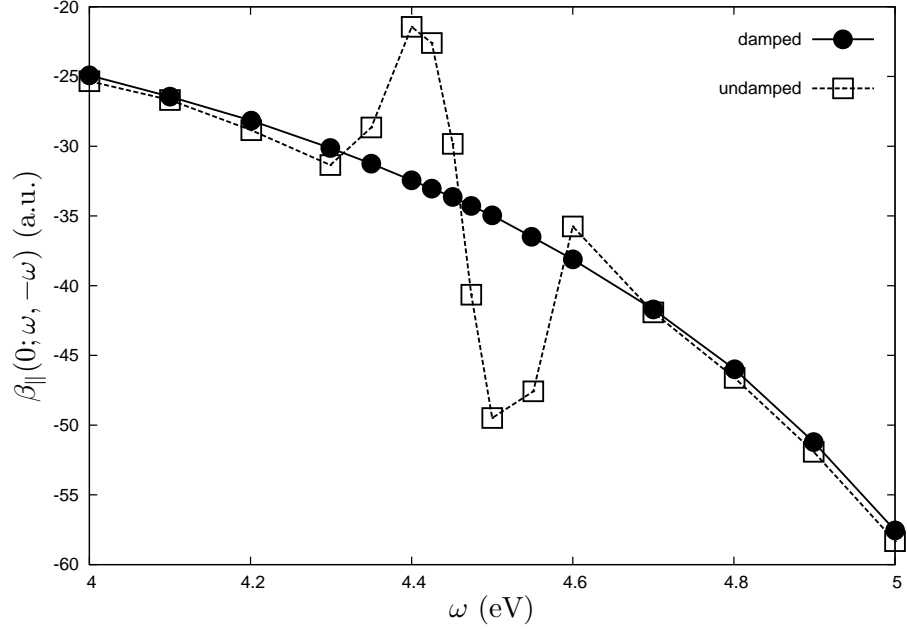


Figure 4.18: Optical rectification $\beta_{||}(0; \omega, -\omega)$ of H_2O around the lowest resonant frequency of the second harmonic generation.

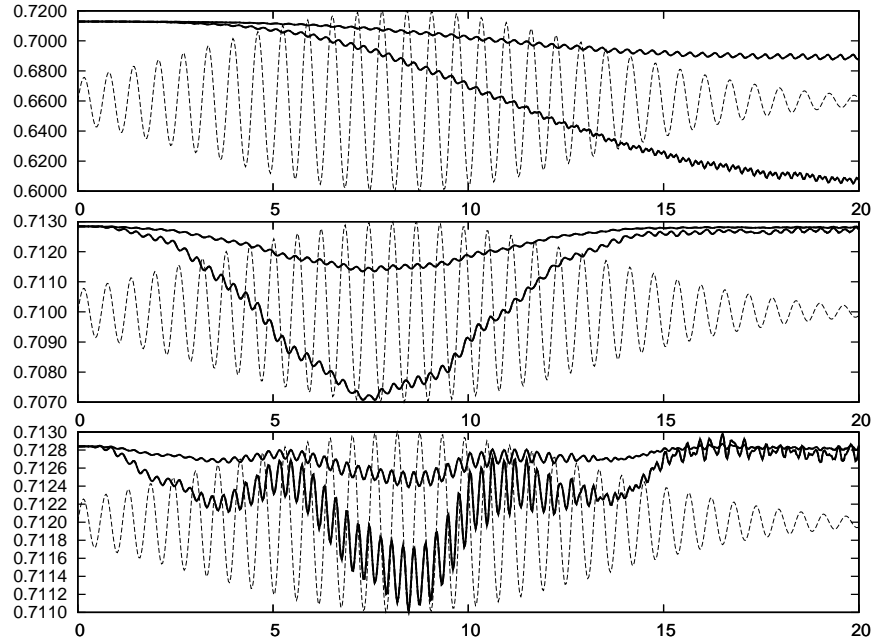


Figure 4.19: Dipole moment (a.u.) v.s. time (fs) with the external frequency $\omega = 6.5$ eV, 6.8 eV, and 7.2 eV of H_2O for (E_y, p_z) responses showing from the top.

4.5 CHCl_3 molecule and Basis Set Tests

Study of hyperpolarizabilities calculation of chloroform is especially of interest since this solvent is widely used for studying the performance of nonlinear organic molecules, such as chromophores. Hyperpolarizabilities of chromophores are usually measured by hyper-Rayleigh scattering (HRS) in a dilute solution of chloroform. HRS is the newly developed technique of characterizing a second harmonic generation of a sample molecule. HRS is the scattering of light at frequency 2ω when a liquid sample is illuminated by light at frequency ω [71]. The HRS method resolves two fundamental limitations in EFISH, that the molecules must have a permanent dipole moment and that they must not ionize in solution. In addition, unlike EFISH, the second harmonic scattered light is proportional to $\langle\beta^2\rangle$, so it does not require measuring μ or γ . The problem of HRS is the calibration. HRS cannot measure absolute values of the second harmonic coefficient $\beta(-2\omega; \omega, \omega)$ of the solute without knowing the absolute value of the reference molecule or solvent molecule.

For the theoretical hyperpolarizabilities calculation of this molecule, we found that the typical basis set used for this molecule is not adequate, as pointed out by Davidson *et al.* [90]. The result of basis set dependence is listed in Table 4.5.

Table 4.6 shows dependence on the energy shift $\delta\epsilon$ value which determines the cut-off radius of the first- ζ at each atomic site. The default energy shift is 0.01 Har, but this is usually inadequate for calculating nonlinear properties for small molecules. In the case of CHCl_3 , the value must be at least 0.5×10^{-6} Har, in order to have β_{\parallel} within the experimental value. The corresponding cut-off radius must be 2-3 times larger than the default setting. Indeed, the requirement of a large cut-off radius for the first- ζ is closely related to the requirement of a small splitnorm value for multiple- ζ . Away from the core region, the nonlinear properties are very sensitive to the extended region of the valence electron basis functions.

The various results using double- ζ basis set are obtained by varying the “splitnorm” parameter. The value of the ‘splitnorm’ parameter defines the amount of norm that the second- ζ split-off piece has to carry, and the corresponding split radius is defined accordingly. The last column 5Z4P basis includes five- ζ and has *all* split values (0.6, 0.15 0.015, and

Table 4.5: CHCl_3 permanent dipole moment, linear polarizabilities, and the first hyperpolarizabilities results with SIESTA. Study of dependence with splitnorm value. The splitnorm of 0.15 is the SIESTA default setting. The DZDP basis set is the double- ζ plus two polarization functions. The 5Z4P basis set includes five- ζ with splitnorm of 0.6, 0.15, 0.015, and 0.0015. The “splitnorm” is a parameter for constructing the second- ζ . The value defines the amount of norm that the second- ζ split-off from the first- ζ has to carry, and the corresponding split radius is defined accordingly. All are calculated with energy shift of 0.5×10^{-7} for the first- ζ .

	DZDP	DZDP	DZDP	DZDP	5Z4P
splitnorm	0.6	0.15	0.015	0.0015	
μ_z	0.383	0.388	0.360	0.354	0.402
α_{xx}	57.565	64.448	63.887	61.256	66.937
α_{yy}	57.563	64.492	63.888	63.555	66.939
α_{zz}	39.825	44.434	44.186	42.611	46.582
β_{xxy}	-6.319	-9.409	-13.773	-12.826	-12.192
β_{xxz}	-6.590	-7.031	-6.836	-6.381	-6.404
β_{yyy}	6.333	9.414	13.834	12.901	12.256
β_{yyz}	-6.587	-7.034	-6.833	-6.355	-6.404
β_{zzz}	-35.304	-20.492	6.941	14.551	11.348
μ (in D)	0.974	0.985	0.914	0.899	1.022
$\bar{\alpha}$	51.651	57.777	57.320	55.041	60.153
β_{\parallel}	-29.089	-20.234	-4.037	1.089	-0.876

Table 4.6: CHCl_3 permanent dipole moment, linear polarizabilities, and the first hyperpolarizabilities results with SIESTA. Study of convergence by varying energy shift $\delta\epsilon$ value. The DZP basis set and energy shift of 0.01 Har are the SIESTA default settings. The 5Z4P basis set is the same basis as used in Table 4.5.

	DZP	5Z4P	5Z4P	5Z4P	5Z4P	5Z4P
Energy Shift (Har)	0.01	0.5×10^{-4}	0.5×10^{-5}	0.5×10^{-6}	0.5×10^{-7}	10^{-8}
Cut-off radius (Bohr)						
$r_c^s(\text{C})$	4.088	6.911	8.030	9.330	10.572	11.114
$r_c^p(\text{C})$	4.870	9.330	11.114	12.913	14.632	15.772
$r_c^s(\text{H})$	4.709	8.800	10.483	12.180	13.802	14.877
$r_c^s(\text{Cl})$	3.826	6.152	7.148	8.099	8.951	9.410
$r_c^p(\text{Cl})$	4.673	8.099	9.410	10.993	12.389	13.024
μ_z	0.262	0.406	0.404	0.403	0.402	0.402
α_{xx}	50.718	66.953	67.204	67.080	66.937	66.887
α_{yy}	51.147	67.167	67.316	67.113	66.939	66.857
α_{zz}	31.313	46.413	46.650	46.628	46.582	46.538
β_{xxy}	-7.618	-9.440	-11.674	-12.238	-12.192	-12.181
β_{xxz}	-2.832	-4.970	-6.232	-6.443	-6.404	-6.398
β_{yyy}	7.202	9.518	11.799	12.329	12.256	12.223
β_{yyz}	-2.908	-4.996	-6.252	-6.451	-6.404	-6.382
β_{zzz}	-16.395	3.979	9.387	11.090	11.348	11.278
μ (in D)	0.666	1.031	1.026	1.024	1.022	1.021
$\bar{\alpha}$	44.393	60.178	60.390	60.273	60.153	60.094
$\beta_{ }$	-13.281	-3.592	-1.858	-1.083	-0.876	-0.901

0.0015) for $2s$ orbital of C and Cl, and $1s$ orbital of H. The default value is 0.15 and usually yields very good value. Indeed, the DZDP basis set using the splitnorm set to 0.15 gives the value of μ and α closest to that of the large basis 5Z4P set. However, the problem is that the first hyperpolarizability β values, especially β_{zzz} , is too *negative* whereas 5Z4P basis result is *positive*. If we choose small splitnorm value (split from the first- ζ at near the tail), the values of β become close to the 5Z4P basis.

The value obtained by the 5Z4P basis is very similar to the Gaussian03 [91] PBE/PBE aug-cc-pVQZ basis set results of Davidson *et al.* [90]. We have also tested SIESTA basis set result against the other available methods in Gaussian.¹ The results are summarized in Table 4.7. The HyPol basis set is the basis set specifically designed for the calculation of non-linear properties by Pluta and Sadlej [92]. We have also studied the role of electron correlation in the accuracy of the calculation. For this we used PBE, B3LYP hybrid functionals for DFT as well as *ab initio* methods like HF, MP2 and CCSD.

All the DFT methods predict a negative value for $\beta_{||}$; the results are, however, within the experimental error margin. The *ab initio* methods produce positive values, again within the experimental margin of error.

Table 4.8 shows the result of frequency calculation of CHCl_3 . Both vector average $\beta_{||}$ and rotational average β_{HRS} (Eq. 4.4) are listed for comparison with experimental results to be discussed later.

¹Gaussian calculation is performed by Fernando D. Vila at the University of Washington.

Table 4.7: CHCl_3 permanent dipole moment, linear polarizabilities, and the first hyperpolarizabilities results with SIESTA, and compares against various methods with GAUSSIAN 03.

	This Work	PBE	B3LYP	HF	MP2	CCSD	Expt.
	5Z4P	HyPol	HyPol	HyPol	HyPol	HyPol	
μ_z	0.402	0.407	0.425	0.477	0.425	0.426	
α_{xx}	66.937	66.787	64.865	60.265	63.311	62.777	
α_{yy}	66.939	66.797	64.869	60.266	63.312	62.778	
α_{zz}	46.582	46.830	45.825	42.981	45.420	45.129	
β_{xxy}	-12.192	-14.012	-10.870	-6.604	-6.863	-7.703	
β_{xxz}	-6.404	-6.739	-5.582	-3.216	-4.016	-4.333	
β_{yyy}	12.256	14.242	10.953	6.606	6.877	7.719	
β_{yyz}	-6.404	-6.747	-5.593	-3.216	-4.016	-4.333	
β_{zzz}	11.348	12.161	10.039	6.782	8.639	8.830	
μ (in D)	1.022	1.034	1.080	1.213	1.080	1.084	1.04 ± 0.02^a
$\bar{\alpha}$	60.153	60.138	58.520	54.504	57.348	56.895	
$\beta_{ }$	-0.876	-0.795	-0.682	0.210	0.364	0.0985	0.5 ± 2^b

^a Experiment from Ref. [93].

^b Gas phase EFISH measurement from Ref. [71].

Table 4.8: Frequency-dependent hyperpolarizability averages β_{\parallel} and β_{HRS} for the CHCl_3 molecule. The first hyperpolarizability in physical unit is given by β 1 a.u. = $3.20636 \times 10^{-53} \text{C}^3 \text{m}^3 \text{J}^{-2} = 8.6392 \times 10^{-33} \text{esu}$.

	$\omega = 0.0 \text{ eV}$	$\omega = 0.65 \text{ eV}$	$\omega = 1.17 \text{ eV}$	$\omega = 1.24 \text{ eV}$
$\beta(0; -\omega, \omega)$				
$\beta_{\parallel} \text{ (a.u.)}$	-0.813	-1.037	-1.081	-1.090
$\beta_{\text{HRS}} \text{ (a.u.)}$	9.594	9.726	10.001	10.005
$\beta_{\text{HRS}} (10^{-30} \text{ esu})$	0.0829	0.0841	0.864	0.0868
$\beta(-2\omega; \omega, \omega)$				
$\beta_{\parallel} \text{ (a.u.)}$	-0.813	-1.269	-1.729	-1.829
$\beta_{\text{HRS}} \text{ (a.u.)}$	9.594	10.021	10.945	11.131
$\beta_{\text{HRS}} (10^{-30} \text{ esu})$	0.0829	0.0866	0.0946	0.0962
$\beta_{\text{HRS}} \text{ Expt. (a.u.)}$	8.55 ± 0.6^a			

^a Experimental result of HRS, sum of $\langle \beta_{\text{VV}}^2 \rangle^{1/2}$ and $\langle \beta_{\text{HV}}^2 \rangle^{1/2}$ polarization average, from Ref. [94].

4.6 *para*-Nitroaniline (pNA)

The pNA molecule has an electron donor amino-group and an electron acceptor nitro-group (Fig. 4.20). It is also known to have a large hyperpolarizability β because of the intra-molecular donor-acceptor charge-transfer contribution [95]. This is one of the smallest examples of the “push-pull” molecule where the donor group “push” charges and the acceptor aids to “pull” charges to enhance the nonlinear optical activities.

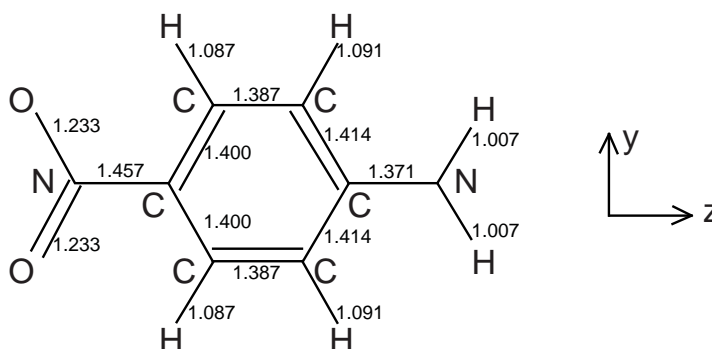


Figure 4.20: The molecular structure of *p*-Nitroaniline (pNA). The bond lengths are shown in Å.

The molecule pNA has been particularly useful for testing theoretical calculations, since accurate experimental [96, 97, 71, 98] and theoretical [99, 100, 101, 68, 13, 14, 102, 58, 90, 1] results are widely available. In addition, this molecule is an important prototype molecule for the large scale “push-pull” molecule for building organic nonlinear molecules of chromophores appearing in the next chapter for device applications.

Fig. 4.21 and Fig. 4.22 show the dynamical polarizability $\alpha(\omega)$ pNA using a step function as an external field. This result includes 0.3 eV broadening. The first absorption peak is located at 3.49 eV, which corresponds to $\lambda_{\max} = 356$ nm. This is in good agreement with the observed peak for pNA in chloroform solution of 347 nm [97] as it typically exhibits solvatochromic red shift.

In order to check internal consistency and completeness, we have calculated the effective

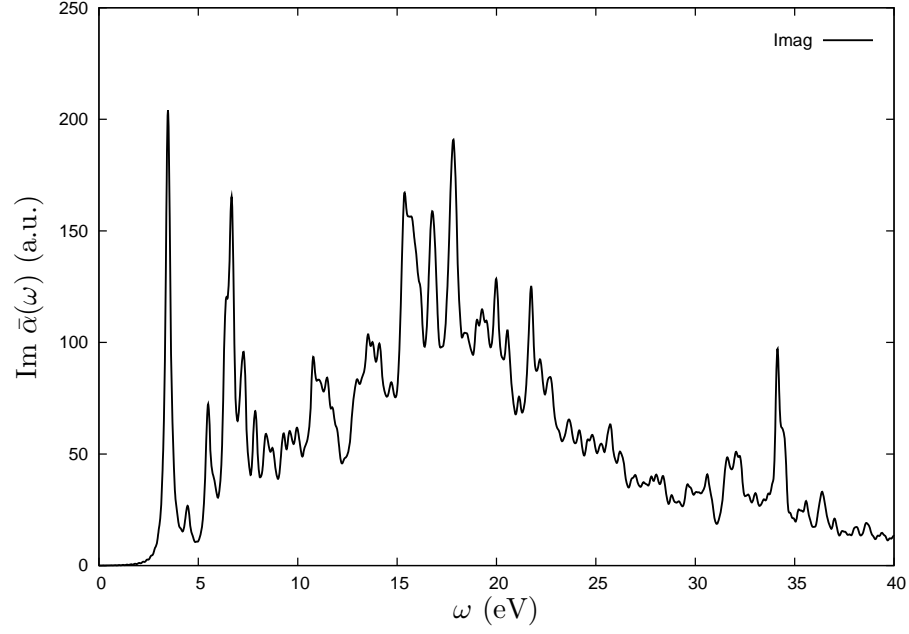


Figure 4.21: The imaginary part of dynamical polarizability $\text{Im } \alpha(\omega)$ of pNA obtained from the response to the step function external field.

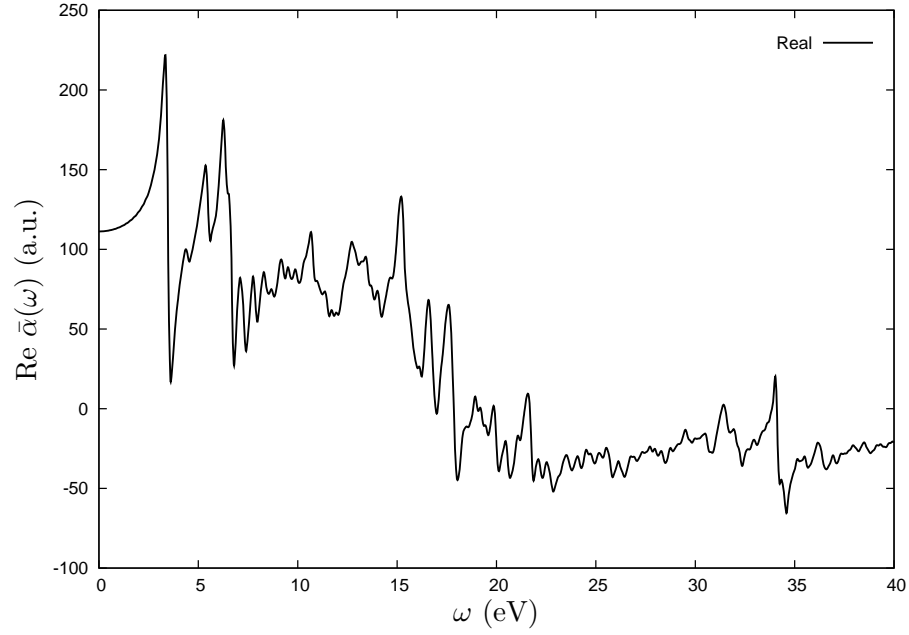


Figure 4.22: The real part of dynamical polarizability $\text{Re } \alpha(\omega)$ of pNA, obtained from the response to the step function external field.

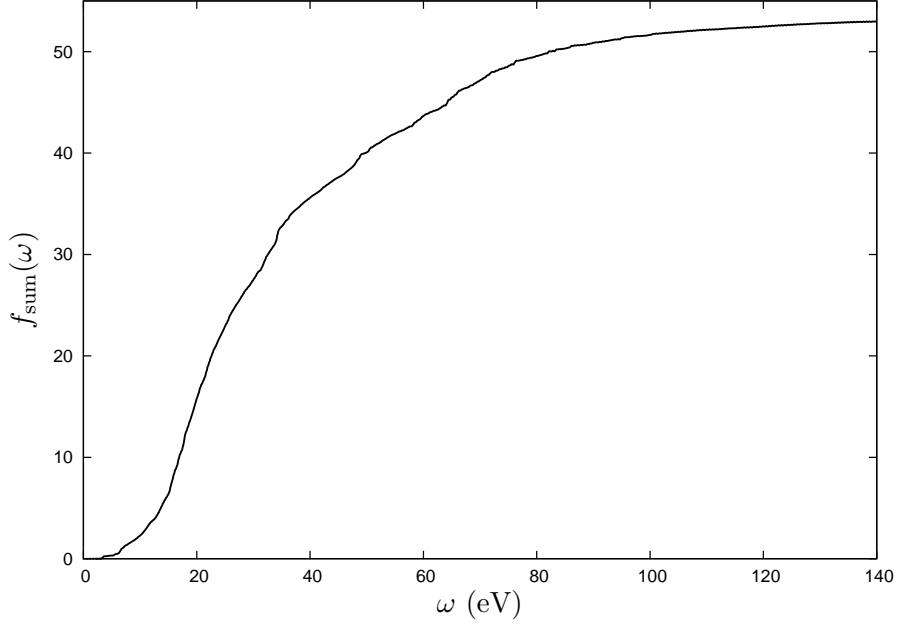


Figure 4.23: f -sum rule for pNA (see text). The exact limit is $N_e = 52$.

number of electrons contributing to the absorption N_e using the f -sum rule,

$$\int_0^\infty d\omega S(\omega) = \lim_{\omega \rightarrow \infty} f_{\text{sum}}(\omega) = \sum_i f_i = N_e, \quad (4.6)$$

where $f_{\text{sum}}(\omega) \equiv \int_0^\omega d\omega' S(\omega')$, and f_i are the oscillator strengths. The result for the partial sums $f_{\text{sum}}(\omega)$ is illustrated in Fig. 4.23. This yields $N_e = 51.8$ for large ω , whereas the actual number of valence electrons for pNA is $N_e = 52$. The small difference is likely due to numerical error.

We have used both the 5Z4P and DZDP basis sets for the calculation of dynamic hyperpolarizabilities. Note that unlike previously studied small molecules, small basis size would not cause a much of a problem especially for a molecule with a large permanent dipole moment. The reason is that even though the basis size per atom is small, the total number of basis orbitals for a molecule is big, so that there is enough flexibility in the atomic basis sets to represent the molecular states. For example, there are 228 basis orbitals in the DZDP basis in pNA compared to 80 and 165 basis orbitals in the DZDP and 5Z4P basis in CHCl_3 respectively; hence, the number of basis orbitals in a molecule is larger for the DZDP basis set in pNA than that of the 5Z4P basis set in CHCl_3 .

The results of the frequency-dependent calculation of hyperpolarizability are shown in Table 4.9 and Fig. 4.24. The figures include the results for the DZDP basis as well as the 5Z4P basis. The 5Z4P basis calculation is consistently higher than DZDP basis calculation, a difference of about 7% throughout. For comparison with the other theoretical calculations, HF results are, again, much smaller than the observed values. The difference is clearly due to the absence of correlation in HF. The TDDFT B3LYP study is a calculation of the response functions at the DFT level based on an exponential, second-quantized parametrization of the density operator [14]. The same group has applied the method with higher-order wave function method using CCSD in the later study [3]. Both method yields results significantly lower than our calculations, especially at higher frequencies close to the resonance. Lastly, our results agree well with recent real-grid, frequency-space calculations for pNA by Andrade *et al.* [1]. Their result is almost identical to our DZDP basis calculation. Our method agrees well the location of the second harmonic generation resonant frequency shown in Fig. 4.25. Close to resonance space our results are higher than those in Ref. [1], but this is likely due to differences in damping factors. Our calculation of the static value $\beta(0;0,0)$ is obtained from the classic FFPT method, without any time-integration. However, our RT-TDDFT frequency-dependent calculation also converges to the correct static limit.

For the comparison with experimental results, our 5Z4P basis calculation seems to outperform the other available theoretical methods. However, there remain many uncertainties in the experimental measurement. For example, the EFISH experimental results are obtained by pNA in a solution extrapolated to infinite dilution of the solvent [99], in which the

Table 4.9: Frequency-dependent hyperpolarizability $\beta_{||}(-2\omega, \omega, \omega)$ of pNA in the atomic unit, using the B-convention.

ω (eV)	Real-time	HF ^a	MP2 ^b	TDDFT ^c	CCSD ^d	Expt. ^e	Expt. ^f
	5Z4P		B3LYP				
0.507	303		476	521			
0.65	624	314		566	572	670 ± 35	
0.905	775	324				820 ± 21	
1.17	1083	339	833	899	800	1170 ± 28	1072 ± 44
1.364	1720	354		1209	960	1740 ± 69	
1.494	2739	365		1604	1120	2780 ± 210	

^a Ref. [71].

^b Ref. [68] using RPA dispersion.

^c Ref. [14].

^d Ref. [3].

^e Ref. [99], extrapolated from solvent measurements.

^f Ref. [71], gas phase measurement.

limit may not be equal to pure pNA measurement. More promising is the agreement with the gas phase EFISH measurement at 1.17 eV by Kaatz *et al.* [71]. Indeed, Salek *et al.* argue that their divergent results with solvent measurements may arise from a probable red shift of the lowest transition in solution that alters the slope of the dispersion curve and explain the discrepancy between the B3LYP DFT and CCSD models as well as experimental results [3]. They believe B3LYP overestimates hyperpolarizability rather than underestimating at high frequencies. We would rather not conclude our results are “better” than those of their method, but we believe they may have a problem with basis set, as we found that increasing basis size made the values increase.

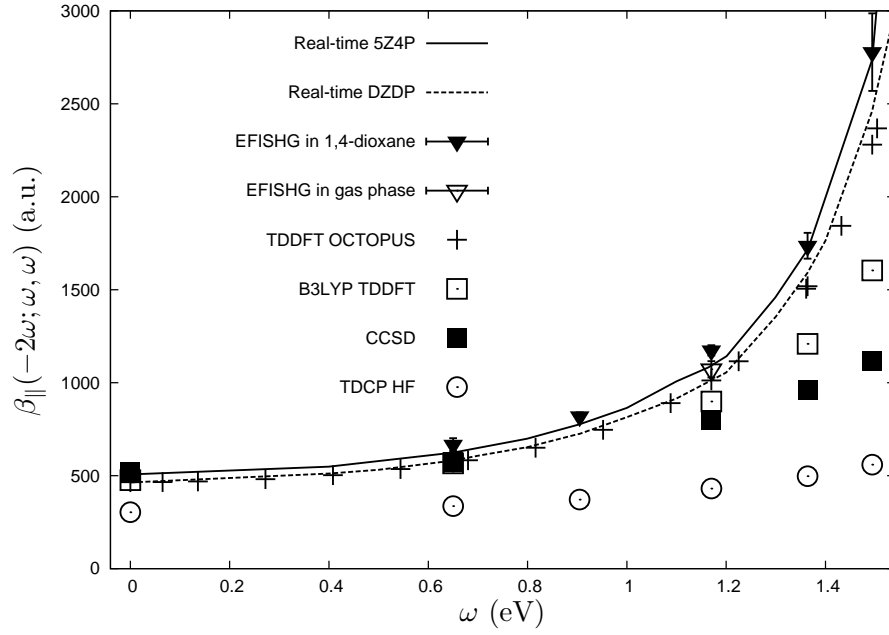


Figure 4.24: Frequency-dependent of the first hyperpolarizability $\beta_{\parallel}(-2\omega; \omega, \omega)$ for pNA, using the B-convention. References are given in Table 4.9, except for OCTOPUS [1].

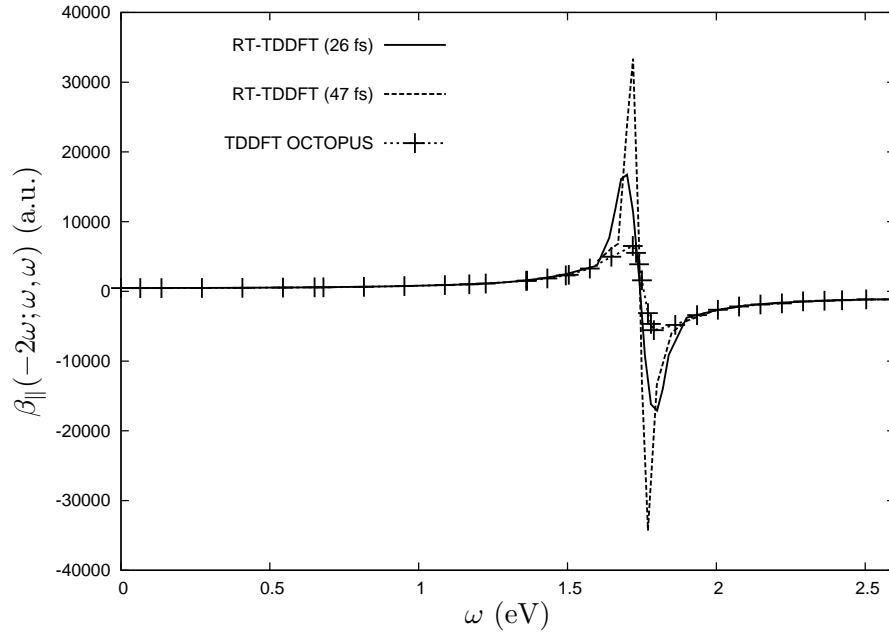


Figure 4.25: The first hyperpolarizability $\beta_{\parallel}(-2\omega; \omega, \omega)$ of pNA including the lowest resonant frequency, and compared against results of Ref. [1], using the B-convention. The results of two different simulation times are shown (26 and 46 fs) near the resonant frequency.

4.7 Time-evolution Time Step Dependence on a System.

For a given total simulation time T , there is a maximum simulation time step that can be used for calculating a given system. The size of the time step is usually much smaller than the theoretically required Nyquist–Shannon sampling theorem of the time step for obtaining the response at a given frequency. For example, for the frequency at $\omega = 27.2$ eV or 1 Har frequency, the required time step is $\pi/\omega = 3.14$ Har $^{-1}$. The typical optical frequency of 1 eV or less would only require the time step of order 10 Har $^{-1}$. However, as shown in Table. 4.10, it would require one to use a much smaller time step due to the fact that the time-evolution simulation begins to diverges within the duration of simulation as illustrated in Fig. 4.26. In general, the smaller and lighter molecule requires the use of the smaller time step. It is also depends on the basis set, it is usually possible to use the larger time step for a given simulation time T with the larger basis set comparing to the smaller basis set. We found that the 5Z4P basis enables us to choose the time step Δt by a factor of about 2 larger than the DZDP basis. Due to this advantage of using larger time step, 5Z4P basis set actually takes less time than the DZDP basis set, especially for a small molecule. This is quite important for setting up a simulation as increasing basis size does not necessary increase the calculation cost.

Table 4.10: The maximum time step (Har $^{-1}$) for nonlinear calculation running for the total simulation time $T = 860$ Har $^{-1}$ or $T \sim 20$ fs. The elapsed time is also shown in 10^3 sec running on Intel(R) Xeon(R) CPU E5335 @ 2.00GHz.

	CO	H ₂ O	CHCl ₃	pNA
Basis Size				
DZDP	0.06	0.08	0.22	0.24
5Z4P	0.10	0.10	0.50	0.54
Elapsed Time (10^3 sec)				
DZDP	19	15	9	30
5Z4P	14	14	5	28

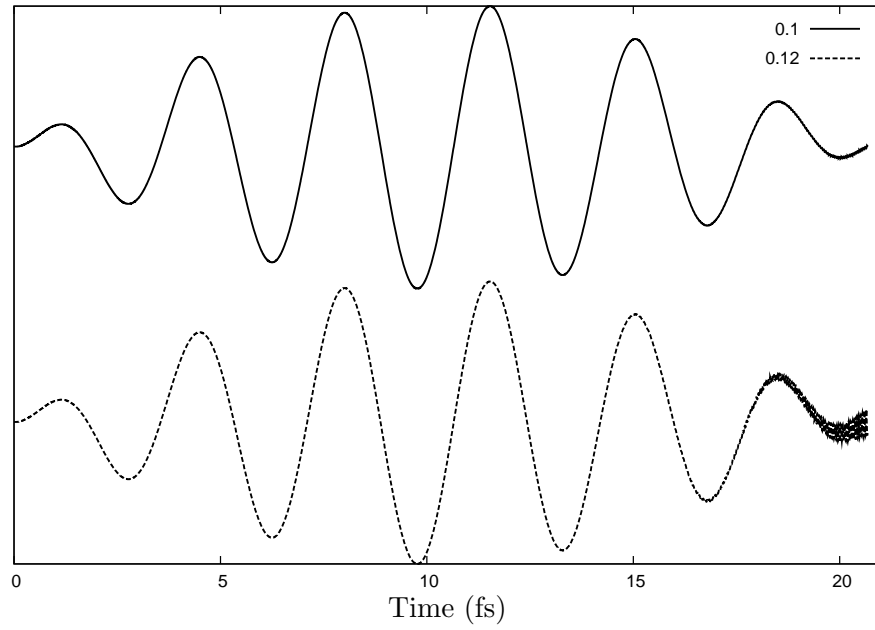


Figure 4.26: The real-time simulation of the dipole moment p_z of CO with quasimonochromatic frequency of $\omega = 1.17$ eV in E_z direction. The top curve is obtained with $\Delta t = 0.1$ Har $^{-1}$ and the bottom curve is obtained with $\Delta t = 0.12$ Har $^{-1}$.

Chapter 5

APPLICATION FOR LARGE PHOTONIC MOLECULES

5.1 YLD156 Chromophore Linear and Non-linear Polarizability

Increasingly large molecular hyperpolarizabilities have long been predicted, specifically, larger π -conjugation organic chromophores [103, 104, 105, 106, 107]. The π -electron conjugated core of chromophore analogous to YLD156 is used to build the tri-chromophore containing dendrimer PSLD33 studied in Dalton’s group at the University of Washington chemistry department. Relevant synthesis and characterization is covered in Ref. [108, 109, 110]. This chromophore is particularly interesting for making large electro-optic coefficients in electric field-poled organic materials. The structure of the molecule YL156 [2-(3-cyano-4-((E)-2-(5-(4-(dimethylamino)-styryl)thiophen-2-yl)vinyl)-5-phenyl-5-(trifluoromethyl)furan-2(5H)-ylidene) malononitrile] is shown in Fig. 5.1. The molecular geometry was optimized with the DFT code DMol3 using the PBE functional and DNP numerical basis set.¹ The medium optimization criteria were satisfied with the energy converged to 1.4×10^{-5} Har, the maximum gradient to 12.3×10^{-4} Har/bohr, and the maximum displacement to 0.085 bohr. This structure was used for all subsequent calculations.²

Fig. 5.2 shows UV/Vis absorption spectra calculated both with the real-time method and experimental measurement in chloroform solution. This real-time calculation is performed with the DZDP basis set and mesh cut-off value 60 Har. The resulting spectra of calculation is obtained by including third-order polynomial damping (Eq. B.4). The observed lowest absorption peak is located at $\omega_0 = 1.65$ eV ($\lambda_0 = 753\text{nm}$) in chloroform solution. Our real-time result of gas phase calculation gives $\omega_0 = 1.72$ eV ($\lambda_0 = 721\text{nm}$). The difference is likely due to solveto-chromic shift that includes the effect of solvent molecules distorting the charge-transfer molecular orbital state as well as local field correction; both affect the

¹Materials Studio and DMol3; Accelrys: San Diego, 2002.

²Optimization is provided by Bruce E. Eichinger eichinger@chem.washington.edu.

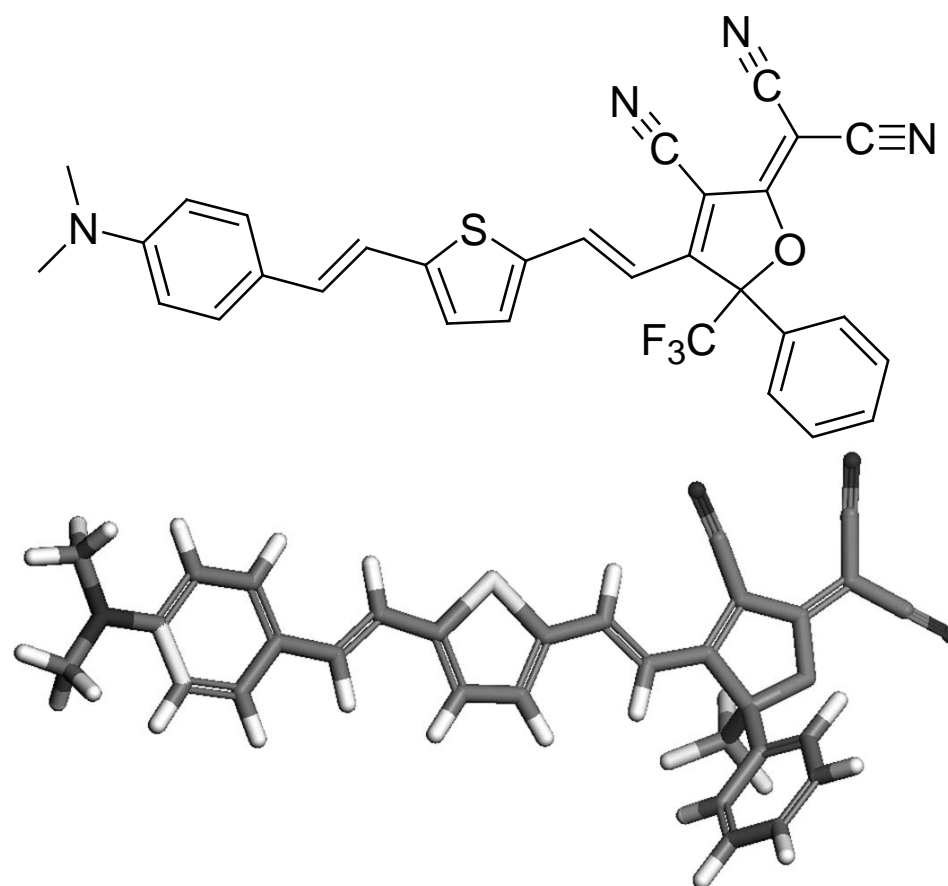


Figure 5.1: The molecular structure of YLD156 nonlinear chromophore.

bond length of the solute molecule and linear absorption. The solvent considerations are important for comparison to the experiments.

The TDDFT linear calculation of the isolated molecule already yields a reasonable value of the first absorption peak. Moreover, the absolute error of ~ 0.1 eV is in the error range of TDDFT. Table 5.1 shows static properties of the YLD156 chromophore, comparing calculations with the DZDP and 5Z4P basis sets. As we see, the difference between the two basis sets is about 1-3% for all values including nonlinear properties. We, therefore, confirmed that the large system does not necessary to use the large basis set as in the small molecules. The reason is, again, that the total number of atomic basis orbitals with the DZDP basis set is much larger than that of the smaller molecule we have studied with the 5Z4P basis set; hence the basis orbitals tends to completes the molecular states even with relatively small basis sets per atomic site.

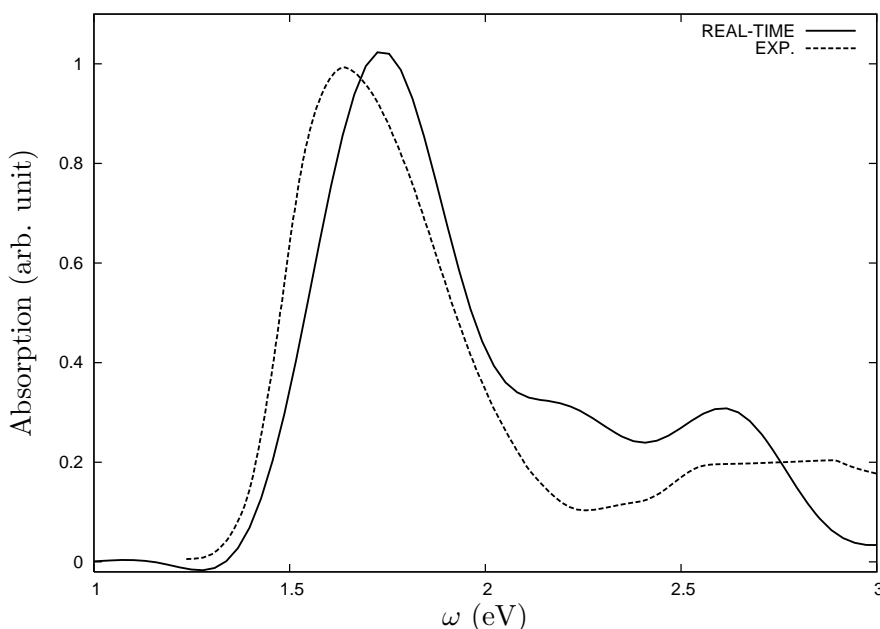


Figure 5.2: UV/Vis. photoabsorption spectrum for YLD156. Experiment is measured in chloroform solution.

Table 5.2 shows the first hyperpolarizability β frequency calculation for the YLD156 chromophore. Theoretical comparison with DALTON [111, 112, 101] and GAUSSIAN03

Table 5.1: YLD156 permanent dipole moment, linear polarizabilities, and the first hyperpolarizabilities of static ($\omega = 0$) results with SIESTA (β 1 a.u. = 8.6392×10^{-33} esu).

	DZDP	5Z4P
μ_z	9.948	10.19
α_{xx}	539	543
α_{yy}	281	283
α_{zz}	1736	1768
μ (in D)	25.28	25.90
$\bar{\alpha}$	852	865
β_{zzz} (10^{-30} esu)	307	317
β_{\parallel} (10^{-30} esu)	203	210
β_{HRS} (10^{-30} esu)	151	156

calculations are also included. The DALTON calculation is already too expensive to perform with the sufficiently large basis sets for this molecule. We have used B3LYP/3-21g basis sets as opposed to the standard 6-31g basis sets. All calculation agrees within an order of magnitude at the static value, where HF value seems underestimate, as we already have found in the small molecule. Calculations start to diverge at higher frequencies. Our real-time method seems to yield the best agreement with the experimental value, as we discuss in the following section.

There is no direct experimental information on $\beta_{zzz}(0; -\omega, \omega)$. However, the nonlinear characteristics of the chromophore are commonly evaluated using hyper-Rayleigh scattering (HRS), which measures $\beta_{\text{HRS}}^2(-2\omega, \omega, \omega)$. HRS measures a signal $S_{2\omega} \propto I_{2\omega}$ where $I_{2\omega}$ is the intensity of the scattered light at 2ω . For a two-component system (solute and solvent), one can write [113]

$$S_{2\omega} = G [N_{\text{solvent}} \langle \beta_{\text{HRS}}^2 \rangle_{\text{solvent}} + N_{\text{solute}} \langle \beta_{\text{HRS}}^2 \rangle_{\text{solute}}] I_{\omega}^2, \quad (5.1)$$

where the constant G accounts for instrument factors, orientation average, and other constants. When measurement is performed in a dilute solution, the refractive indices and the

Table 5.2: Frequency dependence of the nonlinear coefficients $\beta(0; -\omega, \omega)$ and $\beta(-2\omega; \omega, \omega)$ of YLD156 (β 1 a.u. = 8.6392×10^{-33} esu).

	$\omega = 0.0$ eV	$\omega = 0.65$ eV	$\omega = 0.8$ eV	$\omega = 1.24$ eV
$\beta_{zzz}(0; -\omega, \omega)$ (10^{-30} esu)				
Real-time	307	414	532	1383
DALTON ^{a*}	340	421	482	867
HF ^{b*}	208	234	249	269
$\beta_{\text{HRS}}(0; -\omega, \omega)$ (10^{-30} esu)				
Real-time	151	205	262	686
DALTON ^{a*}	165	203	233	414
HF ^{b*}	103	116	123	134
$\beta_{zzz}(-2\omega; \omega, \omega)$ (10^{-30} esu)				
Real-time	307	924	4218	2062
DALTON ^{a*}	340	719	1287	-2719
$\beta_{\text{HRS}}(-2\omega; \omega, \omega)$ (10^{-30} esu)				
Real-time	151	446	1999	980
DALTON ^{a*}	165	347	621	1292

^a DALTON calculation with B3LYP/3-21g* basis.

^b Gaussian03/HF calculation with 6-31g* basis.

* Both DALTON and HF calculation are performed by B. Eichinger at University of Washington.

solvent number density $N_{solvent}$ do not change significantly with solute density. Then, the signal $S_{2\omega}$ as a function of $N_{solvent}$ yields a straight line, hence the ratio $\langle\beta_{HRS}^2\rangle_{solute}/\langle\beta_{HRS}^2\rangle_{solvent}$ can be obtained. Hence, it measures the “relative” value β_{HRS}^{Rel} in which gives the ratio of $\beta_{solute}/\beta_{solvent}$. Table 5.3 shows both theoretical and the experimental values of the ratio. The value at higher energy slightly overestimates the experimental value, but is generally in satisfactory agreement given estimated experimental error. Note that if we took DALTON results to estimate the quantity, the value at 0.65 eV would be too small and 1.24 eV would be too big compared to the real-time results.

Table 5.3: Comparison of theoretical and HRS experimental values for YLD156. All β values are in 10^{-30} esu (β 1 a.u. = 8.6392×10^{-33} esu).

	$\beta_{HRS}(-2\omega)$ YLD156	$\beta_{HRS}(-2\omega)$ $CHCl_3$	β_{HRS}^{Rel} (This work) $\beta_{solute}/\beta_{CHCl_3}$	β_{HRS}^{Rel} (Expt. ^a) $\beta_{solute}/\beta_{CHCl_3}$
0.65 eV ($\lambda = 1.9\mu m$)	446	0.0866	5150	6100 ± 2000
1.24 eV ($\lambda = 1.0\mu m$)	980	0.0962	10190	7940 ± 500

^a The experimental value was measured by HRS relative to $CHCl_3$ as the internal standard.

Fig. 5.3 and Fig. 5.4 show the frequency spectra of YL156 for the first hyperpolarizability values, $\beta_{zzz}(-2\omega; \omega, \omega)$ and $\beta_{HRS}(-2\omega; \omega, \omega)$, respectively. Fig. 5.5 shows the frequency spectra of $\beta_{zzz}(0; -\omega, \omega)$ and $\beta_{HRS}(0; -\omega, \omega)$ related to the OR. For the calculation of the OR, there we can see the unphysical glitch at the lowest resonant frequency of the SHG $\beta(-2\omega; \omega, \omega)$, which cannot completely removed by the damping technique described earlier. We, however, believe it can be removed if we use a sufficiently longer simulation.

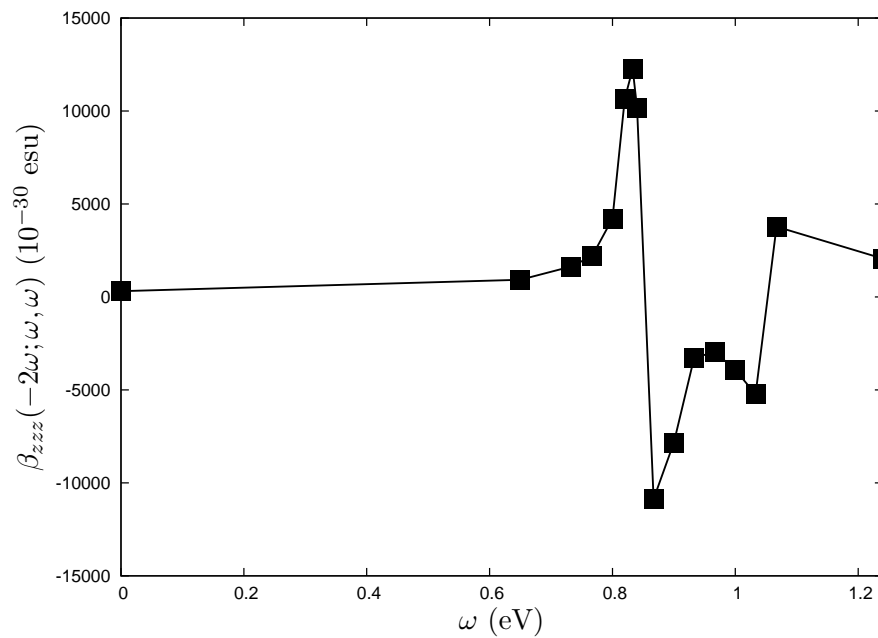


Figure 5.3: The first hyperpolarizability spectrum of $\beta_{zzz}(-2\omega; \omega, \omega)$ for YLD156.

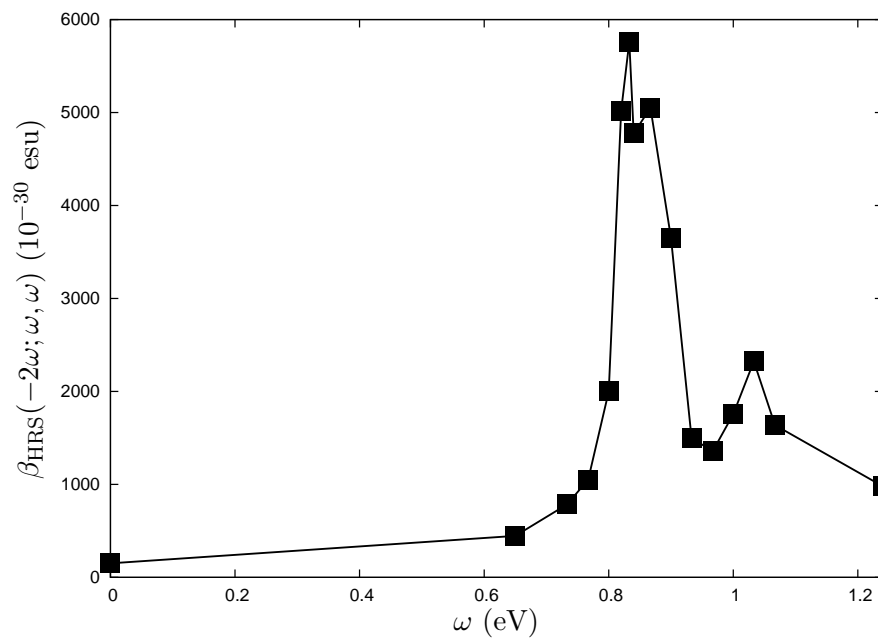


Figure 5.4: The first hyperpolarizability spectrum of $\beta_{\text{HRS}}(-2\omega; \omega, \omega)$ for YLD156.

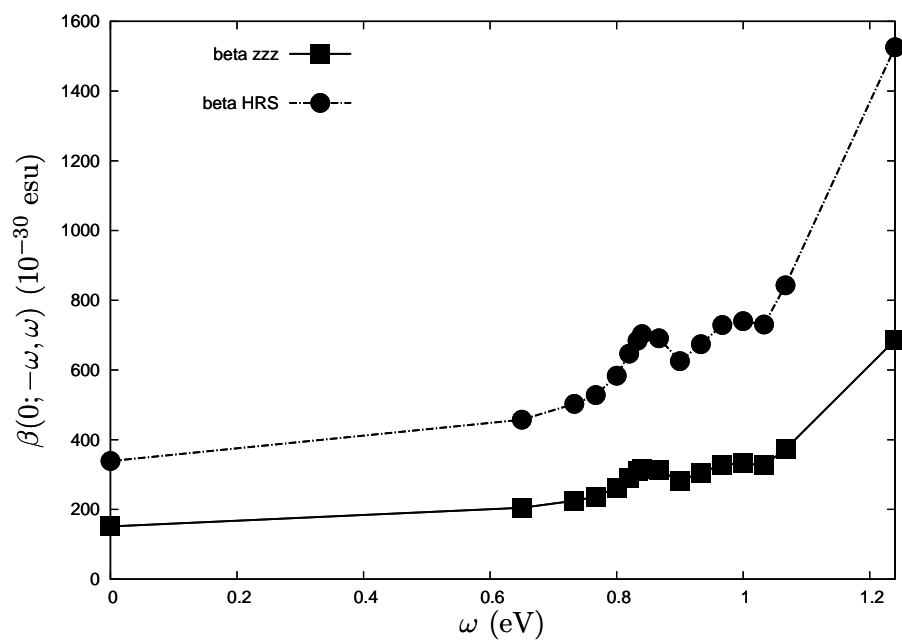


Figure 5.5: The first hyperpolarizability spectrum of $\beta_{zzz}(0; -\omega, \omega)$ and $\beta_{HRS}(0; -\omega, \omega)$ for YLD156.

Chapter 6

STUDY OF “LOCAL” SOLVENT EFFECTS IN OPTICAL LINEAR AND NONLINEAR RESPONSE

It is important to consider the effect of solvents on optical properties of molecules as the result of the molecular interaction with the solvent environment. In the classic study by Debye and Onsager [114, 115], a polarizable dielectric medium induces a reaction field on a molecule with dipole moment that tends to enhance the internal dipole moment. A more precise description of the dielectric effect is usually studied via the polarizable continuum model (PCM) of Tomasi *et al.* [116], where reaction energies are calculated using a cavity defined through van der Waals-spheres centered at atomic positions and the reaction field is represented through point charges located on the surface of the molecular cavity.

Our preliminary study of the solvent effect on optical properties attempts to address the “local” solvent effect, or the local reaction field, rather than the dielectric reaction field. More precisely, we will address the effect of “hydrogen bonds” on a dipole molecule and study the changes in the dynamic linear and nonlinear properties.

Here we have studied pNA with presence of methanol (CH_3OH) and chloroform (CHCl_3). Fig. 6.1, Fig. 6.2, and Fig. 6.3 show our model of pNA molecule in local contact with methanol. All structures are optimized with ground-state DFT using B3LYP 6-31+G(d,p) basis sets. The hydrogen bonds distance given by the hybrid functional of B3LYP is usually sufficient for purpose of this study whereas the LDA functional is known to predict poorly for the distance between two molecules. Fig. 6.1 is the interaction of methanol through the acceptor side of the nitro group. Fig. 6.2 is the interaction of methanol through the donor side of the amino group. Fig. 6.3 is the interaction of two methanol molecules both on the acceptor and donor side of pNA. Similarly, Fig. 6.4, Fig. 6.5, and Fig. 6.6 represent our model of the pNA molecule in local contact with chloroform. Fig. 6.4 shows the interaction of chloroform through the acceptor side of the nitro group. Fig. 6.5 shows the interaction

of chloroform through the donor side of the amino group. Fig. 6.6 shows the interaction of chloroform through the phenyl group.

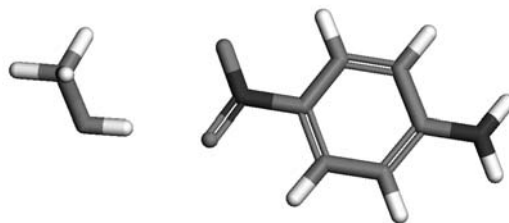


Figure 6.1: pNA+M(A), the molecular structure of pNA with CH₃OH. Interaction of methanol through the acceptor side of pNA.

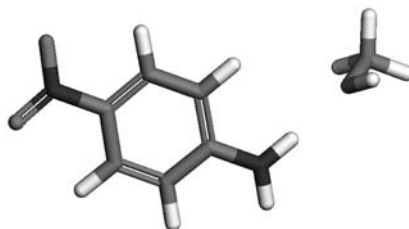


Figure 6.2: pNA+M(D), the molecular structure of pNA with CH₃OH. Interaction of methanol through the donor side of pNA.

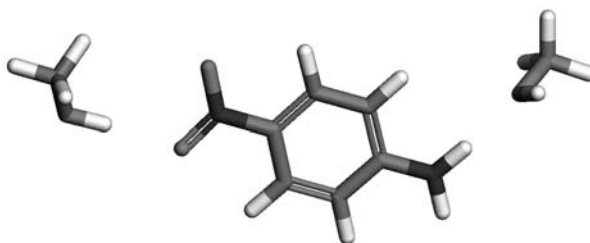


Figure 6.3: pNA+M(A,D), the molecular structure of pNA with CH₃OH. Interaction of methanol through the both acceptor and donor side of pNA.

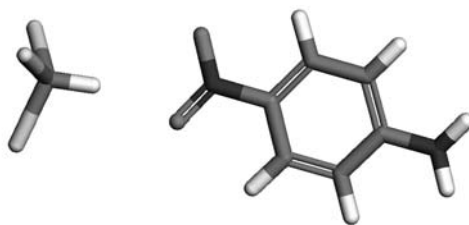


Figure 6.4: pNA+C(A), the molecular structure of pNA with CHCl₃. Interaction of chloroform through the acceptor side of pNA.

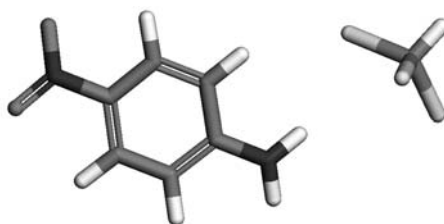


Figure 6.5: pNA+C(D), the molecular structure of pNA with CHCl₃. Interaction of chloroform through the donor side of pNA.

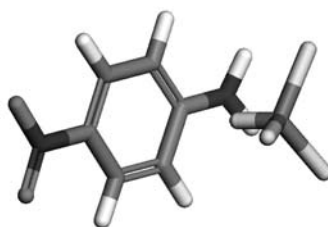


Figure 6.6: pNA+C(P), the molecular structure of pNA with CHCl₃. Interaction of chloroform through the the phenyl group of pNA.

Table 6.1 shows changes in the static properties of the model of Fig. 6.1, Fig. 6.2, and Fig. 6.3. as well as of the model of Fig. 6.4, Fig. 6.5, and Fig. 6.6. The values show both static properties of the whole system (pNA plus solvent) with z-axis defined to be the direction of dipole moment as well as the solvent molecule alone with the same geometry as the whole system but absent pNA (listed in parenthesis as a reminder that it is not the direction of the dipole moment of the solvent molecule). Due to the polar nature of the methanol molecule that changes the charge-transfer state of the pNA molecule so that the solvent enhances the dipole moment more than the sum of individual pNA and methanol molecules. On the other hand, the non-polar chloroform has very little effect except on the interaction through the acceptor side of pNA, otherwise known as the hydrogen bond effect. Similar trends can be seen with the linear polarizability. In the case of the first hyperporizability β , the changes in static values are very subtle; there does not seem to be any significant difference between the polar and non-polar molecules.

Fig. 6.7 and Fig. 6.8 show the linear absorption around the first absorption maximum. Table 6.2 summarizes the location of the maximum for each solvent model. It also gives experimental values in solution. The spectra of both methanol and chloroform were found to exhibit a red shift of about $6nm$ on the acceptor side of pNA, where both form the hydrogen bonds. On the contrary, methanol also makes 8-13nm red shift even in the donor side of pNA whereas almost no shift ($\pm 2nm$) with chloroform. The difference in the experimental absorption shift between methanol and chloroform is 9nm. If we assume the solvent molecule is equally likely on the acceptor side and the donor side, it appears that the result of the local solvent models is consistent with observed solvent shift.

Table 6.1: The static properties of “local” solvent CH_3OH or CHCl_3 near pNA. The values presented in parenthesis are the calculations of the solvent molecule alone but keeping the orientation the same as corresponding geometry with pNA.

	pNA	pNA+M(A)	M(A)	pNA+M(D)	M(D)	pNA+M(A,D)	M(A,D)
μ_z	3.09	3.89	(0.36)	4.04	(0.47)	5.11	(0.96)
α_{zz}	173.4	214.2	(22.1)	205.0	(21.3)	246.7	(43.2)
$\bar{\alpha}$	111.2	138.2	(22.3)	136.9	(22.2)	164.8	(44.5)
β_{zzz}	950.4	726.6	(3.39)	975.5	(-18.0)	791.9	(-17.7)
β_{\parallel}	506.7	394.2	(2.29)	543.5	(-15.7)	458.9	(-20.6)
β_{HRS}	377.0	108.7	(18.6)	412.2	(17.4)	365.9	(27.4)
	pNA	pNA+C(A)	C(A)	pNA+C(D)	C(D)	pNA+C(P)	C(P)
μ_z	3.09	4.02	(0.41)	3.39	(0.21)	2.69	(-0.16)
α_{zz}	173.4	247.2	(47.2)	246.1	(62.2)	225.0	(65.0)
$\bar{\alpha}$	111.2	177.6	(60.7)	174.3	(60.6)	168.1	(60.7)
β_{zzz}	950.4	1352	(9.84)	979.3	(-3.44)	866.9	(-6.32)
β_{\parallel}	506.7	755.1	(-1.55)	549.6	(-0.23)	464.0	(-1.13)
β_{HRS}	377.0	546.3	(9.53)	409.7	(7.74)	351.2	(5.58)

Table 6.2: The first absorption peak ω_{\max} and λ_{\max} of pNA with “local” solvent CH_3OH or CHCl_3 .

	ω_{\max} (eV)	λ_{\max} (nm)
pNA gas	3.48	356
pNA+M(A)	3.43	362
pNA+M(D)	3.41	364
pNA+M(A,D)	3.36	369
Expt. ^a (Methanol)		356
pNA+C(A)	3.43	362
pNA+C(D)	3.46	358
pNA+C(P)	3.49	355
Expt. ^a (Chloroform)		347

^a Expt. [97]

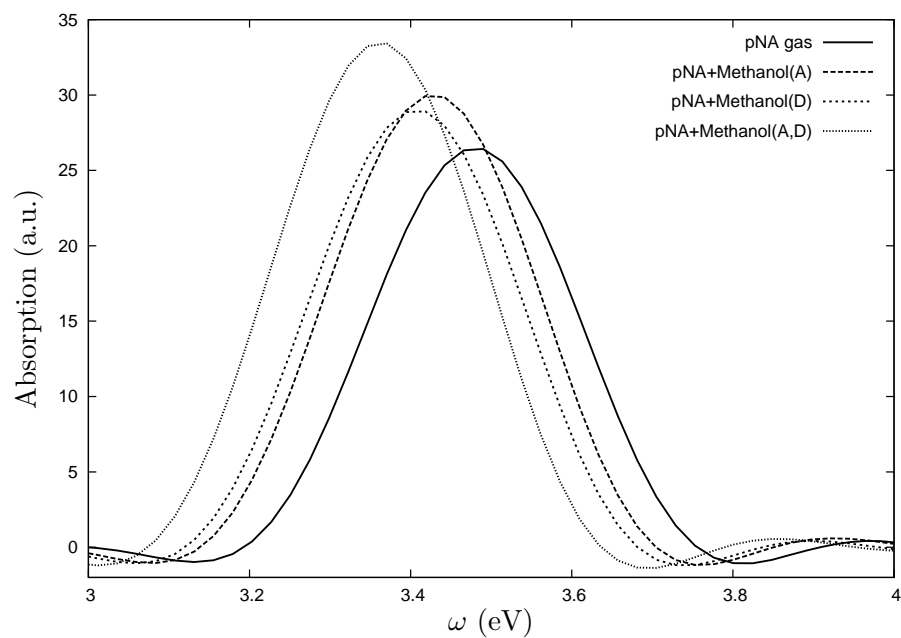


Figure 6.7: pNA plus local solvent - methanol - absorption spectra.

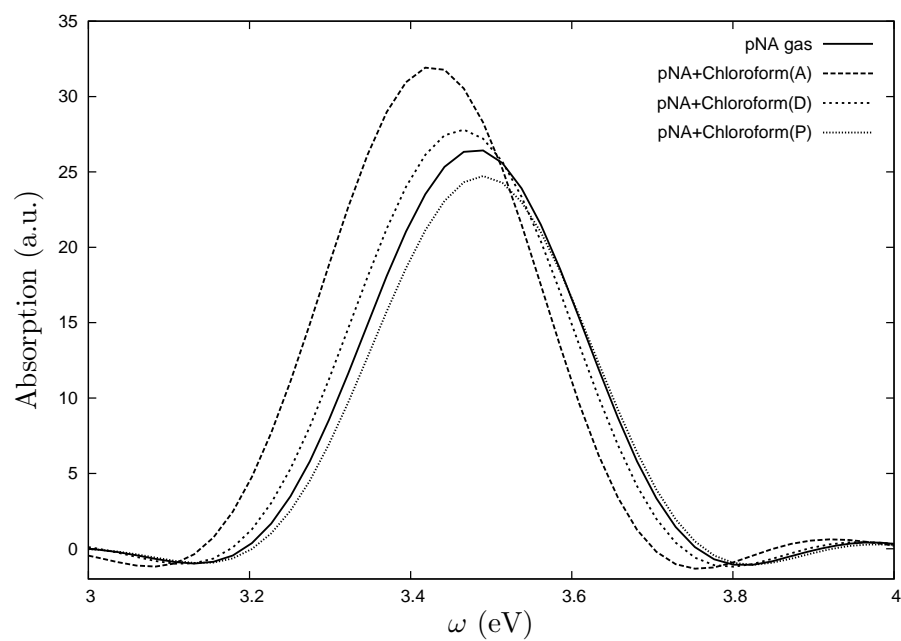


Figure 6.8: pNA plus local solvent - chloroform - absorption spectra.

Table 6.3 and Table 6.4 summarize the frequency-dependent calculation of pNA with local solvent at a typical laser frequency of $\omega = 1.17$ eV ($\lambda = 1064$ nm). It is now clear that the most prominent changes to the nonlinear properties are present when the solvent molecule interacts with the acceptor side of pNA. For the second harmonic generation (SHG), the spherical average of β_{HRS} increases by 95% for pNA with methanol (pNA + M(A) configuration), and 35% for pNA with chloroform (pNA + C(A) configuration). The factor of 2 enhancement observed with methanol is likely due to the strong hydrogen bonds formed between methanol and the acceptor side of pNA. Of course this is not a comprehensive study of the solvent effect, since we are only studying the local interaction with a few selected configurations. However, the effect on the frequency-dependent hydrogen bonds itself appears to be quite significant and consistent with the experimental measurements. The experimentally observed difference between the methanol and chloroform solutions is about a 33% enhancement in HRS signal. Our theoretical estimate of the difference is about 43% due to the hydrogen bonds.

Table 6.3: The first hyperpolarizability β at $\omega = 1.165$ eV with “local” solvent CH_3OH near pNA. The values presented in parenthesis are the calculations of the solvent molecule alone but keeping the orientation the same as corresponding geometry with pNA.

	pNA	pNA+M(A)	M(A)	pNA+M(D)	M(D)	pNA+M(A,D)	M(A,D)
$\beta(0, 0, 0)$ Static							
β_{zzz}	950.4	726.6	(3.39)	975.5	(-18.0)	791.9	(-17.7)
$\beta_{ }$	506.7	394.2	(2.29)	543.5	(-15.7)	458.9	(-20.6)
β_{HRS}	377.0	108.7	(18.6)	412.2	(17.4)	365.9	(27.4)
$\beta(0, -\omega, \omega)$ OR							
β_{zzz}	1177	222.1	(3.50)	1205	(-18.8)	597.4	(-18.5)
$\beta_{ }$	640.2	80.9	(2.27)	670.3	(-16.4)	328.7	(-21.6)
β_{HRS}	469.6	152.4	(19.4)	510.2	(18.1)	294.1	(28.6)
$\beta(-2\omega, \omega, \omega)$ SHG							
β_{zzz}	1973	3763	(3.75)	2051	(-20.7)	4051	(-20.5)
$\beta_{ }$	1083	2193	(2.54)	1169	(-18.0)	2469	(-23.6)
β_{HRS}	789.6	1556	(21.3)	869.3	(19.9)	1786	(31.4)
$\beta(-2\omega, \omega, \omega)$ HRS Expt. ^a in methanol 2590 ± 100							

^a Expt. [97], values are relative to *p*-dioxane HRS signal calibrated by its EFISH measurement.

Table 6.4: The first hyperpolarizability β at $\omega = 1.165$ eV with “local” solvent CHCl_3 near pNA. The values presented in parenthesis are the calculations of the solvent molecule alone but keeping the orientation the same as corresponding geometry with pNA.

	pNA	pNA+C(A)	C(A)	pNA+C(D)	C(D)	pNA+C(P)	C(P)
$\beta(0, 0, 0)$ Static							
β_{zzz}	950.4	1352	(9.84)	979.3	(-3.44)	866.9	(-6.32)
β_{\parallel}	506.7	755.1	(-1.55)	549.6	(-0.23)	464.0	(-1.13)
β_{HRS}	377.0	546.3	(9.53)	409.7	(7.74)	351.2	(5.58)
$\beta(0, -\omega, \omega)$ OR							
β_{zzz}	1177	1648	(10.3)	1196	(-3.46)	1080	(-6.49)
β_{\parallel}	640.2	926.8	(-1.56)	664.7	(0.14)	591.1	(-1.24)
β_{HRS}	469.6	667.5	(9.86)	502.1	(8.04)	440.1	(5.85)
$\beta(-2\omega, \omega, \omega)$ SHG							
β_{zzz}	1973	2665	(11.2)	1883	(-4.18)	1827	(-6.82)
β_{\parallel}	1083	1504	(-2.26)	1049	(-0.48)	1012	(-1.24)
β_{HRS}	789.6	1081	(10.8)	797.5	(8.79)	746.1	(6.36)
$\beta(-2\omega, \omega, \omega)$ HRS Expt. ^a in chloroform 1940 ± 60							

^a Expt. [97], values are relative to *p*-dioxane HRS signal calibrated by its EFISH measurement.

Chapter 7

FUTURE PROSPECTS AND CONCLUSION

We have presented a real-time approach for calculating the linear and nonlinear dynamic optical response of complex photonic molecules. The method has been extensively tested on small molecules, and with a sufficiently large basis set such that we were able to achieve accuracy comparable to the other available theoretical methods as well as available experimental results within their uncertainties. In fact, real-time method is often as good as more sophisticated state-of-art hybrid B3LYP functional when compared with conventional frequency-domain methods, even though our exchange-correlation only included gradient correction at the PBE level. One of the advantages of the real-time method is “automatic-inclusion” of the local field correlation effect by performing the time-evolution of the density. It is the crucial feature of the real-time density evolution used in TDDFT, as Hamiltonian is determined from the density of the system at the time and is implicitly related to the density of all previous states. In other words, real-time f_{xc}^{TDDFT} provides an effective electron-hole interaction efficiently, without much effort in the actual implementation, while it is known to give a significant contribution to the frequency spectra.

This method is a derivative of the TDDFT approach in which the evolution of a system is calculated explicitly in real time, following the approach of Tsoiakidis *et al.* [18], using the SIESTA electronic structure code. A key result is a generalization of this approach for nonlinear dynamic responses using a quasi-monochromatic electric fields. While we use the same Crank-Nicholson time evolution operator for its accuracy, we have completely restructured the code and made the code to run faster and more efficiently. We also have made this real-time code to run in parallel processors for high-performance computing (HPC) facilities. Having HPC facilities, we can run the real-time simulation for a very large molecule or cluster of molecules including a few hundred atoms. Indeed, the parallelization is implemented in SIESTA ground-state calculation quite efficiently, and we have reused inner routines whenever

possible and incorporated them seamlessly into the original development. This effort is very important for future developments and improvements as SIESTA code is still developing and adding new features as well as bug fixes. We have minimized the maintenance cost for any future changes in SIESTA developments.

We have applied this approach to the non-centrosymmetric NLO molecules and obtained results in good agreement with experimental values. As far as we know, our implementation is the *only* accessible *ab initio* tool for calculating dynamic hyperpolarizability for large-scale photonic molecules at the desired accuracy. The advantage of the real-time TDDFT approach is actually not obvious when one is trying to a small system. It actually takes a much longer computation effort to perform the time-evolution calculation than the frequency-domain calculation for a small system. The present calculation cost of the real-time method is at most $\mathcal{O}(N^3)$, where N is the number of atoms involved, and the most time-consuming part is preparing the Hamiltonian at each time step as well as its inversion with the Crank-Nicholson time-evolution operator. However, we note that this is the same operation cost as the ground-state calculation, since the number of time steps that needs to be evaluated does not change with the number of atoms involved. Moreover, the required number of time steps to be evaluated usually decreases for the large system. The reason is that the large system is more stable with the presence of an external electric field, and the calculation will not diverge as quickly as the small system that enables us to use much larger time step during the simulation. For example, to obtain the time simulation for 20 fs, CO and H₂O molecule (5Z4P basis) require about $\Delta t = 0.1 \text{ Har}^{-1}$ whereas that for pNA (5Z4P basis) and YLD156 chromophore (DZDP basis) are about $\Delta t = 0.5 \text{ Har}^{-1}$.

We believe the development of real-time TDDFT for nonlinear dynamic optical response is as important as that of the success in the linear response. We already have shown that real-time TDDFT works well on small systems as well as the large system. Our development and implementation in parallel-process on a large cluster with an efficient DFT code of SIESTA is promising for further study. Following are the list of immediate interests in the future study:

- Improvement of the time-step operator scheme for the faster processing that works

efficiently for very large systems ($\sim 10^3$ to 10^4 atoms).

- Combination of real-time TDDFT and molecular dynamics (MD) and study phonon.
- Detailed solvent study with larger cluster and combining the MD.
- Study of higher-order hyperpolarizabilities such as second hyperpolarizability γ .
- Study of even larger molecules and help designing high-performance nonlinear molecules.
- Study of nonlinear properties of solids, crystals, and condensed system.

The field of photonics is undergoing exponential growth. The interests of organic and biological system are gaining more popularity in the field of making efficient and stable nonlinear optical devices, mainly for its performance and low production cost. We believe that this real-time method is one of the most promising tools for studying large molecular systems to help us design and characterize nonlinear organic materials.

BIBLIOGRAPHY

- [1] M. A. L. Marques X. Andrade, S. Botti and A. Rubio. *J. Chem. Phys.*, **126**(184106), 2007.
- [2] G. Cooper W. Chan and C. Brion. *Chem. Phys.*, **170**(123), 1993.
- [3] P. Salek, T. Helgaker, O. Vahtras, H. Ågren, D. Jonsson, and J. Gauss. *Mol. Phys.*, **103**(439), 2005.
- [4] D. P. Shelton and J. E. Rice. *Chem. Rev.*, **94**(3), 1994.
- [5] E. Schrödinger. *Am. Physik*, **79**(361), 1926.
- [6] T. T. Magel G. N. Lewis, D. Pipkin. *J. Am. Chem. Soc.*, **63**(3005), 1941.
- [7] T. H. Maiman. *Phys. Rev. Lett.*, **4**(564), 1960.
- [8] T. H. Maiman. *Naure*, **187**(493), 1960.
- [9] C. W. Peters P. A. Franken, A. E. Hill and G. Weinreich. *Phys. Rev. Lett.*, **7**(118), 1961.
- [10] J. F. Ward M. Bass, P. A. Franken and G. Weinreich. *Phys. Rev. Lett.*, **9**(446), 1962.
- [11] D. P. Chong. *J. Chinese Chem. Soc.*, **39**(375), 1992.
- [12] J. T. Carter D. P. Chong K. C. Casida M. E. Casida M. Wrinn J. Guan, P. Duffy. *J. Chem. Phys.*, **98**(4753), 1993.
- [13] J. G. Snijders S. J. A. van Gisbergen and E. J. Baerends. *J. Chem. Phys.*, **109**(10644), 1998.
- [14] P. Salek, O. Vahtras, T. Helgaker, and H. Ågren. *J. Chem. Phys.*, **117**(9630), 2002.
- [15] K. Yabana and G. F. Bertsch. *Phys. Rev. B*, **54**(4484), 1996.
- [16] F. D. Vila Y. Takimoto and J. J. Rehr. *J. Chem. Phys.*, **127**(154114), 2007.
- [17] C. Y. Yam F. Wang and G. Chen. *J. Chem. Phys.*, **126**(244102), 2007.

- [18] D. Sánchez-Portal A. Tsolakidis and R. M. Martin. *Phys. Rev. B*, **66**(235416), 2002.
- [19] P. Hohenberg and W. Kohn. *Phys. Rev.*, **136**(B864), 1964.
- [20] W. Kohn and L. J. Sham. *Phys. Rev.*, **140**(A1133), 1965.
- [21] D. M. Ceperley and B. J. Alder. *Phys. Rev. Lett.*, **45**(566), 1980.
- [22] A. D. Becke. *J. Chem. Phys.*, **98**(1372), 1993.
- [23] M. Ernzerhof J. P. Perdew and K. Burke. *J. Chem. Phys.*, **105**(9982), 1996.
- [24] D. Sánchez-Portal, P. Ordejón, E. Artacho, and J. M. Soler. *Int. J. Quantum Chem.*, **65**(453), 1997.
- [25] E. Artacho, D. Sánchez-Portal, P. Ordejón, A. García, and J. M. Soler. *Phys. Status Solidi B*, **215**(809), 1999.
- [26] P. Ordejón. *Phys. Status Solidi B*, **217**(335), 2000.
- [27] J. M. Soler, E. Artacho, J. D. Gale, A. García, J. Junquera, P. Ordejón, and D. Sánchez-Portal. *J. Phys.: Condens. Matter*, **14**(2745), 2002.
- [28] N. Troullier and J. L. Martins. *Phys. Rev. B*, **43**(1993), 1991.
- [29] L. Kleinman and D. M. Bylander. *Phys. Rev. Lett.*, **48**(1425), 1982.
- [30] O. F. Sankey and D. J. Niklewski. *Phys. Rev. B*, **40**(3979), 1989.
- [31] D. Sánchez-Portal, J. M. Soler and E. Artacho. *J. Phys.: Condens. Matter*, **8**(3859), 1996.
- [32] S. Huzinaga. *Comput. Phys. Rep.*, **2**(279), 1985.
- [33] A. Szabo and N. Ostlund. *Modern Quantum Chemistry*. Mac-Millan, New York, 1982.
- [34] C. J. Cramer. *Essentials of Computational Chemistry, 2nd Ed.* John Wiley & Sons, Ltd., 2004.
- [35] E. Runge and E. K. U. Gross. *Phys. Rev. Lett.*, **52**(997), 1984.
- [36] A. Zangrwill and P. Soven. *Phys. Rev. A*, **21**(1561), 1980.
- [37] R. van Leeuwen. *Phys. Rev. Lett.*, **80**(1280), 1998.

- [38] K. Yabana and G. F. Bertsch. *Int. J. Quantum Chem.*, **75**(55), 1999.
- [39] A. Rubio G. F. Bertsch, J. I. Iwata and K. Yabana. *Phys. Rev. B*, **62**(7998), 2000.
- [40] X. Lin X. Qian, J. Li and S. Yip. *Phys. Rev. B*, **73**(035408), 2006.
- [41] M. E. Casida. *Recent Advances in Density-Functional Methods, Vol. 3 of Part I, Vol. 3 of Part I, edited by D. A. Chong*. World Scientific, Singapore, 1995.
- [42] G. E. Scuseria R. E. Stratmann and M. J. Frisch. *J. Chem. Phys.*, **109**(8218), 1998.
- [43] R. Bauernschmitt and R. Ahlrichs. *Chem. Phys. Lett.*, **256**(454), 1996.
- [44] K. C. Casida M. E. Casida, C. Jamorski and D. R. Salahub. *J. Chem. Phys.*, **108**(4439), 1998.
- [45] I. Vasiliev, S. Ögüt, and J. R. Chelikowsky. *Phys. Rev. Lett.*, **82**(1919), 1999.
- [46] F. Furche and R. Ahlrichs. *J. Chem. Phys.*, **117**(7433), 2002.
- [47] F. H. Hennrich R. Bauernschmitt, R. Ahlrichs and M. M. Kappes. *J. Am. Chem. Soc.*, **120**(5052), 1998.
- [48] R. E. Stratmann K. B. Wiberg and M. J. Frisch. *Chem. Phys. Lett.*, **297**(60), 1998.
- [49] M. Head-Gordon C. P. Hsu, G. R. Fleming and T. Head-Gordon. *J. Chem. Phys.*, **114**(3065), 2001.
- [50] M. Head-Gordon S. Hirata and R. J. Bartlett. *J. Chem. Phys.*, **111**(10774), 1999.
- [51] L. Reining G. Onida and A. Rubio. *Rev. Mod. Phys.*, **74**(601), 2002.
- [52] J. Werschnik K. Burke and E. K. U. Gross. *J. Chem. Phys.*, **123**(62206), 2005.
- [53] A. Zangwill. *J. Chem. Phys.*, **78**(5926), 1983.
- [54] F. Furche. *J. Chem. Phys.*, **114**(5982), 2001.
- [55] S. Tretiak and V. Chernyak. *J. Chem. Phys.*, **119**(8809), 2003.
- [56] G. F. Bertsch A. Rubio M. A. L. Marques, A. Castro. *Comput. Phys. Commun.*, **151**(60), 2003.
- [57] S. Mukamel. *Phys. Rev. A*, **71**(24503), 2005.

- [58] A. Ye and J. Autschbach. *J. Chem. Phys.*, **125**(234101), 2006.
- [59] J. Crank and P. Nicholson. *Proc. Cambridge Philos. Soc.*, **43**(50), 1947.
- [60] J. J. Rehr and R. Alben. *Phys. Rev. B*, **16**(2400), 1977.
- [61] R. M. Martin. *Electronic Structure: Basic Theory and Practical Methods*. Cambridge University Press, Cambridge, 2004.
- [62] M. A. L. Marques A. Castro and A. Rubio. *J. of Chem. Phys.*, **121**(3425), 2004.
- [63] H. D. Cohen and C. C. J. Roothaan. *J. Chem. Phys.*, **43**(S34), 1965.
- [64] Jr. J. A. Pople, J. W. McIver and N. S. Ostlund. *J. Chem. Phys.*, **49**(2960), 1968.
- [65] J. I. Iwata G. F. Bertsch K. Yabana, T. Nakatsukasa. *physica status solidi (b)*, **243**(1121), 2006.
- [66] D. E. Makarov W. Kohn, Y. Meir. *Phys. Rev. Lett.*, **80**(4153), 1998.
- [67] P. N. Butcher and D. Cotter. *The Elements of Nonlinear Optics*. Cambridge University Press, Cambridge, 1990.
- [68] M. Dupuis F. Sim, S. Chin and J. E. Rice. *J. Chem. Phys.*, **97**(1158), 1993.
- [69] K. Burke J. P. Perdew and M. Ernzerhof. *Phys. Rev. Lett.*, **77**(3865), 1996.
- [70] D. M. Burland A. Willetts, J. E. Rice and D. P. Shelton. *J. Chem. Phys.*, **97**(7590), 1992.
- [71] E. A. Donley P. Kaatz and D. P. Shelton. *J. Chem. Phys.*, **108**(849), 1998.
- [72] J. C. J. Decius S. J. Cyvin, J. E. Rauch. *Chem. Phys.*, **43**(4083), 1965.
- [73] G. Maroulis. *J. Phys. Chem.*, **100**(13466), 1996.
- [74] J. G. Snijders S. J. A. van Gisbergen and E. J. Baerends. *J. Chem. Phys.*, **109**(10644), 1998. ; **111**, 6652 (E) (1999).
- [75] J. S. Muentner. *J. Mol. Spectrosc.*, **55**(490), 1975.
- [76] G. A. Parker and R. T. Pack. *J. Chem. Phys.*, **64**(2010), 1976.
- [77] M. E. Casida and D. R. Salahub. *J. Chem. Phys.*, **113**(8918), 2000.

- [78] M. Honigmann G. Hirsch L. Chanturanpong, K. Bhanuprakash and R. J. Buenker. *Chem. Phys.*, **161**(351), 1992.
- [79] K. Kirby and L. L. Cooper. *J. Chem. Phys.*, **90**(4895), 1989.
- [80] M. F. Herman D. Lynch and D. L. Yeager. *Chem. Phys.*, **64**(69), 1982.
- [81] P. Jorgensen E. S. Nielsen and J. Oddershede. *J. Chem. Phys.*, **73**(6238), 1980.
- [82] B. V. McKoy N. Padial, G. Casanak and P. W. Langhoff. *J. Chem. Phys.*, **69**(2992), 1978.
- [83] M. H. Wood. *Chem. Phys. Lett.*, **28**(477), 1974.
- [84] T. Shibuya W. Coughran, J. Rose and V. McKoy. *J. Chem. Phys.*, **58**(2699), 1973.
- [85] T. Shibuya J. Rose and V. McKoy. *J. Chem. Phys.*, **58**(74), 1973.
- [86] J. Breton M. Eidelsberg, F. Rostas and B. Thieblemont. *J. Chem. Phys.*, **96**(5583), 1992.
- [87] M. Lavollée R. Lopez-Delgado R. W. Field, O. Benoist d’Azy and A. Tramer. *J. Chem. Phys.*, **78**(2838), 1983.
- [88] E. N. Lassettre and A. Skerbele. *J. Chem. Phys.*, **54**(1597), 1971.
- [89] R.W. Weast (Ed.). *Handbook of Chemistry and Physics, 77th ed.* Chemical Rubber, Boca Raton FL, 1996.
- [90] B. H. Robinson E. R. Davidson, B. E. Eichinger. *Optical Materials*, **29**(360), 2006.
- [91] M. J. Frisch, G. W. Trucks, H. B. Schlegel, G. E. Scuseria, M. A. Robb, J. R. Cheeseman, J. A. Montgomery, Jr., T. Vreven, K. N. Kudin, J. C. Burant, J. M. Millam, S. S. Iyengar, J. Tomasi, V. Barone, B. Mennucci, M. Cossi, G. Scalmani, N. Rega, G. A. Petersson, H. Nakatsuji, M. Hada, M. Ehara, K. Toyota, R. Fukuda, J. Hasegawa, M. Ishida, T. Nakajima, Y. Honda, O. Kitao, H. Nakai, M. Klene, X. Li, J. E. Knox, H. P. Hratchian, J. B. Cross, C. Adamo, J. Jaramillo, R. Gomperts, R. E. Stratmann, O. Yazyev, A. J. Austin, R. Cammi, C. Pomelli, J. W. Ochterski, P. Y. Ayala, K. Morokuma, G. A. Voth, P. Salvador, J. J. Dannenberg, V. G. Zakrzewski, S. Dapprich, A. D. Daniels, M. C. Strain, O. Farkas, D. K. Malick, A. D. Rabuck, K. Raghavachari, J. B. Foresman, J. V. Ortiz, Q. Cui, A. G. Baboul, S. Clifford, J. Cioslowski, B. B. Stefanov, G. Liu, A. Liashenko, P. Piskorz, I. Komaromi, R. L. Martin, D. J. Fox, T. Keith, M. A. Al-Laham, C. Y. Peng, A. Nanayakkara, M. Challacombe, P. M. W. Gill, B. Johnson, W. Chen, M. W. Wong, C. Gonzalez, , and J. A. Pople. Gaussian 03, revision b.04, 2003.

- [92] T. Pluta and A. J. Sadlej. *Chem. Phys. Lett.*, **297**(391), 1998.
- [93] T.L.J. Weatherly P.B. Reinhart, Q. Williams. *Chem. Phys.*, **53**(1418), 1970.
- [94] D. P. Shelton P. Kaatz. *Optics Comm.*, **157**(177), 1998.
- [95] B. F. Levin. *Chem. Phys. Lett.*, **37**(516), 1976.
- [96] K. Clays and A. Persoons. *Phys. Rev. Lett.*, **66**(2980), 1991.
- [97] O. Ito M. Matsuda K Clays T. Kodaira, A. Watanabe and A. Persoons. *J. Chem Soc., Faraday Trans.*, **93**(3039), 1997.
- [98] A. M. Moran and A. M. Kelley. *J. Chem. Phys.*, **115**(912), 2001.
- [99] C. C. Teng and A. F. Garito. *Phys. Rev. B*, **28**(6766), 1983.
- [100] S. P. Karna and P. N. Prasad. *J. Chem. Phys.*, **94**(1171), 1991.
- [101] H. Ågren, O. Vahtras, H. Koch, P. Jørgensen, and T. Helgaker. *J. Chem. Phys.*, **98**(6417), 1993.
- [102] H. Soscún, O. Castellano, Y. Bermúdez, C. Toro, N. Cubillán, A. Hinchliffe, X. Nguyen Phu. *International Journal of Quantum Chemistry*, **106**(1130), 2006.
- [103] O. Zamani-Khamiri J. R. Heflin, K. Y. Wong and A. F. Garito. *Phys. Rev. B*, **38**(1573), 1988.
- [104] Z. G. Soos and G. W. Hayden. *Phys. Rev. B*, **40**(3081), 1989.
- [105] Alex K-Y. Jen K. Y. Wong and V. Pushkara Rao. *Phys. Rev. A*, **49**(3077), 1994.
- [106] W. M. Wijekoon S. P. Karna, G. B. Talapatra and P. N. Prasad. *Phys. Rev. A*, **45**(2763), 1992.
- [107] Z. Shuai and J. L. Brédas. *Phys. Rev. B*, **62**(15452), 2000.
- [108] P. A. Sullivan A. J. P. Akelaitis B. H. Robinson Y. Liao, C. A. Anderson and L. R. Dalton. *Chem. Mater.*, **18**(1062), 2006.
- [109] S. K. Lee G. McGrew S. K. Lee D. H. Choi P. A. Sullivan, A. J. P. Akelaitis and L. R. Dalton. *Chem. Mater.*, **18**(344), 2006.

- [110] Y. Liao B. C. Olbricht A. J. P. Akelaitis K. A. Firestone J-W. Kang J. Luo J. A. Davies D. H. Choi B. E. Eichinger P. J. Reid A. Chen A. K-Y. Jen B. H. Robinson P. A. Sullivan, H. Rommel and L. R. Dalton. *J. Am. Chem. Soc.*, **129**(7523), 2007.
- [111] O. Vahtras, H. Ågren, P. Jørgensen, H. J. Aa. Jensen, T. Helgaker, and J. Olsen. *J. Chem. Phys.*, **97**(9178), 1992.
- [112] H. Hettema, H. J. Aa. Jensen, P. Jørgensen, and J. Olsen. *J. Chem. Phys.*, **97**(1174), 1992.
- [113] K. Clays and A Persoons. *Rev. Sci. Instrum.*, **63**(3285), 1992.
- [114] P. Debye. *Physik. Z.*, **13**(97), 1912.
- [115] L. Onsager. *J. Am. Chem. Soc.*, **58**(1486), 1936.
- [116] J. Tomasi and M. Persico. *Chem. Rev.*, **94**(2027), 1994.

Appendix A

WHERE TO FIND THE CODE AND SYSTEM REQUIREMENT

A.1 *Obtaining the Code*

Our real-time TDDFT code is based on the DFT electronic structure code SIESTA available at <http://www.uam.es/departamentos/ciencias/fismateriac/siesta/>. You need to obtain the SIESTA source code, in order to use our time-dependent extension. SIESTA is distributed freely for academics, including their program source code, under conditions set by the license agreement. Non-academic distribution is available through Nanotec (<http://www.nanotec.es/>). In either case, please visit the SIESTA website above to find out how to obtain the source code.

Our current version of real-time TDDFT code works together with version 2.0.1 of SIESTA. Since our code is *in-process* instead of *post-process* of SIESTA calculation, you need to modify or patch the original SIESTA source to integrate our modification. At the present form of development, we do not guarantee SIESTA code will behave exactly the same as the original, even if you are not calculating real-time evolution. We suggest keeping the original and using it for any of non-time-dependent calculations, such as geometry optimization.

In order to obtain our source, please inquire about its availability to professor John J. Rehr jjr@phys.washington.edu.

A.2 *System Requirement*

The platform requirement is exactly the same as for the SIESTA code. You need appropriate FORTRAN90/95 compiler on your platform for the compilation. If this condition is met, you should be able to run on such widely available operating systems as Linux, BSD UNIX, Apple OS X, and Microsoft Windows.

Scripting language of Perl (<http://www.perl.com/>) is required for pre-process to help making input files as well as that of OCTAVE (<http://www.octave.org/>) for post-process

to calculate final spectra. We have used and tested on the version `v5.8.8` for `Perl` and `v2.1.73` for `OCTAVE`.

Appendix B

REAL-TIME TDDFT PROGRAM MANUAL

B.1 Quick Start Guide

The real-time TDDFT distribution package consists of a set of files and directories. After unpacking the source distribution, `rt-tddft****.tar.gz` where, “****” is the version control number, you will find the following sub-directories:

```
rt-tddft/examples
rt-tddft/patch
rt-tddft/utis
```

The directory “utis” contains the scripts for pre-process and post-process:

```
utis/prepsiesta : TDDFT preparation script (Perl script)
utis/hypfits : TDDFT post-process script (Octave script)
```

The directory “patch” contains the patch “diff” file, `tddft-current.diff` needed to modify the original SIESTA source code of version 2.0.1.

Following are optional scripts to help in running a set of jobs:

```
utis/submit_jobs : Script for running multiple jobs (require to edit)
utis/submit_to_queue : Used together with the script above
```

The other utility scripts may be used for analysis, as will be explained below.

B.1.1 Compilation

Create a working directory and untar the SIESTA source code `siesta-2.0.1.tgz`.

```
$ tar xzf siesta-2.0.1.tgz
```

Unpack the real-time TDDFT distribution `rt-tddft****.tar.gz`, where “****” is the version control number.

```
$ tar xzf rt-tddft****.tar.gz
```

Apply the patch to modify the original source code.

```
$ patch -p1 -d siesta-2.0.1 < patch/tddft-current.diff
```

Build the program from source the same way as the original SIESTA. Go to the “**Src**” directory; you will then need to provide an architecture-dependent configuration file called **arch.make**. There are number of examples in the “**Src/Sys**” sub-directory. If your system has an architecture whose required compiler and libraries exactly match to one of a sample file in “**Sys**” sub-directory (unfortunately, very unlikely), you can simply create a symbolic link to the file:

```
$ ln -sf Sys/xxx.make arch.make
```

where “**xxx**” is the name of configuration file. In the default setting, SIESTA calculates the density on a grid using single precision; I would suggest adding “**FPFLAGS = -DGRID_DP**” to help improve the SCF convergence and the accuracy of the dipole moment to be calculated.

Then, type **make** to compile the source code from **Makefile**:

```
$ make
```

If the compilation is successful, a binary file “**siesta**” will be created. This is the main executable for the SIESTA program. You will also need to read the SIESTA manual available at <http://www.uam.es/siesta> for further detail.

If you need to create a parallel-architecture version of SIESTA, please first read the basic tutorial available in the following section on parallel computing. It is important to note that if you are running the real-time SIESTA in parallel, you need to specify that the number of working processors be equal to an integer squared (4, 9, 16, ... and so on) in order to make the matrix-inversion operation run in parallel. If you try to run on any other number of processors, only the head node performs the inversion, causing significant performance deration, and/or you experience memory issues on the head node.

B.2 Static Calculation

1.) Static calculation of linear and nonlinear (hyper)polarizability is possible with the plain SIESTA code. However, it is important to start with static calculation, since the quality of

the final result depends on the performance on the static limit. We take a water molecule as an example. We use a sample SIESTA input file available in the “Examples” directory. Let’s make a working directory and go to the directory:

```
$ mkdir h2o
$ cd h2o
$ cp ~/siesta-2.0.1/Examples/H2O/h2o.fdf .
```

2.) Running the SIESTA a calculation requires corresponding pseudopotentials file for each atom in the molecule. Here, we simply take the ones available on the SIESTA website pseudopotentials database. With your favorite browser, you need to open the following URL:

<http://www.uam.es/siesta/>. Then, follow the link Pseudos & Basis in the left menu, then click on the link Translation of Abinit’s GGA pseudo database to Siesta format. For water, we need pseudopotentials for H and O atoms. Click on the element H. You will find the link “Link to siesta input psf.” To save the pseudopotential file, right-click on the link psf and choose “Save Link As” (option may vary with browser) and save the file as “H.psf,” repeat the process and obtain “O.psf” as well. Copy the saved pseudopotentials, H.psf and O.psf, to the working directory you have just created.

3.) Using a text editor, you need to edit the SIESTA input file for water h2o.fdf and insert the following options,

```
TD.ShapeOfEfield      step # use step function for linear response
TD.NumberOfTimeSteps  1    # number of time steps,
```

where the words after “#” are the comments. The keyword TD.ShapeOfEfield specifies the shape of the external field. Since static calculation requires a constant field, we use the step function which provides a constant field for $t < 0$.

4.) A minimum of five field strengths is required in order to calculate the static values of hyperpolarizabilities. You need to use pre-process `prepsiesta` script to prepare all required inputs. It is advisable to save the scripts under “rt-tddft/utis” to a directory listed in one of the directories under the \$PATH shell variable. Assuming you already have done so (I assume all utilities scripts *and* siesta binary are copied under a directory in \$PATH for

the rest of this tutorial), you now type

```
$ prepsiesta -e "0.0 0.005 0.01" h2o.fdf ,
```

where ‘-e’ is the option to specify the strength of the external electric field in the atomic unit. The addition of zero field in the decimal format is always required.

The above command creates five folders {1 2 3 4 5}, each one corresponding to the specified field strengths where the directory 1 for $E = 0.0$, 2 for $E = 0.005$, 3 for $E = -0.005$, 4 for $E = 0.01$, and 5 for $E = -0.01$. Note that you only need to specify the “positive” fields; corresponding directories for the negative fields are automatically created. In addition, under the five folders just created, there are three additional subfolders {1 2 3} under each directory. These subfolders correspond to three spatial axes, i.e., the x-, y-, and z-direction of the external fields. Note that the zero-field does not have any preferred direction; the 1/2 and 1/3 subfolders are the symbolic link to the 1/1 subfolder. The task of the script **prepsiesta** is quite simple: it copies all pseudopotentials under the working directory and adds an electric field to the input file **h2o.fdf**, and saves the input file as **input.fdf**. For example, under the directory 2/1, following the SIESTA input statement is appended at the end of the **h2o.fdf** file:

```
%block ExternalElectricField
0.005 0.0000 0.0000 Har/Bohr/e
%endblock ExternalElectricField
```

5.) Now, you are ready to run the calculation. There are a total of 13 unique folders {1/1 2/1 2/2 2/3 3/1 3/2 3/3 4/1 4/2 4/3 5/1 5/2 5/3}, and you need to run SIESTA in each unique folder.

```
$ cd 1/1
$ siesta < input.fdf | tee output.log
```

The above will execute **siesta** from the input file in the directory. You will need to wait until the calculation is completed. Many output files are generated during the execution. Beside SIESTA outputs, two extra files are also generated. They are **dipole.vs.time** and **energy.vs.time**, as their names suggest, these two files store the dipole v.s. time and the total energy v.s. time evolutions. After this calculation is completed, you will need to go

to the next directory and execute `siesta`.

```
$ cd ../../2/1
```

```
$ siesta < input.fdf | tee output.log
```

6.) You must repeat this process and run `siesta` under all remaining folders. To automate this repetition, shell scripts are available. You will need to edit `submit_jobs` and `submit_to_queues` in the “`rt-tddft/utils`” folder. In the script `submit_jobs`, one must set the variable `$SCRIPT_DIR` to specify the location of `submit_to_queues` file. In the `submit_to_queues` file, one must set the variable `$SIESTA_CMD` to specify the location of `siesta` executable file. If the `submit_jobs` file is located under `$PATH`, execution of the following command under the working directory will process all 13 subfolders sequentially:

```
$ submit_jobs
```

If a machine has multiple processing cores, you can run multiple jobs, i.e.:

```
$ submit_jobs 4
```

The above will execute four processes at a time. If you set up correctly for a cluster facility, you can run multiple processes in parallel such that each process may utilize multiple processors.

After all jobs are completed, it is necessary to post-process all the results together to get (hyper)polarizabilities with “`hypfits`” script. Execute the `OCTAVE` script:

```
$ hypfits
```

This starts the interactive mode and will ask you to input several parameters before processing. In general, you can leave all parameters as suggested by the default values which enclosed by the square brackets [...]; so you will have to keep pressing the `ENTER` key repeatedly until the script starts to analyze the `dipole.vs.time` files.

7.) The main output file for the static calculation is “`hypfits.output.dat`.” Several numbers are listed in somewhat cryptic form that needs some explanation. The main result starts from the real part of (hyper)polarizability, tagged by “`# real part`”:

```
# real part (0.000 eV)
```

At this point, the subsequent three rows give (hyper)polarizabilities in physical units, in each column, with the exception of the first three columns read from the first column as follows: “the frequency of external field”, “the order of electric field in the dipole moment

expansion”, and “the frequency of output field.” In case of the static field, the first and the third columns are all zero. Then, the data columns of physical units are listed as follows

```
# real part (0.000 eV)
0.00 0 0.00  d_x  d_y  d_z
0.00 1 0.00  a_xx a_xy a_xz a_yx a_yy a_yz a_zx a_zy a_zz
0.00 2 0.00 b_xxx b_xxy b_xxz b_yyx b_yyy b_yyz b_zzx b_zyy b_zzz b_z b_HRS,
```

where d_i is the permanent dipole moment μ_i in Debye, a_{ij} is the linear polarizability α_{ij} in \AA^3 , and b_{ijk} is the first hyperpolarizability β_{ijk} in 10^{-30} esu. Note that the tensor component of the first hyperpolarizabilities β_{xyz} , β_{xzy} , and β_{yxz} are not explicitly calculated. Two additional data columns of β are β_z for EFISH vector average and β_{HRS} for HRS rotational average. The rows below [atomic units] list the same results as above, but in the atomic units for convenience. There is also an extra row for the second hyperpolarizability γ_{ijkl}

```
0.00 3 0.00 g_xxxx g_xxyy g_xxxz g_yyyx g_yyyy g_yyyz g_zzzx g_zzyy g_zzzz.
```

Those γ values are usually not meaningful unless you have prepared the basis set carefully for calculating the third-order effect. In addition, you will need at least seven field strengths to get the second hyperpolarizability values accurately. The rows tagged after “# imag part” are the imaginary part of (hyper)polarizabilities where the static values are all identically zero.

The rows tagged after “# hyprot: real part” list (hyper)polarizabilities repeated as before, except that all tensor components are rotated to orient the z-axis in the direction of the permanent dipole moment. You will get different values only if you have supplied a molecular dipole moment not aligned along the z-axis. The 3x3 matrix after the tag “Rotation Matrix = ” is the rotation matrix used for the rotation above. This script also outputs the rotation matrix in a separate file `rot.m`.

B.3 Linear Response Calculation

The calculation of linear response is very similar to the static calculation, except that you now need to propagate in real time.

- 1.) Prepare a fresh working directory and input files, as in steps 1. and 2. of the static calculation tutorial. The SIESTA input file should include all necessary parameters except the `ExternalElectricField` block.
- 2.) Using a text editor, you need to edit the SIESTA input file and add the following options for the TDDFT calculation. For the TDDFT linear calculation, `TD.TimeStep` and `TD.NumberOfTimeSteps` are the only necessary parameters that you might want to change.

```

TD.TimeStep          0.07 # time step in 1/Ryd
TD.NumberOfTimeSteps 1000 # number of time steps
TD.ShapeOfEfield     step # use step function for linear response

```

The optimal value of the `TD.TimeStep` varies from systems to systems. In general, you need a smaller time step for a smaller system, and, of course, you need to choose a smaller time step for a longer run. We suggest you to try running once with relatively large time step size, and thus find out when the system begins to diverge. The error of the Crank-Nicholson time-evolution operator is on the order of $\mathcal{O}(\Delta t^2)$. For example, suppose you run the evolution for 5000 time steps and your test run starts to diverge around 2500 time steps, using the step size of $\Delta t = 0.07$. In order to complete the simulation, you will need to decrease Δt by $\Delta t/\sqrt{2} \approx 0.05$ and increase the number of time steps N by $N\sqrt{2} \approx 7000$.

In fact, the parameter `TD.NumberOfTimeSteps` is not convenient, since a user is usually interested in the “sharpness” or resolution of the final spectra in the linear-response calculation. You will find the following set of parameters are more useful:

```

TD.TimeStep          0.07  # time step in 1/Ryd
TD.EnergyResolution  0.1 eV # the resolution of final spectra
TD.ShapeOfEfield     step  # use step function for linear response,

```

where you set the resolution of the spectra, and the required number of time steps N is determined by

$$N = \pi/(\Delta E * \Delta t), \quad (\text{B.1})$$

where ΔE is the energy resolution in a.u. and Δt is the time step in a.u..

2.) In the case of linear response, a minimum of three field strengths ($-E, 0, E$) is required.

Run the script `prepsiesta`:

```
$ prepsiesta -e "0.0 0.001" input.fdf
```

NOTE: “-e” is the option for specifying the strength of electric fields in the atomic unit.

3.) The following directories are created:

```
{1/1 2/1 2/2 2/3 3/1 3/2 3/3}
```

The sub-directory under 1 is for the zero field calculation, under 2 for the positive strength $E = 0.001$, and under 3 for the negative strength $E = -0.001$.

4.) Next, you need to run SIESTA in each of the 7 unique folders. The zero field directory 1/1 does not evolve in time, so the runtime execution is short and stops shortly after the SCF loop. The other 6 unique folders will be the real-time simulation with the number of steps specified in the input file.

For a spherically symmetrical system, or when only z-component response is needed, you will only need to run 1/1, 2/3, and 3/3 (one ground-state, and two long jobs).

5.) Run `hypfits` within the working directory after completion. You may leave all parameters as specified by the default values, except for the damping factor, which you will probably want to change. Note that this script is quite slow, since I am using the “slow” Fourier transform, not the fast Fourier transform (FFT) algorithm.

6.) The main output file for the linear response is `hypfits.chi.vs.omega.dat` file. The first column is the energy in eV. For the linear response, the output of interest is either $\text{Im } \alpha(\omega)$ or (column 1 through 10) $\text{Re } \alpha(\omega)$ (column 20 through 28).

The data columns for $\text{Im } \alpha_{ij}(\omega)$ (a.u.) in `hypfits.chi.vs.omega.dat` are given by

```
xx, xy, xz (column 2, column 3, column 4)
yx, yy, yz (column 5, column 6, column 7)
zx, zy, zz (column 8, column 9, column 10)
```

The data columns for $\text{Re } \alpha_{ij}(\omega)$ (a.u.) in `hypfits.chi.vs.omega.dat` are given by

```
xx, xy, xz (column 20, column 21, column 22)
yx, yy, yz (column 23, column 24, column 25)
```

zx, zy, zz (column 26, column 27, column 28)

For example, use a favorite plotting program and plot `hypfits.chi.vs.omega.dat` for analyzing data

$\text{Im} \langle \alpha(\omega) \rangle : \text{plot col1 vs (col2 + col6 + col10)}/3$

$\text{Re} \langle \alpha(\omega) \rangle : \text{plot col1 vs (col20 + col24 + col28)}/3,$

where $\langle \alpha(\omega) \rangle$ is the average polarizability.

B.3.1 Damping Factor

The frequency-dependent response is determined by the Fourier transformation of the dipole moment $\mathbf{d}(t)$ by

$$\mathbf{d}(\omega) \equiv \int_0^T dt e^{i\omega t} e^{-\delta t} \mathbf{d}(t), \quad (\text{B.2})$$

where δ is a real positive definite damping factor is introduced in order to perform the Fourier transformation within a finite simulation time T . This damping factor gives a minimum width of the peaks of the imaginary part of the response. If you specify `TD.EnergyResolution` in the input file, the default damping factor will be this value. The exponential damping is especially useful when you are comparing against an experimental measurement including the lifetime and instrumental broadening factor. If this damping factor is too small, you will get the Fourier ripples effect, so that the frequency spectra suffers from the unreal Fourier ripples errors. Note that the Fourier transformation of the damping function gives the Lorentzian function

$$\text{FT} \left[e^{-\delta|t|} \right] (\omega) = \frac{2\delta}{\omega^2 + \delta^2} = \frac{\Gamma_\delta}{\omega^2 + \left(\frac{1}{2}\Gamma_\delta\right)^2}, \quad (\text{B.3})$$

where the Lorentzian width $\Gamma_\delta = 2\delta$. Hence 2δ of the damping factor above gives the FWHM broadening line width in the frequency space.

B.3.2 F-sum

The other quantity of interest for checking internal consistency is the f-sum, which is the sum of the dipole oscillator strength. Column 40 of `hypfits.chi.vs.omega.dat` shows the

cumulative sum of valence electron count. However, it is important to note that if you use the exponential damping function, the total electron counts will not be conserved. If you want to check the f-sum more precisely, you should use the third-order polynomial damping function

$$p^{(n)}(\omega) \equiv \int_0^T dt e^{i\omega t} \left[1 - 3 \left(\frac{t}{T} \right)^2 + 2 \left(\frac{t}{T} \right)^3 \right] p^{(n)}(t), \quad (\text{B.4})$$

where T is the total simulation time. This polynomial function in the square bracket $f(t)$ has the properties $f(0) = 1$, and $f(T) = f'(0) = f'(T) = 0$. The conditions $f(T) = f'(T) = 0$ ensure the $p^{(n)}(t)$ vanishes smoothly at $t = T$. The condition $f'(0) = 0$ guarantees that the f-sum rule is not changed by introducing this damping function [65]. The corresponding FWHM line width is $\Gamma_\delta \sim 6.2/T \sim 2\Delta E$. You can choose this polynomial damping during `hypfits` execution.

B.4 Nonlinear Response Calculation

1.) Prepare a fresh working directory and input files, as for steps 1. and 2. of the static calculation tutorial. The SIESTA input file should include all necessary parameters for running the ground-state calculation except the `ExternalElectricField` block. You need to set following additional parameters for the nonlinear calculation:

```

TD.ExternalFrequency    1.00 eV # The frequency of the external field
TD.EnergyResolution     0.1  eV # Smaller the resolution, longer the simulation
TD.TimeStep             0.07   # Time step in 1/Ryd
TD.ShapeOfEfield        sine   # sine wave
TD.ExternalPacket       .true.  # make the wave enveloped by Gaussian

```

2.) In the case of nonlinear response, a minimum of five field strengths ($-2E$, $-E$, 0 , E , $2E$) is required. Run the script `prepsiesta`

```
$ prepsiesta -e "0.0 0.001 0.002" input.fdf
```

3.) The following directories are created:

```
{1/1 2/1 2/2 2/3 3/1 3/2 3/3 4/1 4/2 4/3 5/1 5/2 5/3}
```

The input file under the sub-directory in 1 is for the zero field, under 2 for positive strength $E = 0.001$, under 3 for negative strength $E = -0.001$, under 4 for positive strength $E = 0.002$, and under 5 for negative strength $E = -0.002$.

4.) Run SIESTA in each unique 13 folders (one ground-state, and 12 long jobs).

For a spherically symmetrical system, or when only the z-component response is needed, you will only need to run 1/1, 2/3, 3/3, 4/3, and 5/3 (4 long jobs).

5.) Run `hypfits` within the working directory after completion. You may leave all parameter as specified by the default.

6.) The main output file for the nonlinear response is `hypfits.output.dat`. Please be careful to note that unlike static response output of (hyper)polarizabilities, not all of the outputs are meaningful.

You will find three different frequencies tagged by “# `hyprot: real part (ω eV)`,” with $\omega = 0$, $\omega = \omega_0$, and $\omega = 2\omega_0$, where ω_0 is the frequency of the external electric field specified by `TD.ExternalFrequency`.

In particular, the result of nonlinear response results are $\beta_{ijk}(0; \omega, -\omega)$ and $\beta_{ijk}(-2\omega; \omega, \omega)$. First, the hyperpolarizability $\beta_{ijk}(0; \omega, -\omega)$ components are listed as:

```
# hyprot: real part (0.000 eV)
...
0.00 2 0.00 b_xxx b_xxy b_xxz b_yyx b_yyy b_yyz b_zzx b_zzy b_zzz b_z b_HRS
```

Next, $\beta_{ijk}(-2\omega; \omega, \omega)$ components are listed as:

```
# hyprot: real part (2.000 eV)
...
0.00 2 2.00 b_xxx b_xxy b_xxz b_yyx b_yyy b_yyz b_zzx b_zzy b_zzz b_z b_HRS,
```

where it is assumed that $\omega = 1.000$ eV. The meaning of all components are the same as static case.

In addition to the nonlinear first hyperpolarizabilities, the linear polarizabilities are also listed; $\alpha_{ij}(\omega)$ components are listed as:

```
# hyprot: real part (1.000 eV)
...
0.00 1 1.00  a_xx  a_xy  a_xz  a_yx  a_yy  a_yz  a_zx  a_zy  a_zz
```

B.4.1 Gaussian Envelope Function

Following combination of keywords in the input file produces the external electric field in monochromatic sine wave enveloped by the Gaussian function.

```
TD.ExternalFrequency  1.00 eV
TD.EnergyResolution    0.1 eV
TD.ShapeOfEfield       sine
TD.ExternalPacket      .true.
```

The shape of Gaussian envelope is automatically determined from `TD.EnergyResolution`. More specifically, the actual shape of the external electric field has a form

$$E(t) = \sin(\omega t) \exp\left(-\frac{1}{2} \frac{(t - t_c)^2}{\sigma^2}\right), \quad (\text{B.5})$$

where `ExternalFrequency` = ω , and the Gaussian function gives the full width at half maximum (FWHM) by

$$\text{FWHM} = 2\sqrt{2\ln 2}\sigma \approx 2.35482\sigma. \quad (\text{B.6})$$

The Fourier transformation of Gaussian is

$$\text{FT}\left[\exp\left(-\frac{1}{2}\frac{t^2}{\sigma^2}\right)\right](\omega) = \sqrt{2\pi\sigma^2} \exp\left(-\frac{1}{2}\sigma^2\omega^2\right) = \sqrt{2\pi\sigma^2} \exp\left(-\frac{1}{2}\frac{\omega^2}{1/\sigma^2}\right). \quad (\text{B.7})$$

Next, the default σ of the Gaussian envelope is chosen such that

$$\pi * \Delta E \equiv \text{FWHM}(\omega) \approx 2.35482/\sigma \quad (\text{B.8})$$

$$\sigma = 2.35482/(\pi\Delta E), \quad (\text{B.9})$$

where $\text{FWHM}(\omega)$ is the corresponding FWHM in the frequency space in which ΔE is given by `TD.EnergyResolution` in the atomic unit (the introduction of π is rather arbitrary where

the value between 3 to 4 gives a good Gaussian bell shape within the total simulation time $T = \pi/\Delta E$.)

The default value of the central peak t_c is simply set at $T/2$, where T is the total simulation time given by

$$t_c = T/2 = N\Delta t/2 \quad (\text{B.10})$$

$$= \pi/(2\Delta E). \quad (\text{B.11})$$

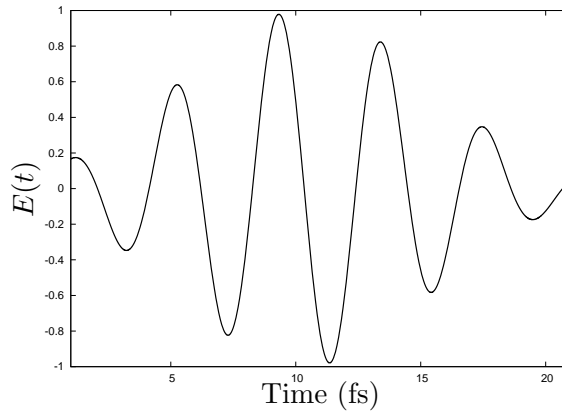


Figure B.1: Quasi-monochromatic external field with **ExternalFrequency** = 1.0 eV and **EnergyResolution** = 0.1 eV. The shape of Gaussian function is determined automatically as described in Eq. (B.9) and Eq. (B.11) where the central peak is located at $T/2$ of the total simulation time T .

B.4.2 Sine Envelope Function

The following combination of keywords in the input file produces the external electric field in monochromatic sine wave enveloped by another sine wave.

```

TD.ExternalFrequency    1.00 eV
TD.EnergyResolution      0.1 eV
TD.ExternalFrequency2   0.1 eV
TD.ShapeOfEfield        sine2
TD.ExternalPacket        .true.

```

The actual shape of the external electric field has a form

$$E(t) = \sin(\omega t) \sin(\omega_2 t), \quad (\text{B.12})$$

where `ExternalFrequency` = ω and `ExternalFrequency2` = ω_2 . Since the default total simulation time is given by $T = \pi/\Delta E$, the value `ExternalFrequency2` equals to `EnergyResolution` makes the envelope of the external sine field by half period of the second sine.

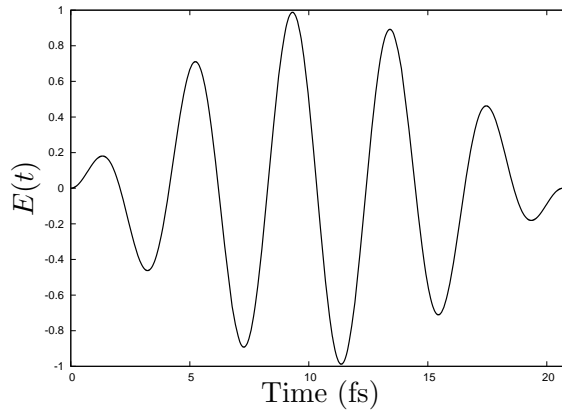


Figure B.2: Quasi-monochromatic external field with `ExternalFrequency` = 1.0 eV, where the envelope sine has a frequency `ExternalFrequency2` = 0.1 eV, and the total simulation time determined from `EnergyResolution` = 0.1 eV, as described in Eq. (B.11)

B.5 How to Prepare Pseudopotentials and Basis Sets

B.5.1 Pseudopotentials

SIESTA reads pseudopotentials that are stored in either ASCII (with extension `.psf`) or binary (with extension `.vps`) files. In general, you need to generate pseudopotentials for each species defined in the input file by an outside program. SIESTA source code comes with a pseudopotentials generation program called ATOM (read `siesta/Pseudo/atom/README` for more complete authorship and copyright acknowledgements). For pseudopotentials generation with ATOM, we refer you to the ATOM manual `siesta/Pseudo/atom/atom.tex` and associated references in the manual.

Fortunately, the SIESTA development website (<http://www.uam.es/siesta/>) has a database of pseudopotentials translated for SIESTA's ASCII `psf` pseudopotentials from ABINIT's Fritz-Haber-Institute (FHI) pseudo database (<http://www.abinit.org/Psps/>). You can download either LDA or GGA pseudopotentials for most of the elements on the periodic table.

In cases where you need to thoroughly test the performance of pseudopotentials, the following two sites are highly recommended:

- OCTOPUS is an open-source real-space grid-based TDDFT program

<http://www.tddft.org/programs/octopus/wiki/>.

This web-based pseudopotential generator generates non-local, norm-conserving Troullier-Martins pseudopotentials in the `psf` format that is used by SIESTA. This site is especially useful since it can also generate an input file for the ATOM program that comes with SIESTA. The URL for the pseudopotential generator is

<http://www.tddft.org/programs/octopus/wiki/index.php/Pseudopotentials>.

- OPIUM is an open-source pseudopotential generation program. This program can be used not only to generate pseudopotentials but also tests the generated pseudopotentials. You can find more information on the OPIUM project website at

<http://opium.sourceforge.net/>.

B.5.2 Basis Sets

There is no “magic” basis set that works for every situation. In principle, use of the standard SIESTA algorithm of generating basis sets, you can make better basis set the “brute force way” by increasing the cut-off radius of every constituent atom of first- ζ orbitals larger and larger, and the same time increase the number of multiple- ζ orbitals more and more. However, you soon find out that the SIESTA execution time becomes impractically long even for the ground-state calculation; hence, it is hopeless to compute the time-evolution with a basis set that is too large. In practice, you don't rarely need such large basis since

not all basis orbital has the coefficient large enough to play any role in the final quantities of interest. In other words, within a certain accuracy, the quantities of interest normally converge at a limited number of basis orbitals. Moreover, unlike the wave-function methods (with complete active space SCF) even at the limit of infinite basis orbitals, the DFT is *not* guaranteed to obtain the optimal value, and the error becomes smaller and smaller. Unless exact exchange-correlation is available, all DFT methods are approximate and you cannot even estimate the absolute error.

With some of the subtleties previously discussed in mind, we now discuss a few “sensible” ways to construct better a basis set in SIESTA for the nonlinear optical calculation. First, you need to increase the cut-off radius or, better, decrease the energy shift δE parameter `PA0.EnergyShift`. This is based on the fact that the optical nonlinearity mainly comes from the tail of the atomic orbitals. As the first hyperpolarizability must be zero for a spherically symmetrical system, the orbitals near the core region would not contribute very much to the first nonlinear properties. The default value of `PA0.EnergyShift` is 0.02 Ryd, but we suggest changing this value from 10^{-4} to 10^{-6} Ryd. Try various `PA0.EnergyShift` values and see how the (hyper)polarizabilities change as you decrease this parameter. You also need to watch out for a change in the execution time. The other parameter for changing the quality of basis is `PA0.SplitNorm`, where it controls the split radius of the second- ζ orbital. I found, in general, that decreasing the split norm value (increasing the split radius) will improve the value of first hyperpolarizability, but unless you also increase the number of multiple- ζ , the value of dipole and linear polarizabilities become degrades.

If you cannot get a satisfactory result with the standard DZP basis, you need to explore increasing the number of multiple- ζ basis. In order to get started constructing multiple- ζ , you must first run SIESTA with the standard DZP basis setting. For example, if you run H2O with the default setting, the standard output will print out the automatic generation of the DZP basis as follows:

```
%block PA0.Basis          # Define Basis set
0          2              # Species label, number of l-shells
n=2   0   2              # n, l, Nzeta
```

```

3.305      2.479
1.000      1.000
n=2   1   2 P   1           # n, l, Nzeta, Polarization, NzetaPol
3.937      2.542
1.000      1.000
H           1           # Species label, number of l-shells
n=1   0   2 P   1           # n, l, Nzeta, Polarization, NzetaPol
4.709      3.760
1.000      1.000
%endblock PA0.Basis

```

The first columns of floating point numbers show the cut-off radius of the first- ζ , whereas the second columns gives the split radius of the second- ζ . Oxygen has two valence shells with $2s$ state ($n = 2, l = 0$) and $2p$ state ($n = 2, l = 1$). Hydrogen has one valence shell with $1s$ state ($n = 1, l = 0$), respectively. The highest occupied angular momentum state also includes the polarization orbital specified by the label P followed by the number of the orbital (the DZP basis has one polarization for each atom). Supposing that you want to make the TZP (triple- ζ + 1 polarization) basis for all available valance electron orbitals, you can simply add the third column and change the number of zeta from 2 to 3 as follows, and include this basis definition in the input file to run.

```

%block PA0.Basis           # Define Basis set
0           2           # Species label, number of l-shells
n=2   0   3           # n, l, Nzeta
0.000      0.000      0.000
1.000      1.000      1.000
n=2   1   3 P   1           # n, l, Nzeta, Polarization, NzetaPol
0.000      0.000      0.000
1.000      1.000      1.000
H           1           # Species label, number of l-shells
n=1   0   3 P   1           # n, l, Nzeta, Polarization, NzetaPol

```

```

0.000      0.000      0.000
1.000      1.000      1.000
%endblock PA0.Basis

```

where 0.000 is the cut-off radius to let SIESTA to choose the cut-off radius from the `PA0.EnergyShift` value instead of the user-specified radius. Similarly, you can create the TZDP (triple- ζ + double polarizations) basis by increasing the number of polarization orbitals, i.e., set `P 2` instead of `P 1`. The other strategy for constructing TZP is to run DZP calculation twice, using two different `PA0.SplitNorm` values. Then, you can discover the best split radius to choose for the second- and third- ζ .

In order to check the significance of each orbital, we suggest looking into the coefficients of each orbital. If the coefficient of a particular orbital are too small for all n and l states, the orbital is likely not playing a role in the calculation. Here are a few steps you need to follow in order to print out the wave function. First, you need to run SIESTA and perform the ground-state calculation. Find the following lines from the standard output:

```

initatomlists: Number of atoms, orbitals, and projectors:  3    23    34

siesta: Automatic unit cell vectors (Ang):
siesta:    7.147558    0.000000    0.000000
siesta:    0.000000    5.482158    0.000000
siesta:    0.000000    0.000000    5.677525

```

Next, you need to run SIESTA again by adding the following statements into your input file (don't ask why).

```

WriteWaveFunctions .true.
LatticeConstant 1.0 Ang
%block LatticeVectors
    7.147558    0.000000    0.000000
    0.000000    5.482158    0.000000
    0.000000    0.000000    5.677525

```

```
%endblock LatticeVectors
%block WaveFuncKPoints
    0.000 0.000 0.000 from 1 to 23
%endblock WaveFuncKPoints
DM.UseSave DM .true.
```

After the end of the second run, you can check the coefficients of all the wave functions shown after the following line:

```
writewave: Wave Functions Coefficients
```

Note that only occupied states are important for the optical calculations, i.e., you only need to look at orbitals that are occupied. Specifically, only the bound states having negative orbital energies are especially significant.

B.6 User's Guide for prepsiesta

The script `prepsiesta` is a Perl script to help preparing SIESTA jobs for linear and nonlinear calculations. If you run `prepsiesta` without an argument, it returns the basic usage:

```
$ prepsiesta
```

```
You must specify SIESTA fdf file.
```

```
Usage: prepsiesta [OPTION] ... [FILE]
```

```
-i, -inter      : Interactive Mode
-d, -default    : Predefined default
-e, -efields    : Electric Fields file
-s, -structure  : XYZ structure file
-c, -car        : CAR structure file
-p, -psf        : Pseudo Potential directory
-b, -basis      : PAO basis file
-m, -param      : FDF parameter file
-v, -version    : Version number
```

Examples:

Basic usage with external electric fields.

```
prepsiesta -e "0.0 0.001" input.fdf
```

We have already seen one of the simplest examples of this script with the option “-e.”

```
$ prepsiesta -e "0.0 0.001" input.fdf
```

Utilizing some of the options, you can simplify the work of preparing input files for many similar jobs, for example:

1. Basic usage with external electric field strengths to read from a file:

```
$ prepsiesta -e efields.dat input.fdf
```

2. Include the external structure in xyz format:

```
$ prepsiesta -e efields.dat -xyz structure.xyz input.fdf
```

3. Include the external structure in car format:

```
$ prepsiesta -e efields.dat -car structure.car input.fdf
```

4. Include the external basis definition file:

```
$ prepsiesta -e efields.dat -xyz structure.xyz -b basisfile.fdf
input.fdf
```

5. Include reference to the pseudo potential directory:

```
$ prepsiesta -e efields.dat -xyz structure.xyz -b basisfile.fdf -psf
psfdir input.fdf
```

6. Include reference to the common fdf parameters:

```
$ prepsiesta -e efields.dat -xyz structure.xyz -b basisfile.fdf -psf
psfdir -m common.fdf input.fdf
```

Advanced settings:

When you set the environment variable `$SIESTA_INPUT`, this script looks for `efields.dat` in that directory, the structure files in `$SIESTA_INPUT/structures`, the pseudo files in `$SIESTA_INPUT/pseudo/$xc` directory (`$xc` is the variable set in this script), and read the fdf parameter file located at `$SIESTA_INPUT/fdfbasis/$xc.fdf`. Then, if you store your

basis definition in the `$SIESTA_INPUT/fdfbasis` directory, you can run this script as:

```
$ prepsiesta -xyz structure.xyz input.fdf
```

This script call is the same as the following:

```
$ prepsiesta -e $SIESTA_INPUT/efields.dat  
-xyz $SIESTA_INPUT/structures/structure.xyz  
-b $SIESTA_INPUT/fdfbasis/basis_structure.fdf  
-psf $SIESTA_INPUT/pseudo/$xc  
-m $SIESTA_INPUT/fdfbasis/$xc.fdf input.fdf
```

B.7 List of Available TDDFT Options in SIESTA

TD.NumberOfTimeSteps (*integer*): Total number of the real-time simulation steps.

Use: Used only if **TD.EnergyResolution** is not specified.

Default value: 0

TD.TimeStep (*real*): The size of time step Δt of the real-time simulation in unit of 1/Ryd.

Default value: 0.07

TD.NumberOfE0TimeSteps (*integer*): You may need to run several time steps for the zero field in order to make the final result more stable. Setting this value at less than the default value is not recommended.

Default value: 2

TD.ShapeOfEfield (*string*): Specify the shape of the external electric field, the step function (constant for $t < 0$ and zero for $t \geq 0$) (**step**), the delta function (**delta**), and a single sine wave (**sine**), and double sine wave (**sine2**).

Default value: **step**

TD.ExternalFrequency (*real energy*): Frequency of the external monochromatic sine wave.

Use: Used only if **TD.ShapeOfEfield** = **sine** is specified.

Default value: 1.0 eV

TD.ExternalFrequency2 (*real energy*): Frequency of the second external monochromatic sine wave.

Use: Used only if **TD.ShapeOfEfield** = **sine2** is specified.

Default value: 1.0 eV

TD.ExternalPhase (*real*): Phase of the external monochromatic sine wave in radian.

Use: Used only if **TD.ShapeOfEfield** = **sine** is specified.

Default value: 0.0

TD.ExternalPhase2 (*real*): Phase of the second external monochromatic sine wave in radian.

Use: Used only if **TD.ShapeOfEfield** = **sine2** is specified.

Default value: 0.0

TD.ExternalPacket (*logical*): Use an envelope function to enclose the monochromatic wave. When this parameter is used with **TD.ShapeOfEfield** = **sine**, the Gaussian envelope is used. If this parameter is specified with **TD.ShapeOfEfield** = **sine2**, the sine envelope is used.

Use: Used only if **TD.ShapeOfEfield** = **sine** or **sine2** is specified.

Default value: **.false.**

TD.ExternalPacketSigma (*real energy*): Specify the width of the Gaussian envelope function.

Use: Used only if both **TD.ShapeOfEfield** = **sine** and **TD.ExternalPacket** = **.true.** are specified.

Default value: $2.35482/\pi \Delta E$ (see Eq. B.9)

TD.ExternalPacketCenter (*real energy*): Specify the central peak location of the Gaussian envelope function.

Use: Used only if **TD.ShapeOfEfield** = **sine** and **TD.ExternalPacket** = **.true.** is specified.

Default value: $\pi/2\Delta E$ (see Eq. B.9)

TD.ExternalPacketPCenter (*real*): The location of the central peak of the Gaussian envelope in percentage, where 0.5 is the center.

Use: Used only if **TD.ExternalPacketCenter** is not specified.

Default value: 0.5

TD.ExternalWidthFactor (*real*): Specify the Lorentzian width $\Gamma = w * \Delta E$ of w in Eq. B.9.

Use: Used only if both **TD.ShapeOfEfield** = `sine` and **TD.ExternalPacket** = `.true.` are specified.

Default value: π

TD.Method (*string*): Specify the time-evolution method. Currently, only the Crank-Nicholson algorithm is implemented. You can set this value to be `cn`, `cn2`, or `cn3`, where respectively increases the number of the operator sum/product in the numerator and the denominator.

Default value: `cn2`

TD.WriteWaveFunctions (*logical*): Primitive routine to dump the time-dependent wave functions for occupied states in each time step (output file will be huge).

Default value: `.false.`

B.8 Parallel Computing

Building MPI parallel binary and running on a cluster can be very tricky. One of the best sources of MPI compilation from scratch is in the SIESTA mailing list. It is highly recommended to follow the instructions given below:

<http://www.mail-archive.com/siesta-l@listserv.uam.es/msg00977/mini-howto.pdf>

Assuming your cluster is already set up for an MPI environment (such as `mpich`, `lam-mpi`, or `openmpi`) you will need to compile LAPACK, BLACS, and ScaLAPACK libraries before attempting to compile SIESTA in parallel. Even if an alternative MPI library is already installed on your cluster, you may have trouble linking to the SIESTA source code. Personally, I encounter fewer problems when I compile LAPACK, BLACS, and ScaLAPACK libraries from scratch.

B.8.1 Important Note

If you are running the real-time SIESTA in parallel, you need to specify that the number of working processors be equal to an integer squared (4, 9, 16, ... and so on) in order to make the matrix-inversion operation run in parallel. If you try to run on any other number of processors, only the head node performs the inversion, causing significant performance deration, and/or you experience memory issues on the head node.

B.9 Developer's Note

We try to make the modification to the original SIESTA source code as small as possible and package all extra functions and subroutines for the time evolution in the FORTRAN90 module `m_evolve.F90`. This is mainly for reducing the future maintenance cost when a new version of the SIESTA source code becomes available. The required modification for the future release should be minimal, as long as no significant change in the SCF loop is made.

The following SIESTA files are modified (modified lines are indicated by “!TD” at the end of lines)

`siesta-2.0.1/Src/Makefile`

```

siesta-2.0.1/Src/atmparams.f
siesta-2.0.1/Src/atom.f
siesta-2.0.1/Src/dhscf.F
siesta-2.0.1/Src/diagg.F
siesta-2.0.1/Src/efield.F
siesta-2.0.1/Src/siesta.F

```

The modification to `Makefile` is necessary to include `m_evolve.F90` module before attempting to compile. Only minor parameter changes are made in `atmparams.f`, and `atom.f`. The change made on `atmparams.f` is to increase the maximum number of zetas from 3 to 6, as this is necessary for increasing the accuracy of a small system. The change made on `atom.f` is to allow users to enter the smaller value of energy shift in order to make the cut-off radius larger, again for accuracy.

The main SIESTA routine is in `siesta.F`, where we utilize the SCF loop to construct Hamiltonian operator, orbitals, and density at each time step. There is one extra outer loop to run the time-evolution cycle that encloses the SCF loop; this is so that the time-evolution start after the end of the SCF loop. We initialize variables before the time-evolution loop and deallocate variable after the loop in `siesta.F`. For the time-dependent electric field, we need to reset the value of the field whenever it changes. The change must be made in `dhscf.F` where it calls `efield.F`. The routine `efield.F` actually sets the value of the electric field, but the routine is only called once in `dhscf.F` by default; thus, both must be modified for the time-dependent case. The routine `diagg.F` is called in the matrix diagonalization routine `diagon.F`. This `diagg.F` routine constructs a new density matrix either by diagonalizing the matrix during the SCF loop or by calling the time-evolution routine to make the new density. This routine also computes the electron occupation number that will be necessary for the time-evolution routine. There is a small difference to create the density matrix in the SCF and time-evolution loop, since the wave function is real in the SCF loop (gamma point calculation), but complex in the time-evolution loop.

Besides small changes in the original SIESTA source code, all time-evolution routine is packaged in `m_evolve.F90`. The main subroutine is `subroutine evolve(...)`. The main

inputs are Hamiltonian operator H , the overlap matrix S , and previous time-step density ρ_{old} . Then, the output is the new density ρ_{new} . For the TDDFT calculation, only electrons of the occupied states need to be evaluated. The full density matrix requires the storage space of $N_{\text{orbs}} \times N_{\text{orbs}}$ matrix with N_{orbs} being the total number of local orbitals. We, however, set the dimension of ρ_{old} and ρ_{new} to $N_{\text{orbs}} \times N_{\text{occ}}$, where N_{occ} is the number of occupied states. For example, in case of the 5Z4P basis set of H_2O , we have $N_{\text{orbs}} = 71$ and $N_{\text{occ}} = 4$. Thus, the required storage space for ρ is 71×4 complex numbers. We explicitly utilize this property in order to reduce the number of operations required to evaluate the new density. The linear equation for the Crank-Nicholson operator to find the new density is

$$\rho_{\text{new}} = Q^{-1}P \rho_{\text{old}}, \quad (\text{B.13})$$

where P and Q are the numerator and the denominator of the Crank-Nicholson operator, respectively. This is the same as

$$Q \rho_{\text{new}} = P \rho_{\text{old}}. \quad (\text{B.14})$$

The usual routine for solving the linear equation above in LAPACK is to use the LU decomposition routine for the matrix Q and back substitute to get the new density ρ_{new} . The required number of operations for the back-substitution can be greatly reduced, since we only need to fill the occupied electron density.

Solving the required linear equation for the Crank-Nicholson operator is straightforward for a single processor and easily done with a standard LAPACK routine. There is a bit of complication for the parallel computation. Corresponding libraries for solving the linear equation in parallel are available in BLACS and SCLAPACK. The matrix for performing an LU factorization requires to be squared, the matrix must be the shape of $np \times np$ processor grid where np is the number rows and columns of the 2D processor grid with the total number of processors equal to $N_{\text{procs}} = np \times np$. The matrix P and Q , associated with Hamiltonian operator H and the overlap matrix S , must reshape and distribute elements to all nodes before calling the SCLAPACK routine. Since SIESTA constructs the matrix H and S into 1D processor grid in which the number of rows and columns are divided by

N_{procs} . We, therefore, need to re-index the input matrices H and S inside the time-evolution routine. The overlap matrix S does not change over time, but H is updated every time step, so re-indexing must be performed efficiently in order to reduce the communication cost over processor nodes. To do this, we create a “cache” matrix for index-mapping during the initial time step and store the mapping information for subsequent time-steps for fast re-indexing. The operation after this mapping procedure is straightforward; you only need to call corresponding MPI routines instead of a single-processor LAPACK routines.

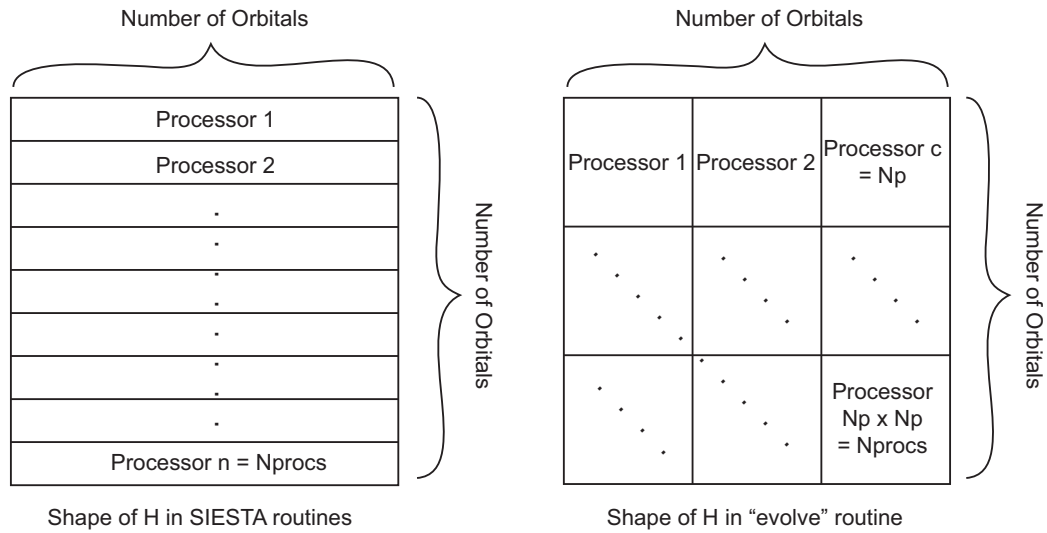


Figure B.3: Schematic of the Hamiltonian matrix block form of the 1D processor grid in SIESTA main routine and the 2D processor grid in the matrix inverses routine.

B.10 Limitations of the Real-time TDDFT in SIESTA

The real-time TDDFT SIESTA has several limitations. The followings lists some of the known limitations:

- **SolutionMethod = `diagon`** is required. This is important for the large system since SIESTA automatically switches **`diagon`** to **`orderN`** if the number of atoms involved is greater than 100. This digitalization routine is only used in the SCF loop to prepare

wave functions. The time-evolution does not use this digitalization routine, but the Crank-Nicholson has similar \mathcal{O} scaling.

- The real-time TDDFT will not work for solids or crystals. You can only calculate properties for molecules. As a result, only the gamma point $\mathbf{k} = 0$ calculation is implemented.
- Parallel operations work only in orbital-based, a 1-D block cyclic distribution. The operation of 2-D blocked distribution will not work.
- Restarting or checkpoint features will not work. If a computer or one of the compute nodes crashes during calculation, you need to start over again from the beginning. Implementation should not be *too* difficult, but the restarting feature is not yet implemented.

VITA

Yoshinari Takimoto was born in Shizuoka, Japan. He grew up in Kanagawa, a suburb of Tokyo. Yoshinari earned his B.S. in Engineering Physics at Colorado School of Mines in 1997. He began his graduate studies at the University of Washington in 2000, where he earned the M.S. in Physics in 2003. This dissertation completes the requirements for his Ph.D. in Physics.